DESIGN OF A LUNAR SURFACE STRUCTURE

By

SOHROB MOTTAGHI

A thesis submitted to the

Graduate School-New Brunswick

Rutgers, The State University of New Jersey

in partial fulfillment of the requirements

for the degree of

Master of Science

Graduate Program in Mechanical and Aerospace Engineering

written under the direction of

Professor Haym Benaroya

And approved by

_____

_____

_____

New Brunswick, New Jersey

October, 2013

ABSTRACT OF THE THESIS

DESIGN OF A LUNAR SURFACE STRUCTURE

by Sohrob Mottaghi

Thesis Director: Prof. Haym Benaroya

The next step for manned exploration and settlement is a return to the Moon. In such a return, the most challenging task is the construction of structures for habitation, considering the Moon's hostile environment. Therefore the question is: What is the best way to erect habitable structures on the lunar surface?

Given the cost associated with bringing material to the Moon, In-Situ Resource Utilization (ISRU) is viewed by most as the basis for a successful manned exploration and settlement of the Solar system. Along these lines, we propose an advanced concept where the use of freeform fabrication technologies by autonomous mini-robots can form the basis for habitable lunar structures. Also, locally-available magnesium is proposed as the structural material. While it is one of the most pervasive metals in the regolith, magnesium has been only suggested only briefly as a viable option in the past. Therefore, a study has been conducted on magnesium and its alloys, taking into account the availability of the alloying elements on the Moon.

An igloo-shaped magnesium structure, covered by sandbags of regolith shielding and supported on a sintered regolith foundation, is considered as a potential design of a lunar base, as well as the test bed for the proposed vision. Three studies are carried out:

First a static analysis is conducted which proves the feasibility of the proposed material and method.

Second, a thermal analysis is carried out to study the effect of the regolith shielding as well as the sensitivity of such designs to measurement uncertainties of regolith and sintered thermal properties. The lunar thermal environment is modeled for a potential site at 88^{o} latitude in the lunar South Pole Region. Our analysis shows that the uncertainties are in an acceptable range where a three-meter thick shield is considered. Also, the required capacity of a thermal rejection system is estimated, choosing the thermal loads to be those of the Space Station modules.

In the third study, a seismic model based on best available data has been developed and applied to our typical structure to assess the vulnerability of designs that ignore seismicity. Using random vibration and modal superposition methods, the structural response to a lunar seismic event of 7 Richter magnitude indicates that the seismic risk is very low. However, it must be considered for certain types of structural designs.

Acknowledgements

First and foremost, I wish to express my gratitude to my research advisor Professor Haym Benaroya, who graciously allowed me to build this thesis on his ideas and has guided me throughout this project. I am thankful for his friendship, support, and kindness.

I would like to thank my committee members Professor Haim Baruh and Professor William J. Bottega. A big acknowledgment goes to Professor Haim Baruh and the New Jersey NASA Space Grant Consortium for his interest and support in parts of this research work. Also, I am thankful to Professor Bottega for all his help during the time that he was Graduate Director.

I want to thank two of my colleagues, Stephen Indyk and Zachary Porter, who helped in parts of this research work. Also, I wish to thank my other officemates (Dr. Yuri Gulak, Dr. Elan Borenstein, Tushar Saraf, Paul Bonness, and Joey Sanchez) who made our office a pleasant place to work.

Our Department of Mechanical and Aerospace Engineering has been an enjoyable place to work, and therefore I am thankful to all our faculty members, staff, and my fellow graduate students.

I have been blessed with many great friends to all of whom I am thankful, specially; Chiara Briguglio, Alireza Yazdani, Giorgiana Giancola, Ron Berkowitz, Mona Golbabaei-Asl, Murthy Kalluri, Sankha Banerjee, Daniel Cordasco, and Peter Balogh.

Words cannot express my gratitude to my family. I am truly grateful to my parents, Jalal Mottaghi and Meetra Emamy, and to my sister, Sarah Mottaghi, for all their support and love.

Last but not least, I wish to thank all the researchers and authors whose work I have used in this thesis.

Dedication

In memory of my father, Dr. Jalal Mottaghi.

Table of Contents

List of Tables

List of Figures

Chapter 1. Introduction

Lunar colonization is humanity's long lasting aspiration. It can be traced back to as early as the second century when Lucian writes of a trip to the Moon. In 1638, Wilkins, an English clergyman and natural philosopher, mentions lunar colonization soon after Kepler's earlier telescopic observations of the lunar surface. After Wilkins, there exist many science fiction stories that write of human activities on the Moon. An example is Jules Verne's fictional novel "From the Earth to the Moon". By the 20th century, the literature takes a more scientific approach toward lunar exploration, and by mid-20th century, papers on different approaches to building lunar shelters come to exist (Johnson and Leonard 1985). In 1969, Neil Armstrong became the first human to set foot on the Moon in the Apollo 11 mission. During the Apollo missions, many experiments were carried out and data were transmitted back to Earth. As the understanding of the lunar environment increased, the literature on lunar bases became very detailed and many authors proposed different lunar structures and wrote of specifications that must be considered in the design of these structures. Unfortunately, by the mid-1990s the political climate turned against lunar exploration and Mars began to be viewed as the "appropriate" destination, essentially skipping the Moon (Benaroya et al. 2002). With the 2004 declaration of the Bush vision for the manned return to the Moon by 2020, lunar literature gained some of the attention back from Mars, but this did not last long due to the 2010 Obama call for the end to NASA's Moon program. Although during the past few decades, many hundreds of papers have been written on the subject, we review a few

of these that we believe to be representative of evolution of lunar base concepts up to the present day.

Generally, the proposed lunar structures can be divided to three categories: (i) Inflatable, (ii) Rigid, and (iii) Hybrid (inflatable/rigid). The hybrid structures, as categorized here, are those consisting of inflatable sections (containing air), and rigid sections (bearing the loads). Other definitions exist in the literature for hybrid structures. In comparison with the other two types, very few efforts have been made to model hybrid structures and these are not considered here. A good example, however, is the work done by Land (1985).

1.1 Inflatables

Inflatable habitats are designed to minimize the transport of materials from the Earth to the Moon. A study was done during the Apollo program on a number of inflatable manned space systems by Goodyear Aerospace Corporation through NASA's Langley Research Center (Roberts 1988). Ever since, many researchers have devoted their efforts to design and optimize these structures. Land (1985) proposed a pneumatic structure that permanently supports the regolith shielding layer. In his design, the deflated structure is initially laid on a leveled surface, then regolith is pushed over and the structure is inflated. The upper surface of the structure is ribbed to anchor into the regolith (Fig. 1.1).

In another research work, Roberts (1988) proposed an inflatable habitat that consists of a spherical pneumatic envelope with an interior structural cage to support the floors, walls, and to hold up the envelope if the pressure is lost (Fig. 1.2).

Nowak et al. (1992) considered a pillow-shaped, modular inflatable lunar base. The structure is composed of several basic modules and each module consists of the following structural components: roof and floor membranes, four columns and footings, four arched ribs, and external wall membranes (Fig. 1.3).

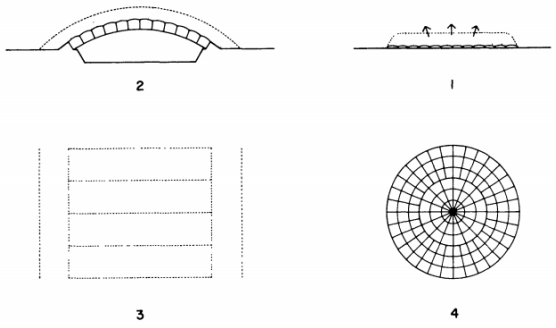

Figure 1.1. Base concept, low arch shield with pneumatic support structure (Land 1985, courtesy of NASA). (1) Deflated structure flat structure flat on ground. (2) Structure inflated, raising the regolith. (3) Plan showing the concept applied in sections for a continuous low arch shield. (4) Plan showing concept applied in a low, domed shield.

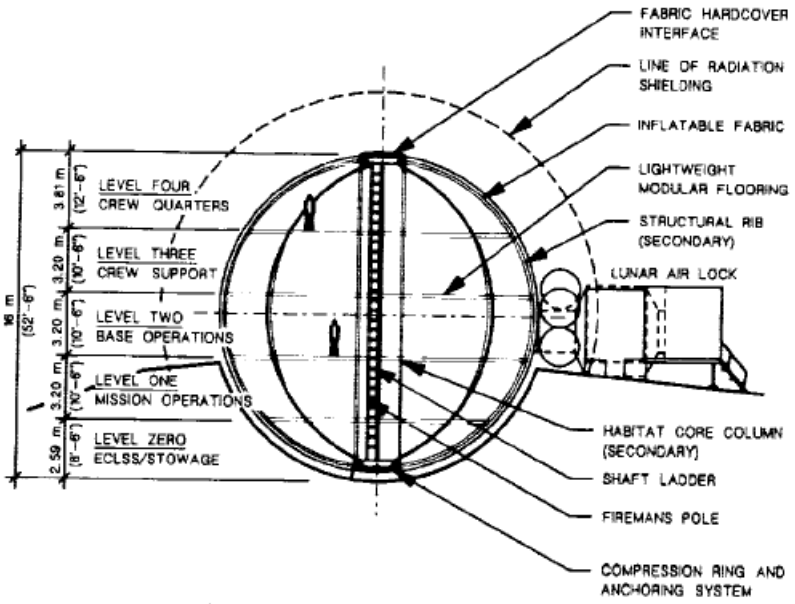

Figure 1.2. Cross section of the inflatable Lunar Habitat (Roberts 1988, courtesy of NASA).

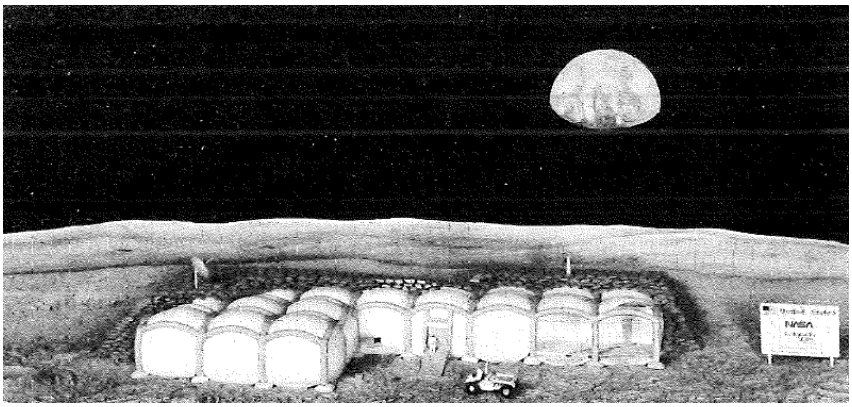

Figure 1.3. Physical model of inflatable lunar base (Nowak et al. 1992, with permission from ASCE).

In 1996, NASA Johnson Space Center (JSC) started to conduct a study on a return mission to the lunar surface. They considered the habitat craft as an inflatable, deployable, cylindrical, composite structure with rigid endcaps that would sit atop a landing craft. The structure would expand to full volume when on the lunar surface (Fig. 1.4) (Cadogan et al. 1999).

In another study, Gruber et al. (2007) investigated bionic concepts that can be applied to deployable structures. They explained that such natural concepts are not translated into terrestrial application because of the scaling problem. They believed that the deadweight, that limit these concepts on Earth, can be overcome for lunar applications due to the Moon's weaker gravity field. Their lunar habitat design was inspired by wing folding principles and geometry of ladybirds (Fig. 1.5), while five other designs were also considered for different lunar applications.

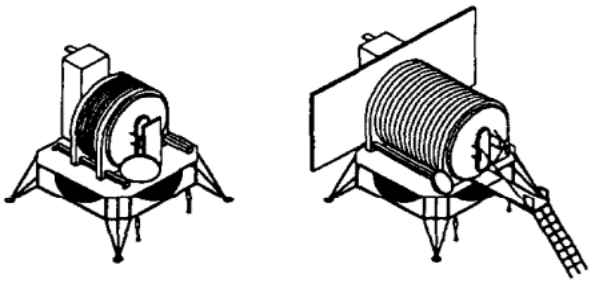

Figure 1.4. Stowed and deployed lunar habitat (Cadogan et al. 1999, with permission from Elsevier).

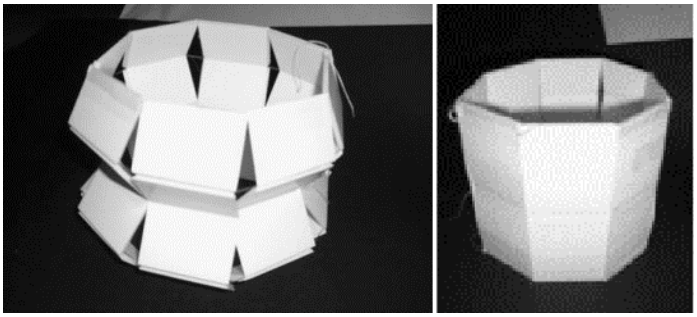

Figure 1.5. Working model showing deployment process (Gruber et al. 2007, with permission from Elsevier).

All of the lunar structures mentioned above use the regolith as a shielding layer except the JSC structure which utilizes a double layer composite fabric to protect the interior from the lunar environment.

1.2 Rigid Structures

Many research works have been devoted to rigid structures and numerous structural designs have been proposed. Kaplicky and Nixon (1985) investigated the use of direct derivatives of module types being developed for the Space Station. The structure is a

series of modules grouped into a complex under a regolith shielding envelope. The envelope is configured as a shallow, flat-topped mound of loose regolith supported by a continuous tension membrane that is connected to a regular grid of telescopic columns and supported by tapered beams (Fig. 1.6). In another study, King et al. (1990) proposed the concept of using the liquid oxygen tank portion of the space shuttle external tank that would be modified in low Earth orbit before transport to the Moon.

In another study, Lin et al. (1989) proposed a precast, prestressed concrete lunar structure of 120 ft diameter and 72 ft height (Fig. 1.7). Their structure required 8000 tons of concrete, 110 tons of prestressing steel and 250 ton of rebars. Their preliminary analysis indicated the feasibility of concrete structures, yet an estimated 36 tons of hydrogen would have had to be transported to the Moon to make the concrete. Meyer and Toutanji (2007) also investigated the possibility of lunar concrete structures with the difference that their lunar concrete would not require water. They proposed an arched-panel habitat made out of a sulfur-lunar regolith concrete (Fig. 1.8).

In another study, Aulesa (2000) proposed a dome shape shell structure made of cast basalt (regolith) that is to be covered by 5.4 meters of unconsolidated regolith in order to combat against radiation. The location of the conceptual base is selected at a mountain in the lunar South Polar Region at 0º longitude, 86º South latitude. This location is selected due to the fact that Sun never completely sets and the Earth is visible 100% of the time.

An excellent study is the work done by Ruess et al. (2006). They outlined a structural engineer's approach, having considered the lunar extreme environment and availability of the materials on the Moon. Having proposed their lunar base as a group of igloo-shaped

structures made of cast regolith (Figure 1.9), they present a very detailed design. They recommended a design volume (living and working areas) of 120 m^3 per person for a lunar habitat based on research of long-term habitation and confined spaces.

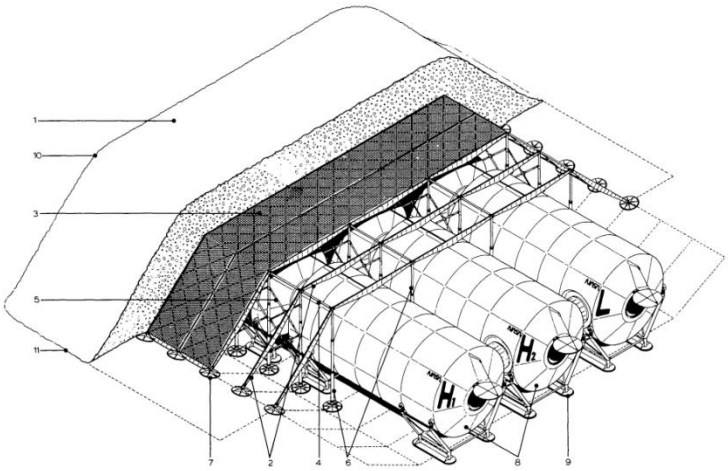

Figure 1.6. Cutaway illustration of superstructure envelope system (Kaplicky and Nixon 1985, courtesy of NASA): 1- regolith mass shielding; 2-main tapered beam; 3-grafite fiber mesh; 4-longtudinal struts; 5-longitudinal bracing; 6- telescopic tubular columns; 7- circular footpads; 8- linked habitat/laboratory/workshop modules; 9- module ground support cradles; 10- crest of slope; 11- base of slope.

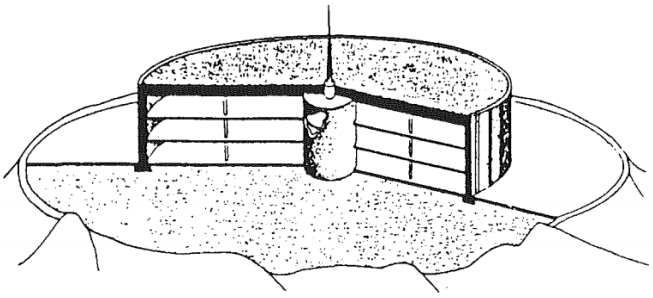

Figure 1.7. Three-level concrete lunar base proposed by Lin et al. (1989, with permission from ASCE).

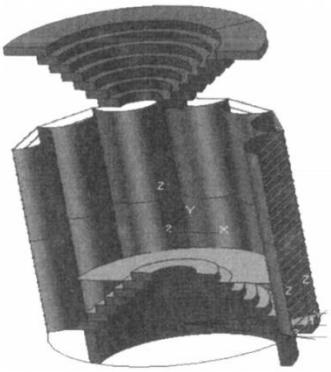

Figure 1.8. Arched-panel habitat proposed by Meyers and Toutanji (2007, with permission from ASCE).

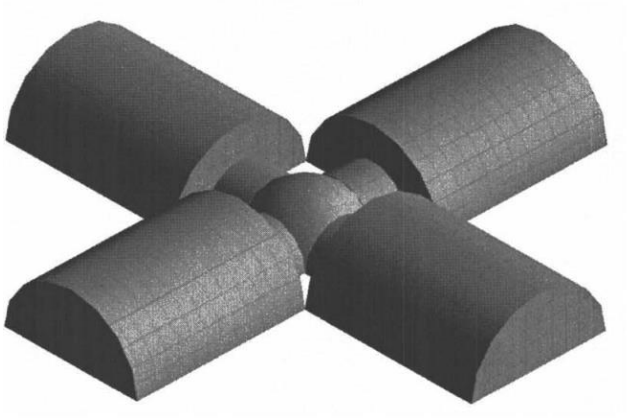

Figure 1.9. Proposed lunar structure by Ruess et al. (2006), with permission from ASCE.

1.3 Summary and Thesis Outline

As mentioned earlier, hundreds of papers exist on the subject of lunar structures, many offering unique approaches. Taking into account the many factors that are needed to be considered in designing a lunar structure, it is very hard to favor one design over the others. However, the majority of the research is devoted to innovative designs that, in

principle, are able to overcome the challenges that the hostile lunar environment imposes. These detailed designs are mostly evaluated by considering the static analysis of the structures, while the other factors are just mentioned. For instance, although most of the concepts studied have considered regolith shielding layers to combat against radiation, extreme temperature fluctuations, and micrometeoroid bombardments, proposing thicknesses varying from 30 cm to 15 m, very few have carried out a basic analysis to justify these values. Even in these few studies, the uncertainties associated with regolith's physical properties are often neglected. As we will see throughout this work, the differences between the estimated values of some physical properties in the literature are as large as an order of magnitude.

There is no doubt that the existing literature is very valuable, however, there is a serious lack of computational studies. Returning to the Moon requires studies on redefining the NASA roadmaps, developing detailed information about the lunar environment, technological assessments, as well as computational studies that can assist in evaluating the feasibility of each design.

Moreover, a review on the evolution of lunar structural concepts reveals that those designs, not surprisingly, have tried to adapt new technologies as they came to exist. Therefore, in Chapter Two, we review the relevant NASA roadmaps and we propose an advanced concept for autonomous construction of lunar surface structures. This advanced concept is based on current technologies as well as the ones we anticipate to mature in near future. In Chapter Three, we explore the materials on the Moon, propose magnesium as a feasible structural material, and review the properties of magnesium alloys, taking into account the availability of the alloying elements on the Moon.

In Chapter Four, we choose the recommended design dimensions by Ruess et al. (2006) and magnesium as the structural material, and carry out a static analysis to design our typical structure: (a) to prove the feasibility of using magnesium as structural material and (b) to obtain a test bed for the analysis in the remainder of this thesis.

An extensive review of lunar temperature and regolith thermal properties is presented in Chapter Five, after which we conduct thermal analyses for a selected location on the lunar South Pole. Having examined the uncertainties in thermal properties of the sintered regolith, the needed thermal rejection system's capacity is estimated for our typical lunar structure.

Chapter Six presents a review of the lunar seismic literature. We develop a seismic model based on the best available data and apply it to our typical lunar structure to assess the vulnerability of designs that ignore seismicity.

Finally, in Chapter Seven we conclude this research work and outline future work than can help to develop this work further and, wishfully, one day contribute to making the lunar base concept a reality.

Chapter 2. Advanced Systems Concept for Autonomous Construction and Self-Repair of Lunar Surface ISRU Structures

Human exploration calls for a return to the Moon. Such a return requires construction of structures that can be used for habitation as well as other applications. Each offers unique challenges to the design engineers and the astronaut construction teams that must erect the structures. Therefore the question is: What is the best way to erect habitable structures on the lunar surface?

In this chapter, we begin by answering the above question. Exploring the current technologies that can meet the requirements needed to construct structures with minimal if any dependence to material transportation from the Earth, we propose an advanced concept. Then, we choose a conceptual design for a lunar structure as a test bed of our vision that will be the core for the rest of this thesis. This chapter is a short summary of the relevant discussions from our earlier work (Benaroya et al. 2012).

2.1 ISRU for Manned Space Exploration and Settlement

In-Situ Resource Utilization (ISRU) is viewed by most as the basis for a successful manned exploration and settlement of the solar system. It is as its name implies, the "living off the land" that is a necessity for any untethered manned activity. The goal of ISRU is to allow settlements on the Moon and Mars and beyond to live with minimal if any dependence on the shipment of raw materials from Earth. The existence of a broad spectrum of elements on the lunar surface and on Mars gives hope that, in principle, it is

possible to build a sustainable infrastructure on both these bodies that is based on local resources.

Many technical reports and workshops have recommended the need of technologies to process the raw regolith to useful materials for future explorations. In a NASA report, Williams and Hubbard (1981) examined a methodology for the selection of potential lunar resource sites. They point to the major need for autonomous systems, capable of data collection and analysis upon which intelligent decisions can be made about the usefulness of a potential resource site. In the proceedings edited by Mendell (1985), there are many chapters on all aspects of the development of lunar bases and the anticipated space activities in the 21st century, including needed technologies for ISRU. A workshop report edited by Fairchild and Mendell (1988) investigated potential joint development of the key technologies and mechanisms required to enable the permanent habitation of space. The autonomous construction and ISRU were among the working groups' recommendations.

The workshop report edited by Duke (1998) had as its principal purpose the examination of high-priority, near-term applications of in situ planetary resources that could lower the construction costs of human outposts on the Moon and Mars. Of particular interest was the use of indigenous material for the initial stages of planetary outpost installation.

With the 2004 declaration of the Bush vision for the manned return to the Moon by 2020, NASA embarked on an assessment of capabilities known as the capability roadmaps in key technical areas. One of these was the ISRU capability roadmap chaired by Sanders and Duke (2005). This report is an excellent and detailed overview of the ISRU

capability. It states that the early incorporation of ISRU into missions and architectures would lead to reduction in mass, cost, risk, increase mission flexibility and mission enhancement and general capabilities. Also identified in this report were critical interdependencies of ISRU with other roadmap capabilities. In the paper by Duke et al. (2006), an excellent and substantial discussion was provided on all aspects of the manned return to the Moon. An extensive and detailed section was written on the development and use of lunar resources.

Due to the importance of ISRU, many research efforts have been devoted to the processing of regolith simulant. For example,

- prospecting strategies for lunar resources with some ideas as to where certain elements are located (Taylor and Martel 2003);
- carbothermal reduction of oxides for elemental extraction and zone refining for obtaining high-purity metals (Sen et al. 2005, Balasubramaniam et al. 2010);
- extraction systems and transportation (Siegfried and Santa 2000) as well as the discovery of water ice in significant quantities (Sridharan et al. 2010);
- oxygen, metals, silicon and glass refining on the Moon (Landis 2007), extraction of magnesium and copper using a surfactant and water in supercritical carbon dioxide (Wang et al. 2008);
- using a regolith-based substrate in the fabrication of solar cells directly on the lunar surface (Horton et al. 2005);
- production of structural elements via a geothermite reaction in a mixture of lunar regolith simulant and aluminum powder (Faierson et al. 2010);

- growing plants – lunar and Martian agriculture (Kozyrovska et al. 2006, Davies et al. 2003);
- ISRU technologies development for Mars (Moore 2010), for life support systems (Sridhar et al. 2000), propellant production (Hu et al. 2007, Holladay et al. 2007).

Although these efforts had relative successes, ISRU technologies have not reached a satisfactory stage where a mission can be accomplished without any terrestrial support. However, the advancements are promising.

2.2 Advanced Concept Description

A return to the Moon requires the construction of structures for habitation as well as for manufacturing, farming, maintenance and science. The most challenging of these is the construction of structures that can be used for habitation, although the other mentioned applications each offer unique challenges to the design engineers and, initially, the astronaut construction teams that must erect the structures.

The question is the following: Given the costs associated with bringing material to the Moon (assuming no Space Elevator exists before man returns to the Moon), how do we design and construct habitable structures on the lunar surface in a way that is feasible from mass and energy constraints and minimizes astronaut construction time and risk? What is needed is a small “machine” that can be sent to the Moon and can build structures utilizing primarily in-situ resources and can operate via solar power in conjunction with nuclear power as backup. Therefore, we propose that the use of freeform fabrication technologies by autonomous mini-robots can form the basis for the construction of habitable lunar structures using primarily in-situ resources and

solar/nuclear power. Over a six to twelve month period prior to the arrival of astronauts such a system can potentially erect a near-habitable structure.

Every aspect of this concept and goal has serious technical challenges. Currently we do not have the suite of capabilities needed to autonomously erect structures on the Moon using local resources. We cannot even do this on Earth, where the challenges are less severe.

2.3 The "Grand Vision"

The "grand vision" is the design of freeform fabrication machines that operate almost completely under solar power. One can envision such machines doing most of their work during the lunar day – perhaps during the night as well if battery or nuclear technologies are also included in the equation. Another possibility is to select lunar locations with permanent sunlight.

To analyze this prospect a study is proposed comprising of the following aspects:

1. select a benchmark lunar structure for analysis and which is to be built using the autonomous technologies proposed;
2. establish structural strength of "blocks" built from in-situ/regolith material (what can be expected from such a process ideally and realistically, knowing the kind of efficiencies one can obtain on Earth);
3. estimate if the benchmark lunar structure with the expected strength can combat against lunar environment.

2.4 The Benchmark Lunar Surface Structure

Lunar structural design must be simple to allow the use of basic robot manipulators and control systems. Using teleoperated robots might be possible, but signal transmission delay between Earth and the Moon can pose many challenges to such systems as well.

Moreover, structures for manned habitation must be designed to protect against the extreme lunar surface environment. Some argue that manned structures be buried – and they will be one day as the infrastructure is created on the Moon that is capable to engineer underground structures – but initial forays to the Moon will be modest given our limited capabilities to build on such a hostile environment.

Therefore, a benchmark lunar structure is selected as igloo-shaped structures with the same interior space dimensions as proposed by Ruess et al. (2006). The structure is to be a metallic structure since rapid prototyping technologies have shown great capabilities in manufacturing metallic parts. The structure is envisioned to be protected using a regolith sandbags shielding and be supported on a sintered regolith or a concrete foundation. As it is discussed in the next chapter, sintered regolith in principle can possess material strength higher than lunar concrete. However, lunar concrete technologies are more ready to be used and might be more suitable for autonomous construction.

2.5 Conclusions

In this chapter, based on our previous work (Benaroya et al. 2012), we have presented a conceptual overview of how an automated ISRU effort can create near-habitable structures in advance of the arrival of astronauts on the Moon and eventually Mars and

beyond. Clearly we have extrapolated from currently available technologies in three dimensional printing. These technologies offer the promise that they can be adapted to the hostile lunar environment and can be powered by solar and nuclear generation systems envisioned for the Moon. We have not much discussed the robotics needed for such an automated ISRU system. It appears to us that the printing technologies are further advanced than are the robotics.

Also introduced was a possible design as an igloo-shaped metallic structure with sintered regolith foundation. The structure is to be covered by sandbags regolith shielding for protection against the harsh lunar environment.

Serious challenges exist along the way to the types of systems proposed here. But there can be no settlement of the Moon and beyond without such systems.

Chapter 3. Materials Selection

The construction of structures for long-term habitation, considering the current cost of shipping supplies to the Moon, requires designs that mainly utilize in situ resources and have the least dependency on the material transportation from Earth. Therefore, in this chapter we explore the materials on the Moon and carry out a feasibility study of a proposed material by reviewing the physical properties of it and its alloys.

The proposed lunar structure will rest on a sintered regolith foundation and will be covered by regolith shielding. This chapter is based on our earlier work, Benaroya et al. (2013).

3.1 Materials on the Moon

Regolith has been defined as fragmental and unconsolidated layer of rock material that covers the underlying bedrock layer of the Moon. This fined-grain layer generally covers the upper 3 m to 20 m layer of the Moon (McKay, et al. 1991). Assuming that materials would mainly be refined from regolith, because of heavy machinery needed to mine the deeper layers, we only consider the mineralogy of the upper layer. Table 3.1 shows the average composition of the lunar surface, and Figure 3.1 shows the average composition of lunar regolith. It consists primarily of iron, calcium, aluminum, and magnesium silicates, with small amounts of chromium, titanium, and manganese (Landis, 2007).

Using metal as the constructional material, a choice has to be made between iron, aluminum, and magnesium. Being the most available metal in the regolith, magnesium has not received the same attention as iron and aluminum for lunar applications. It was

suggested, albeit briefly, as viable option by Ruess et al. (2006). Therefore, in the following sections we examine the possibilities of processing and using the relatively abundant magnesium in the lunar regolith as that building material. In the following sections we discuss and summarize those properties of magnesium that add or detract to its use as a structural material on the lunar surface.

Table 3.1. Average composition of major materials on the lunar surface (percent by weight) (adapted from Landis, 2007)

Element	O	Si	Mg	Fe	Ca	Al	Cr	Ti	Mn	H
Amount (wt%)	43.4	20.3	19.3	10.6	3.22	3.17	0.42	0.18	0.12	([a])

[a] Hydrogen: while hydrogen is present in surface soil at approximately 50 ppm by weight, it is a major soil component in high latitude (near polar) craters only.

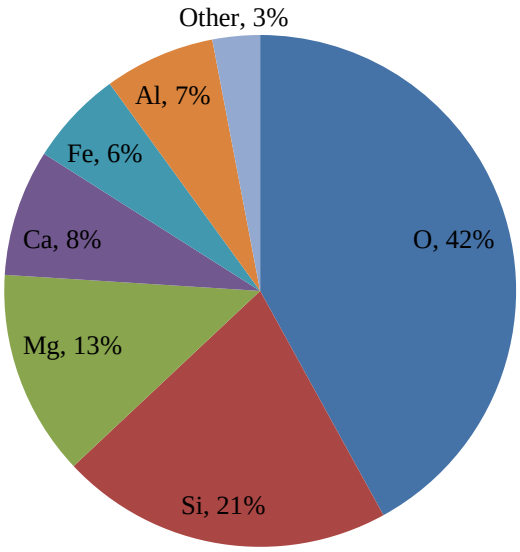

Figure 3.1. Composition of the lunar regolith (adapted from Landis, 2007)

3.2 Magnesium as Structural Material

3.2.1 Advantages

A particularly beneficial factor specific to high extraterrestrial magnesium alloy utilization is its high strength-to-weight ratio, especially in strong alloys such as AZ91, which even outperforms steel (Boby et al. 2011). Although aluminum alloys are typically proposed for such purposes, magnesium alloys have advanced greatly in recent decades and have been shown to have higher relative mechanical properties (property/density) and energy absorption than aluminum and steel (Liu and Taylor 2011). Because of these attributes, magnesium alloys have recently been used in the aerospace and automotive industries: many magnesium engine components are present in aircraft to reduce weight and retain strength.

Magnesium exhibits strong electromagnetic shielding, the effectiveness of which is established by its conductivity and permeability. For example, relative to copper, an excellent conductor, the relative conductivities of the following three metals show magnesium to be a good conductor: Mg (0.36), Al (0.61), and Fe (0.17) (Cortes and Cantwell 2004; Neelakanta 1995). It has been considered, along with aluminum, as a radiation shield for space applications (Wilson et al. 1997; Heinbockel et al. 2011). Its neutron absorption cross-section value is given at 0.0636 ± 0.004 barns/atom (1 barn = 10^{-24} cm^2) (Avedesian and Baker 1999).

Magnesium also has 30 times the vibrational damping of aluminum (Cole 2003) and high impact resistance (Watarai 2006; Shu and Ahmad 2011). These traits of magnesium, one

of the most pervasive metals in lunar soil (Landis 2007), are useful on the Moon for combating moonquakes and meteoroids, respectively.

The low melting temperature of magnesium metal, 650 ± 2 ˚C, is well within the range of the furnace heated by solar concentrators used on Space Station Freedom and as such is achievable on the Moon (Landis 2007; Taylor and Carrier 1993). For comparison, aluminum's melting point is 660 ˚C, that of iron is 1535 ˚C, and that of titanium is a nearly unfeasible 1795 ˚C. Coupled with a latent heat of fusion that is two-thirds and a specific heat that is three-quarters that of aluminum (Cole 2003), these traits allow magnesium to be produced and recycled quickly and with little energy expenditure compared with other metals (Table 3.2).

Magnesium is the most easily machined metal used in engineering designs (Boby et al. 2011; Jayalakshmi et al. 2002) and has excellent castability (Cole 2003; Kaneko and Suzuki 2003; Mordike and Ebert 2001). Thus, magnesium replacement parts could be fabricated from regolith and a CNC (Computer Numerical Control) milling machine, lending to decreased dependence on Earth-based manufacturing.

Magnesium is a diamagnetic material, with a magnetic susceptibility of 1.2×10^{-5} that is close to aluminum's magnetic susceptibility of 2.2×10^{-5}, which equals zero if the material does not respond with any magnetization. Thus, having a slight magnetization can be useful in refining or processing.

Table 3.2. Comparison of Physical Properties of Magnesium with Other Pure Metals (Adapted from Watarai 2006).

	Specific gravity	Melting Point (˚C)	Boiling point (˚C)	Latent Heat of melting (kJ/kg, J/cm^3)	Specific heat (kJ/kg.K, J/cm^3.K)	Coefficient of linear expansion × 10^6	Tensile strength (MPa)	Elongation	Hard-ness (HB)
Mg	1.74	650	1110	368, 640	1.05, 1.84	25.5	98	5	30
Al	2.74	660	2486	398, 1088	0.88, 2.43	23.9	88	45	23
Fe	7.86	1535	2754	272, 213	0.46, 3.68	11.7	265	45	67
Ti	4.54	1795	3287	419, −	0.54, −	8.6	434	18	72

3.2.2 Disadvantages

One of the main deterrents to the widespread use of magnesium is its high reactivity with water and oxygen. However, because the surface pressure on the Moon is about 10^{-12} Torr (1.0325×10^{-7} Pa) (Liu and Taylor 2011) and there is essentially no atmosphere on the Moon, this should not be a significant problem if the magnesium is only used externally on structures. Also, environmental corrosion in new nickel- and iron-free alloys is reportedly lower than that of steel (Cole 2003). These alloys may minimize environmental corrosion to within acceptable levels.

Although its relative properties are advantageous, magnesium has a lower ultimate tensile strength and fatigue strength than aluminum and most structural metals (Cole 2003). This is ultimately made less important by the Moon's gravity, which is one-sixth of the terrestrial value. Furthermore, these minor strength deficiencies can be effectively mitigated by the use of strong alloys (for example, those produced by Magnesium

Elektron Ltd.) and well-designed casts with surface features, cross sections, and ribbing. Postprocessing, which will be covered later, will also improve these qualities.

Magnesium's ignition safety risk is dissipated by the Moon's nearly oxygen-free hard vacuum, yet some risk may linger as a result of oxygen's presence during some stages of regolith refining. It may be possible to take advantage of magnesium's thermal conductivity to quench a localized fire (Cole 2003). Furthermore, the National Institute of Advanced Industrial Science and Technology of Japan has shown that the ignition points of magnesium alloys can be raised 200-300 ˚C by adding calcium (Watarai 2006). Copper conductor rods may be packed in magnesium oxide to act as a seal and fireproof insulator (http://www.micable.com).

Energy expenditure for the magnesium-refining process is large caused by the difficulty of separating MgO from the regolith. Some proposed methods (Landis 2007; Wang et al. 2008; Seboldt et al. 1993, Taylor and Carrier 1993) exist, but researchers and practitioners may favor processes that produce multiple desired products from the lunar soil for increased efficiency. Meanwhile, no study has focused directly on magnesium refining on the Moon, as it is considered refractory.

Although die-casting magnesium mandates costlier materials and more complex machinery with higher clamping pressures and ram speeds than those for aluminum, the average magnesium die life is two (or more) times that of aluminum dies (Cole 2003). As the current shipping cost to the Moon is about $10,000/kg using current rocket fuel (Duke et al. 2006), the additional costs and the higher power requirements of using magnesium

dies are possibly less than the long-term costs of shipments of building materials from Earth. Of course, the goal is to forgo as many shipments from Earth as possible.

The use of magnesium requires, of course, that it be available in sufficient quantities and that an adequate infrastructure exists on the Moon for its extraction and processing.

3.2.3 Availability

Magnesium, overall, is an abundant metal in lunar regolith. The greatest proportions of Mg on the Moon have been observed in olivine in highlands troctolite Sample 76535 (Papike et al. 1991; Duke et al. 2006), which contained up to 47.1 wt% magnesium oxide, the naturally occurring compound containing the metal in lunar soils and rocks. Whereas olivine as a whole is an excellent mineral source for magnesium oxide, with 32 wt%, on average (McCallumet al. 2006), this compound is also readily available in high proportions in several varieties of lunar regolith. In the highlands, magnesium is found in high concentrations in the aforementioned olivine, as well as in norite. To a lesser degree, it is also present in mare regions, especially in high-Ti and low-Ti regolith (Sen et al. 2005). Such mare soils are well represented, in terms of magnesium concentrations, by the JSC-1, JSC-1A, CAS, FJS-2, FJS-3 (Liu and Taylor 2011), and NU-NHT-1 (Miller et al. 2009) regolith simulants, among others (Table 3.3).

Although prospecting for rocks with above-average quantities of Mg is the most efficient method, magnesium concentration will not likely be a main concern when scientists decide the location of a lunar base. Additionally, whereas olivine contains high concentrations of magnesium, it is also a refractory mineral in that it is nearly unrefinable because of its limited reactivity and the high temperature at which it releases oxygen

(Seboldt et al. 1993). Fortunately, however, magnesium oxide usually composes 5 - 6 wt% of bulk highland soils and 8 - 10 wt% of bulk mare soils in reactive minerals, so it is generally present in refinable quantities (Shu and Ahmad 2011; Senior 1993).

Regions near the South Pole are high on the list of potential sites for lunar bases, and the recent discovery of water is a bonus, in addition to the pole's accessibility to Earth, solar wind flux shielding, and minimal temperature variations (Duke et al. 2006). Unfortunately, no soil samples as of yet have been taken south of about 40.86˚ S, the site where Surveyor VII landed. Recently, however, researchers using gamma-ray spectroscopy (GRS) have surveyed the lunar South Pole, providing approximations for magnesium yield in different regions (Shkuratov et al. 2005). GRS images reveal large concentrations of magnesium (up to 16 wt% Mg) in the southern region of the Aitkin Basin, in sites on the far side of the Moon that are within 10 miles from the South Pole 170 – 175˚ W. This location is consistent with the Shackleton crater, which conveniently has been shown to have high concentrations of lunar ice (Campbell and Campbell 2006).

3.2.4 Refining

Any production method on the Moon must minimize the use of carbon and other elements that are nearly nonexistent on the Moon and use recycled reactants to conserve resources; thus, many terrestrial methods, such as carbothermal reduction, are not applicable. One approach to minimizing resource consumption is to use beneficiated soil or magnesium-rich minerals. If pure olivine can be reduced to a mixture of CaO and MgO (Landis 2007), it may not be necessary to do any further separation. Magnesium

may be produced from MgO via a reduction reaction with ferrosilicon (FeSi), the reactants of which are quite available on the Moon

$$2\ CaO(s) + 2MgO(s) + Si(s) \rightarrow 2\ Mg(g) + Ca_2SiO_4(s)$$

This process can take place in the temperature range of 1200 -1500 ˚C in a vacuum. It is a highly endothermic reaction, and the products are gaseous magnesium and a slag of dicalcium silicate.

However, assuming that regolith is to be used, it will be necessary to provide a method for separating out the magnesium from the mixture of elements. Many methods exist for attaining pure magnesium from regolith; reasonably, this usually occurs during the production of oxygen and other metals to conserve energy, using a method such as the caustic solution and electrolysis method proposed by Binder (1990) and Curreri et al. (2006). This process and other similar procedures have been ruled out by some researchers for involving high power requirements and overly complex schemes (Taylor and Carrier 1993). However, recent research on Joule-heated reactors appears to mitigate some of the aforementioned drawbacks of the direct electrolysis method (e.g., Vai et al. 2010).

A fluorination procedure proposed by Landis (2007) seems comparatively promising, notwithstanding its complexity or the terrestrially supplied reagents that must be recovered, as its feedstock does not require benefaction, and it thoroughly refines nearly every constituent of regolith. When regolith is heated in the presence of fluorine, oxygen is displaced in all of the metal oxides. After the removal of volatile fluorides and oxygen and the reduction of the potentially useful iron and aluminum from their fluoride salts,

MgF_2 and CaF_2 may be reacted back to their oxide salts with K_2O. Subsequently, this mixture may react with FeSi in the above reaction. Needless to say, this is a complicated scheme; significant drawbacks to its feasibility are its considerable electrical power consumption and the risks associated with the transport and use of highly reactive fluorides.

Table 3.3. Composition of Major Constituents in Lunar Regolith Samples, by wt% (Adapted and Compiled from Sen et al. 2005; Duke et al. 2006; and Papike et al. 1991 and the References Listed in the Notes Below).

	Mission averages				**Mare rocks**				**Highland rocks**		**Olivine samples**	
	Apollo 14 (Maria)	Luna 16 (Maria)	Luna 20 (high-lands)	Apollo 16 (high-lands)	High Ti High Ti	Low Ti	Very low Ti	Al-rich	Troctolite	Norite	In low-Ti mare basalt 12035	In highlands troctolite 76535
MgO	9.24	8.78	9.19	5.96	7.8	9.7	6.0	8.5	19.1	12.9	30.1	47.1
SiO_2	47.93	41.70	45.40	44.94	39.7	45.8	46.0	46.4	42.9	51.1	35.4	39.9
Al_2O_3	17.6	15.33	23.44	26.71	9.5	9.6	12.1	13.6	20.7	15.0	0.00	0.00
CaO	11.19	12.50	13.38	15.57	11.2	10.2	11.6	11.2	11.4	8.8	0.36	< 0.02
FeO	10.37	16.64	7.37	5.49	19.0	20.2	22.1	16.8	5.0	10.7	33.8	12.0
TiO_2	1.74	3.38	0.47	0.58	11.2	2.8	1.1	2.6	0.05	0.34	0.00	0.00
Cr_2O_3	–	–	–	–	0.37	0.56	0.27	0.4	0.11	0.38	0.11	< 0.02
Na_2O	–	–	–	–	0.38	0.34	0.26	0.4	0.20	0.38	–	–
References	(1)	(1)	(1)	(1)	(2)	(3)	(4)	(5)	(6)	(7)	(8)	(9)

Note: (1) Compiled by Sen et al. 2005. (2) Average of Apollo 11 and 17 low-K high-Ti mare basalts (Haskin and Warren 1991). (3) Average of Apollo 12 and 15 low-Ti basalts (Haskin andWarren 1991). (4) Luna 24 rock fragment 24174, 7 (Taylor et al. 1991). (5) Apollo 14 aluminous mare basalt 14053; with Cr and Na from average of 14,321 Group 5 (Taylor et al. 1991). (6) Troctolite 76535 (Table A5.33 in Papike et al. 1998). (7) Typical norite 77075 (Table A5.33 in Papike et al. 1998). (8) Olivine in low-Ti mare basalt 12035. (9) Olivine in highlands troctolite 76535.

Nevertheless, keeping with the goals of ISRU, the most desirable refinement process would have simple steps and would not require great quantities of electricity to run. Senior (1993), whose work details vapor pyrolysis, may have been on the right track toward such a procedure. The pyrolysis process involves heating bulk regolith to approximately 2000 - 2200 ˚K, which is acceptable in modern solar furnaces, and although it produces oxygen, it may be configured to isolate and remove Mg (or Na, Fe, or Si) by vacuum distillation onto a temperature-controlled condensing surface. There exist multiple obstacles in the process, such as a somewhat low efficiency and the need for further testing of the condensation subsystem, but further examination of this approach may be pivotal to self-sustainable lunar magnesium refining.

3.2.5 Alloying and Grain Refining

Magnesium alloys are significantly more useful than pure magnesium because of their vast benefits to both physical and chemical properties. In the casting process, fine grain size is important for service performance of cast products and the final properties of fabricated products. For casting Mg alloys, a choice between high pressure die casting (HPDC), sand casting, permanent mold casting, and direct chill billet casting must be made. In HPDC, as the rates of solidification are extremely high, there is usually no need to add a grain-refining agent. This is not true for other mentioned casting methods (StJohn et al. 2005). When designating an alloy to investigate further for lunar applications, the availability of its components on the Moon should first be determined and then an alloy with properties well suited for the required application should be chosen.

Magnesium alloys are generally classified into two broad groups: aluminum bearing and aluminum free. For aluminum-free alloys, zirconium (Zr) is usually added as a grain-refining agent (StJohn et al. 2005; Qian and Das 2006). Although Zr is a trace element (trace minerals never exceed a few tenths of a percent) in the form of $ZrSiO_4$ and ZrO_4 (Williams and Jadwick 1980), aluminum constitutes an average of 3.17% wt on the lunar surface (Landis 2007). Therefore, only aluminum-bearing alloys of magnesium are considered, thus eliminating the need to transport Zr to the Moon.

One of the most promising magnesium alloys is AS41. This alloy has reasonable structural strength, good ductility, and retains its creep resistance at high temperatures (Boby et al. 2011). In addition, most of its components are available on the Moon, making it a viable candidate for lunar utilization. Other noteworthy alloys are Elektron 675 and Elektron 21, which have mechanical properties comparable to steel and aluminum alloys used in aerospace structures, respectively (Magnesium Elektron Ltd. 2011a, d; Ostrovsky and Henn 2007). Some common magnesium alloys and their mechanical properties and chemical composition are presented in Table 3.4.

The following is a summary of possible alloying elements, considering their availability on the lunar surface.

Manganese

Mn is included mostly for decreasing the brittleness induced by iron in the alloy and increasing corrosion resistance in wet conditions (Polmear 1994). Also, it should be considered that Mg-Al alloys with low Fe and Mn content are less susceptible to superheating treatment than alloys with high Fe and Mn content (StJohn et al. 2005).

Thorium

There are uncertainties regarding the abundance of Th on the lunar surface, ranging in trace quantities from 0.13 to 5.38 ppm, the South Pole Aitken Basin has average Th concentrations of 2 - 3 ppm with highs reaching 6 ppm (Lawrence et al. 2000; Hagerty et al. 2011), but thorium is still worth taking note of because it is the most effective alloying element known to significantly improve the high temperature properties of magnesium (Mordike 2002). Th percentage in the alloy might be of concern; for instance, in Britain, alloys containing more than 2% of thorium are classified as radioactive materials (Luo and Pekguleryuz 1994).

Silicon

Si constitutes on average 20.3% of the lunar surface (Landis 2007), and when added to magnesium with a low iron content, it favors grain refinement by superheating.

Rare Earth Metals

Addition of rare earth metals increases the strength of magnesium alloys at elevated temperatures. Their addition also reduces weld cracking and porosity during casting (Avedesian and Baker 1999).

Considering the difficulties associated with sand casting with regolith, because of its low melting point, die-casting methods may be more favorable for lunar production. However, sand casting is possible with the addition of binders (Avedesian and Baker 1999).

Regarding the major alloying elements in Table 3.4, aluminum, manganese, titanium, and silicon, constitute 3.17, 0.12, 0.18, and 20.3 wt% of the lunar surface (Landis 2007), whereas zinc, thorium, neodymium, gadolinium, zirconium, and copper are either nonexistent or are present as trace elements on the Moon. If needed, they should be transported from Earth. Some of the alloying elements included in Table 3.4 are used to allay terrestrial conditions that are not present on the Moon.

Although as-cast alloys may be adequately sound for structural applications, postprocessing would further benefit components. Most notably, laser (Ng et al. 2011), thermal treatments, and spray coatings (Pokhmurska et al. 2008) of magnesium alloys may add to their mechanical properties while bolstering corrosion and wear resistance.

Different approaches to obtain grain refinement are superheating, grain refinement by means of other additives, carbon inoculation, and grain refinement by FeCl3 (the Elfinel process) (StJohn et al. 2005). The last two methods can be ruled out because of the very low quantities of carbon and chlorine on the Moon. Superheating involves heating the melt to a temperature well above the liquidus of the alloy (often 180 – 300 ˚C) for a short time, followed by rapid cooling. Because there are no known grain-refinement agents for alloys such as AM50, AM60, and AZ91, HPDC is the only option on Earth and on the lunar surface.

Luo and Pekguleryuz (1994) discussed a 1960 Russian paper that reported the addition of calcium to sand cast Mg-A1-Zn alloys for improved tensile strength and creep resistance at elevated temperatures. Later, calcium was also found to be effective in improving the creep resistance of die-cast Mg-Zn-A1 alloys without adversely affecting corrosion

resistance. The resulting die-cast alloy, ZA102 (Mg-10%, Zn-2%, A1-0.7%, Mn-0.3%,Ca),was claimed to be creep resistant at temperatures up to 177 ˚C. It is doubtful but unknown whether alloys of this type are being used outside Russia at the present time. A Ca-modified sand cast AS41 alloy might provide a cost-effective alternative to Zr-containing alloys.

3.3 Regolith Bulk Densities

Physical properties of lunar regolith are known with a high degree of confidence for the upper 3 m of the lunar surface (direct sampling was limited to 3 m). In situ measurements have been made at the five Surveyor landing sites, at Apollo 15 and 16 landing sites, and at the Luna 16, 20, and 24 landing sites. Also, additional information has been obtained from detailed studies of photographs and television coverage during Apollo missions (Williams and Jadwick, 1980).

Bulk density is a property of granular solids and is defined as the mass of all the particles per unit occupied volume. Table 3.5 presents the best estimated average bulk densities of the regolith on lunar surface (Williams and Jadwick, 1980), although other densities have been estimated based on the data obtained by the Apollo Heat Flow Experiments (see “Thermal Control at Lunar Base”).

Table 3.4. Magnesium alloys and Their Properties.

	AZ31 BO	AZ31BH24	HM 21AT8	Elektron 21	Mg-Al_3Ti	Mg/3.9Cu$_p$	AS41 hp	AZ91D
Tensile Yield Stress (MPa)	150	220	160-170	145	-	355±8	140	150
Compressive Yield Stress (MPa)	110	180	130	168	-	-	-	165
Ultimate Tensile Stress (MPa)	255	290	235-250	248	-	358±7	215	230
Ultimate Compressive Stress (MPa)	-	-	-	-	319.34	-	-	-
Bearing Yield Stress (MPa)	290	325	270	-	-	-	-	-
Shear Strength (MPa)	145	160	125	(ultimate) 172	-	-	-	(ultimate) 140
Coefficient of Thermal Expansion (μm/m˚C)	(20˚C) 26	(20˚C) 26	(20˚C) 26.8	25.3	(40-400˚C) 22.89	27.0 ±0.4	26.1	25
Density (g/cm^3)	1.77	1.77-1.83	1.77-1.78	1.78	2.0861±0.06	2.076 ±0.051	1.77	1.81
Young's Modulus, E (GPa)	45	45	45	44	-	47±1	45	45
Shear Modulus, G (GPa)	17	17	17	-	-	-	-	16.5
Poisson's Ratio, v	0.35	0.35	0.35	0.27	-	-	0.35	0.35
Major Elements (wt%)	Al 2.5-3.5 Zn 0.7-1.3 Mn 0.2-1.0 Mg Balance	Al 2.5-3.5 Zn 0.7-1.3 Mn 0.2-1.0 Mg Balance	Al 3.3 Mn 0.6 Th 2.00	Zn 0.2-0.5 Nd 2.6-3.1 Gd 1-1.7 Zr saturated Mg Balance	Al Ti Mg	Cu 3.9 Mg Balance	Al 3.5-5.0 Zn 0.2 max Mn 0.1 min Si 0.5-1.5	Al 8.5-9.5 Mn 0.17-0.3 Zn 0.45-0.9 Si 0.05 max Cu .025max Mg Balance
References	Alderlieste n et al. 2008; Superform Aluminum 2010	Alderlieste n et al. 2008; Superform Aluminum 2010	Alderlieste n et al. 2008;eFunda	Magnesium Elektron Ltd. 2011d	Yang et al. 2008	Hassan et al. 2004	Senf et al.2000; Int'l Mg Assoc	Int'l Mg Assoc; Magnesium Elektron Ltd. 2011e

Table 3.4 (Continues)

	AM50A	AM60 B	Elektron A8 sand cast	Elektron A8, sand cast, solution treated	AS21	AE42	AE44	AM20-F	Elektron 675
Tensile Yield Stress (MPa)	120	130	85	80	121 ±3	135	142	89.6	310
Compressive Yield Stress (MPa)	-	130	75-90	75-90	-	135	-	89.6	-
Ultimate Tensile Stress (MPa)	220	220	140	200	232 ±6	240	245	214	410
Ultimate Compressive Stress (MPa)	-	-	-	-	125	-	-	-	-
Bearing Yield Stress (MPa)	-	-	-	-	-	-	-	-	-
Shear Strength (MPa)	-	-	-	-	-	-	-	-	-
Coefficient of Thermal Expansion (μm/m˚C)	26	25.6	27.2	27.2	26.1	26.1	25.2	26-27	27.4
Density (g/cm^3)	1.79	1.78	1.77	1.77	1.76	1.79	1.82	1.78	1.95
Young's Modulus, E (GPa)	45	45	44	44	45	45	45	45	-
Shear Modulus, G (GPa)	-	-	-	-	-	-	-	17	-
Poisson's Ratio, ν	-	0.35	0.35	0.35	-	-	-	0.35	-
Major Elements (wt%)	Al 4.5-5.3 Mn 0.28-0.5 Zn 0.20 max Si 0.05 max Mg Balance	Al 5.6-6.4 Mn 0.26-0.5 Zn 0.20 max Si 0.05 max Mg Balance	Al 8.0 Zn 0.5 Mn 0.3 Mg Balance	Al 8.0 Zn 0.5 Mn 0.3 Mg Balance	Al 2 Mn 0.4 Si 1 Mg Balance	Al 4 RE 2.5 Mn 0.2 Mg Balance	-	Al 2.1 Mn 0.1 Mg Balance	-
References	Magnesium Elektron Ltd. 2011e	Int'l Mg Assoc; Magnesium Elektron Ltd. 2011e	Magnesium Elektron Ltd. 2011b,c	Magnesium Elektron Ltd. 2011b, c	(1)	(2)	(3)	Morgo Mg	Magnesium Elektron Ltd. 2011e

(1) Int'l Mg Assoc; Magnesium, Gupta and Sharon 2011; Meridian Technologies. (2) Int'l Mg Assoc; Magnesium, Gupta and Sharon 2011. (3) Meridian Technologies

Table 3.5. Best estimated average bulk densities of the regolith (adapted from Williams and Jadwick 1980).

Depth Range, cm	**Bulk Density, g/cm^3**
0 to 15	1.50 ± 0.05
0 to 30	1.58 ± 0.05
30 to 60	1.74 ± 0.05
0 to 60	1.66 ± 0.05

3.4 Foundation

As mentioned earlier, our vision is a metallic structure supported on a sintered regolith foundation. However, very little satisfactory research has been carried out on this subject. Therefore, in addition to sintered regolith, we briefly review the characteristics of cast regolith and lunar concrete that may be suitable substitutes to sintered regolith.

3.4.1 Sintered Regolith

Loose regolith can be collected, placed into forms, compressed, and heated via microwaves or solar energy to sinter or fuse. The sintering temperature is usually several hundred degrees below the melting point. Lunar regolith sinters at 1000 - 1100 ˚C, but by adding suitable binding agent it can sinter at 150 – 500 ˚C. Sintered regolith simulant generally has low and highly variable mechanical strength. The material is highly heterogenous and the material properties are difficult to characterize exactly. Reported values for the modulus of rupture (flexural strength) vary from 9 – 18 MPa (1300 – 2600 psi) (Happel 1993).

Although the mechanical properties of sintered regolith are poorly understood and it was not considered as suitable material for a lunar structure (Happel 1993), recent advancements are promising. For instance, Hobosyan and Martirosyan (2012) have

shown that use of local lunar resources with low concentration of aluminum (about 12 wt %) will permit the utilization of more than 85 wt % of the regolith for the fabrication of dense and solid ceramic materials for building structures.

3.4.2 Cast Regolith (Cast Basalt)

Cast regolith has been suggested as a building material for the Moon. The use of cast regolith (basalt) is very similar to terrestrial cast basalt. The terms have been used interchangeably in the literature to refer to the same material. It has been suggested that cast regolith can be readily manufactured on the Moon by melting regolith and cooling it slowly so that the material crystallizes instead of turning into glass. Virtually no material preparation is needed. The casting operation is simple requiring only a furnace, ladle and molds. Vacuum melting and casting should enhance the quality of the end product. More importantly, there is terrestrial experience producing the material; but it has not been used for construction purposes yet (Happel 1993).

Cast basalt has extremely high compressive and moderate tensile strength. It can easily be cast into structural elements for ready use in prefabricated construction. Feasible shapes include most of the basic structural elements like beams, columns, slabs, shells, arch segments, blocks and cylinders.

Cast basalt has the disadvantage of being brittle. Tensile loads that are a significant fraction of the ultimate tensile strength need to be avoided. The fracture and fatigue properties need further research. One possibility is to reinforce it with high tensile strength materials such as locally manufactured magnesium or aluminum or with carbon nanotubes (Alford et al. 2006).

It should also be feasible to use cast regolith in many structural applications without any tensile reinforcement because of its moderately high tensile strength (Table 3.6). However, a minimum amount of tension reinforcement may be required to provide a safe structure. The reinforcement could be made with local materials as well. These local materials would also have to be derived from ISRU manufacturing and refining processes that have yet to be developed and tested.

Since it is extremely hard, cast regolith has high abrasion resistance. This is an advantage for use in the dusty lunar environment. It may be the ideal material for paving lunar rocket launch sites and constructing debris shields surrounding landing pads. However, the hardness of cast basalt combined with its brittle nature makes it a difficult material to cut, drill or machine. Such operations should be avoided on the Moon. Production of cast regolith is energy intensive because of its high melting point. The estimated energy consumption is 360 kWh/MT.

3.4.3 Lunar Concrete

The basic material needed for the manufacturing of lunar concrete are aggregate, water, and cement (Happel 1993), however, sulfur (waterless) concrete has also been proposed by replacing cement and water with sulfur (Toutanji et al. 2012).

Regarding water-containing concrete, properly screened and sized lunar regolith makes high quality concrete aggregate. Small quantities of actual lunar regolith have been used as aggregate in the preparation of concrete in the laboratory (Happel 1993). The mechanical properties of the resulting concrete are shown in Table 3.7.

Toujanji et al. (2012) measured compressive strength to be equal to 31.0 MPa for sulfur concrete consisted of JSC-1 Lunar Regolith Simulant (65%) and sulfur (35%).

Table 3.6. Physical and mechanical properties of cast regolith (adapted from Happel 1993).

Tensile Strength	34.5 MPa (5000 psi)
Compressive Strength	538 MPa (78000 psi)
Modulus of Elasticity, E	100 GPa (14×10^6 psi)
Fracture Toughness, k_{Ic}	2 MPa $m^{0.5}$, ±50%
Melting Point	1300 ˚C
Poisson's Ratio	0.28
Mohr's Hardness	8 - 9
Mass Density	3 g/cm^3

Table 3.7. Mechanical properties of the lunar concrete (adapted from Happel 1993).

Modulus of Rupture	8.3 MPa (1200 psi)
Compressive Strength	39 – 75.7 MPa (5.5 – 10.9 kpsi)
Modulus of Elasticity, E	21.4 GPa (3.1×10^6 psi)
Specific Weight	2.6

3.5 Summary

We have outlined the material properties of several materials found on the Moon that may be suitable for construction of lunar surface structures. Specifically, we proposed the possibility of using magnesium as a structural material for lunar structures. Therefore, in

next chapter we choose magnesium to be the structural material for the benchmark structure suggested in Chapter Two and design our typical lunar habitat.

Chapter 4. Static Analysis and Design Configurations

As mentioned earlier, the geometry of the lunar base considered here is based on the igloo-shaped lunar base proposed by Ruess et al. (2006). Considering this design with magnesium as the structural material, it is natural to assume that the wall thickness needed should be small in comparison with the radius of the structure. Since thin walls offer little resistance to bending, it can be assumed that the internal forces result in internal loads tangent to their surface. This method is referred to as membrane analysis in classical mechanics of materials.

We begin with a simple model and an appropriate factor of safety to analytically estimate the wall thickness needed. Then we use a CAD model drawn in Solidworks and ANSYS® Academic Research Workbench, Release 13.0 to carry out a finite element analysis to verify the preliminary geometric values selected and to modify the design, if needed.

4.1 Thin-walled Pressure Vessels

Cylindrical or spherical thin-walled pressure vessels are those with ratios of inner radius, r, to wall thickness, t, greater than 10. Such pressure vessels can be analyzed as a plane stress problem (membrane analysis). Several assumptions are made:

- Plane sections remain plane.
- The ratio $t/r \leq 0.1$ with t being uniform and constant.
- Material is elastic, isotropic and homogenous.
- The resultant stresses are less than the proportional limit.

- The applied pressure, *P*, is the gage pressure, i.e., the relative pressure of inner pressure with respect to outer pressure.
- Stress distributions throughout the wall thickness are constant and equal to the average stress.
- The cross section is selected so that it is far from geometric discontinuities.
- The fluid/gas contained has negligible weight compared to the pressure.

If these conditions can be satisfied, the stress distributions can be found by considering the free body diagram of an appropriate cut section and by using static equilibrium equations. More discussions on this topic can be found in any introductory mechanics of material books e.g., Beer et al. (2006) and Hibbeler (2011).

4.2 Regolith Shielding Thickness

We start the design procedure by specifying the thickness of regolith shielding. The shielding layer should be thick enough to protect the base from solar flare radiation, extreme temperature fluctuations, and meteoroid impacts. Duke et al. (1985) proposed that a 2 m thick regolith layer can protect the base against the solar flare radiation. Also, Vaniman et al. (1991) mentioned that an insulating blanket of about 30 cm of regolith is sufficient to dampen out about 280 ˚K lunar surface temperature fluctuations based on the data obtained during the Heat Flow Experiments of Apollo. Neither of these papers provide a detail calculation.

Considering the thicknesses proposed and taking into account that the shielding layer should also protect the base against meteoroid impacts, we choose a 3 m thick regolith shielding as is generally accepted in the literature.

4.3 Estimating the Thickness of the Walls

Although the proposed base structure contains geometric discontinuities, simple analytical calculations of the form used for pressure vessels provide us with a good estimate of the needed thickness. The value obtained for the thickness by this method is, however, more likely to be less than what is needed due the fact that this method does not consider stress concentrations, i.e., regions around the holes (doorways) and sharp edges, nor does it consider bending stresses. In order to correct the values of stress around the doorways we will use a stress-concentration factor. Also, we will neglect the stress concentrations about sharp edges, because we will use fillets to cancel those out. Also, we will consider a thicker wall to compensate for bending stresses.

In order to estimate the required thickness, we consider the sectioned volumes (see Figure 4.1) of the base and write the equilibrium equations.

From mechanics of materials, we know that for pressure vessels, the hoop stresses are more significant than longitudinal stresses. Writing the static equilibrium equation for the free-body diagram of Fig. 4.1b, we obtain,

$$PA = A_t \sigma_{allow} \, , \tag{4.1}$$

where A is the cross-sectional area under air pressure, A_t is area of the wall of uniform thickness t, P is the gauge pressure, and σ_{allow} is the allowable stress, defined as the ultimate tensile strength of the material (σ_u) divided by an appropriate factor of safety ($F.S.$),

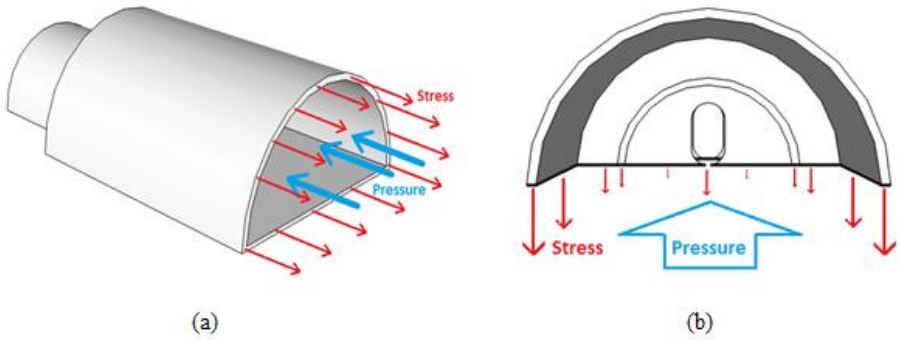

Figure 4.1. Sectioned areas and acting forces.

$$\sigma_{allow} = \frac{\sigma_u}{F.S.} \ . \tag{4.2}$$

While writing Equation 4.1 we assumed the structure contains no geometric discontinuities, we expect high localized stresses about the doorways of the structure. In order to account for such stress concentrations, the allowable stress must be corrected by a stress-concentration factor (*K*), defined as the ratio of maximum stress to the average stress computed in the section of discontinuity,

$$K = \frac{\sigma_{max}}{\sigma_{allow}} \ . \tag{4.3}$$

Therefore, by substituting Equations 4.2 and 4.3 into 4.1, we obtain,

$$PA = A_t \frac{1}{K} \frac{\sigma_u}{F.S.} \ . \tag{4.4}$$

The stress-concentration factor is obtained experimentally through the use of a photoelastic method (Beer et al. 2006). In order to estimate this factor, we used the values obtained for flat bars with a hole under axial loading (see Fig. 4.2).

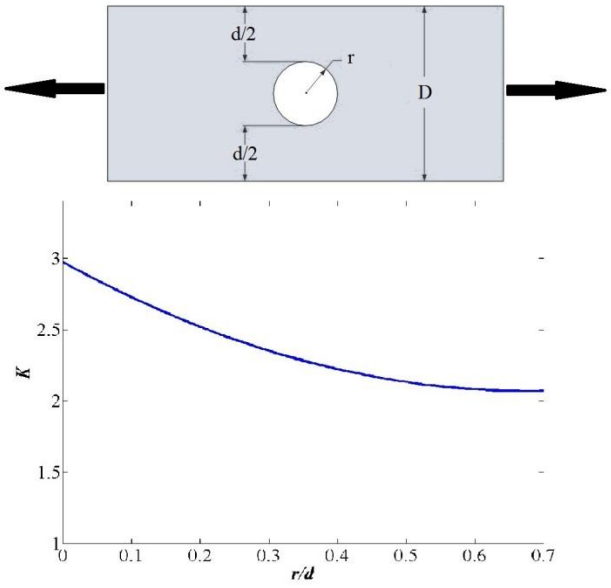

Figure 4.2: Stress concentration factors for flat bars with hole under axial loading (adapted from Beer et al. 2006).

Considering the cross-sectional area like that in Fig. 4.1b in the vicinity of the floor and by subtracting the doorway holes (see Fig. 4.3), values of A and A_t are obtained equal to 150, 50 × t m^2, respectively. Using Fig. 4.2 for a wall of diameter 3 m for the calculation of the stress concentration factor, r/d is equal to 1/(10-2) = 0.125, therefore, K is estimated to be 2.65. The low gravitational acceleration of the Moon (about one sixth of Earth) allows us to neglect the weight of the sandbags by simply considering the gauge pressure, P, equal to the internal pressure of 1 atm (1.01325×10^5 Pa). The factor of safety is chosen to be very high, of the order 4 or 5, even though such a structure can be adequately designed with a much smaller factor of safety. Substituting these values in Equation 4.4, where the ultimate tensile strength of pure magnesium is 21 MPa, the required thickness of the shell is 0.192 m for a factor of safety of 5.

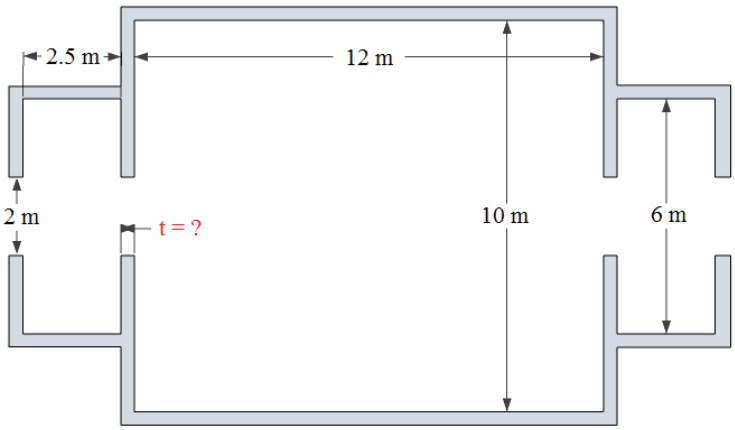

Figure 4.3: Cross-sectional areas in vicinity of the base's floor

4.4 The Design

The approximate wall thickness of equal to 0.192 m (7.56 in) was obtained by using the equilibrium equations and moderating the stress concentrations at the sharp edges by using fillets at the corners. Note that the approximated value is more likely underestimating the thickness because: First, the walls are subjected not only to tensile forces but also to transverse loads (that causes bending stresses). Second, the location of the hole must be far from geometrical discontinuities, which is violated here. Choosing the value of the thickness, t = 0.229 m (9 in) and the inside dimensions as shown in Figure 4.3, the computer aided design (CAD) model of the lunar base is presented in Fig. 4.4. It can be observed in the figure that the sharp edges have been smoothed. The engineering drawing of the base can be viewed in Fig. 4.5.

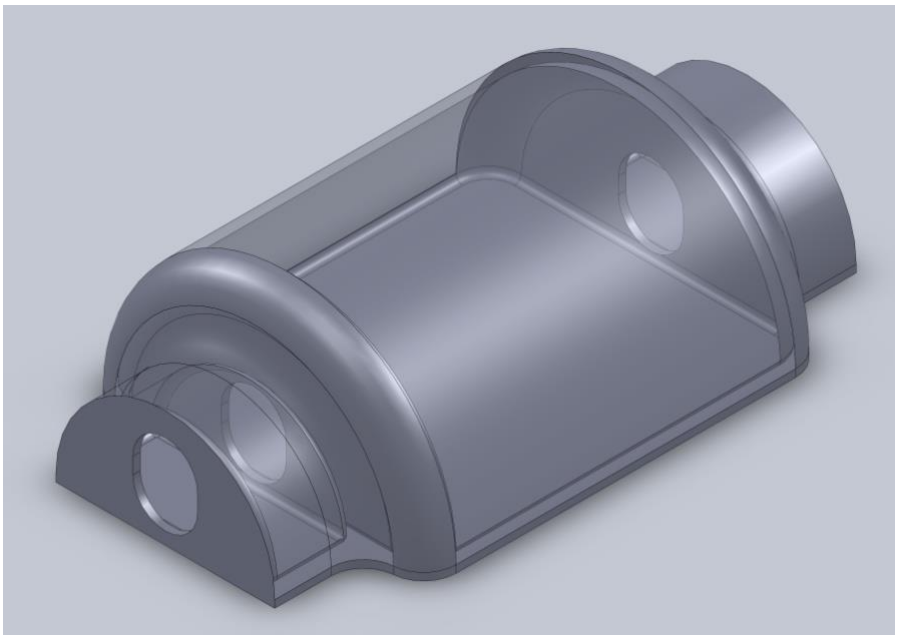

Figure 4.4: The lunar base CAD model (Drawn in Solidworks).

4.5 Finite Element Analysis

4.5.1 The Problem Setup

The structure is considered to be fixed to a foundation. A uniform pressure of 1 atm (1.01325×10^5 Pa) is acting on all interior surfaces. In order to account for the forces applied by the regolith shielding, the bulk density of the regolith is estimated to be 1650 kg/m^3. The bulk densities of the regolith ranges from about 1500 to 1740 kg/m^3 within the upper 1 m layer of the Moon (Williams and Jadwick 1980). The weight results in a uniform downward pressure of 8096 Pa (density × thickness) (see Fig. 4.6).

The physical properties of the magnesium structure is considered to be the same as for sand cast magnesium (Avedesian and Baker 1999), i.e., Young's modulus = 40 GPa, tensile (compressive) yield strength = 21 MPa, Poisson's ratio = 0.35, and density = 1738

kg/m^3. Also, the lunar gravitational acceleration is taken as one sixth terrestrial, 1.64 m/s^2, and results in a body force on the structure.

4.5.2 Numerical Results

ANSYS Academic Research Workbench, Release 14 has been used for the finite element analysis. The ANSYS defaults "Mechanical" have been used to generate the mesh which resulted in 141,554 nodes and 86,531 elements. The generated elements are SOLID187 type (*see* Appendix 1, Section A1.5.1).The results for maximum principal stress, total deformation, factor of safety, and stress intensity are presented in Figures 4.7, 4.8, 4.9, and 4.10, respectively. Also, structural error, which indicates inadequacies in the generated mesh, is presented in Figure 4.11.

4.6 Discussions and Conclusions

As we expected from the analytical calculations, a uniform structural thickness of 0.229 m (9 in) leads to the factor of safety greater than 5 (Fig. 4.9). Naturally, we expect to have higher factors of safety for most parts of the structure, because the chosen thickness for the structure was based on the stress concentration about the doorway. Considering Figure 4.9, it is obvious that such a structure with the same thickness, modified by adding few extra supports can easily achieve higher safety factors. For example, adding a few ribs on the walls containing the exterior doors will increase the section properties by lessening the stress concentration and will result in a safety factor equal to 6 or higher (see Fig. 4.12). We did not modify or optimize the structural design since the purpose of this research work is to show the feasibility of considering this type of structure for a lunar base utilizing magnesium as a structural material.

Also, we have selected the physical properties of sand-cast pure magnesium, which possesses the lowest strength among unalloyed processed magnesium (using other methods, i.e., extrusion, hard rolled sheets, and annealed sheet). This was due to the fact that rapid prototyping techniques generally result in structures with less strength when compared with other methods of manufacturing, and also mechanical properties of rapid prototyped magnesium could not be found.

Naturally, when designing such structures, an alloy will be selected. Most magnesium alloys possess an ultimate tensile strength of about 5 times larger than the sand-cast magnesium considered here. This affords us the possibility of designing much thinner-walled structures, saving material and time.

In the next chapter, we use the structural design obtained in this chapter to carry out the thermal analysis in order to evaluate the effectiveness of the three-meter-thick regolith shielding in protecting the structure from temperature fluctuations. Also, the effect of uncertainties associated with the regolith thermal properties is studied.

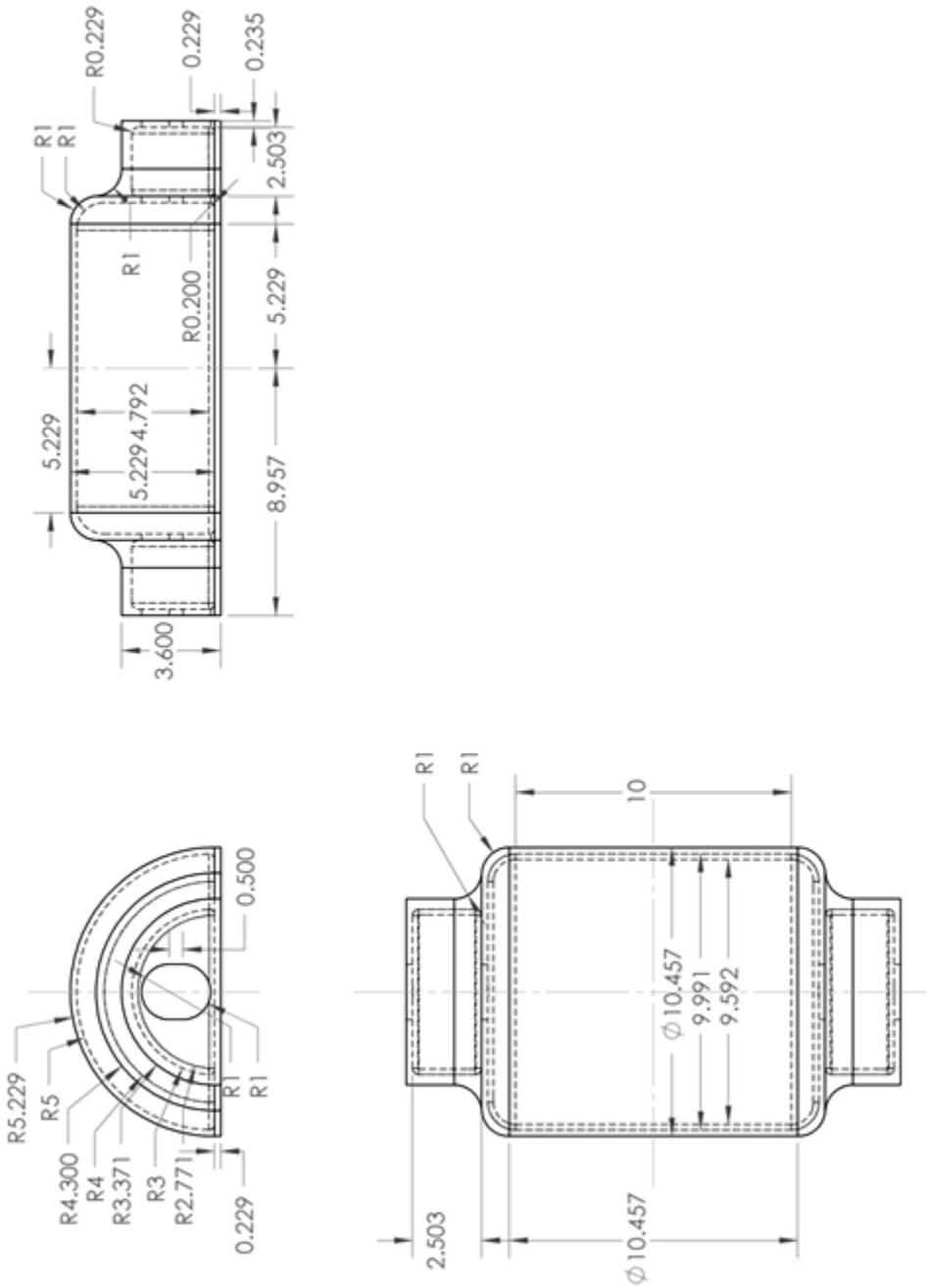

Figure 4.5: Engineering drawings of the final design (All dimensions are in meters).

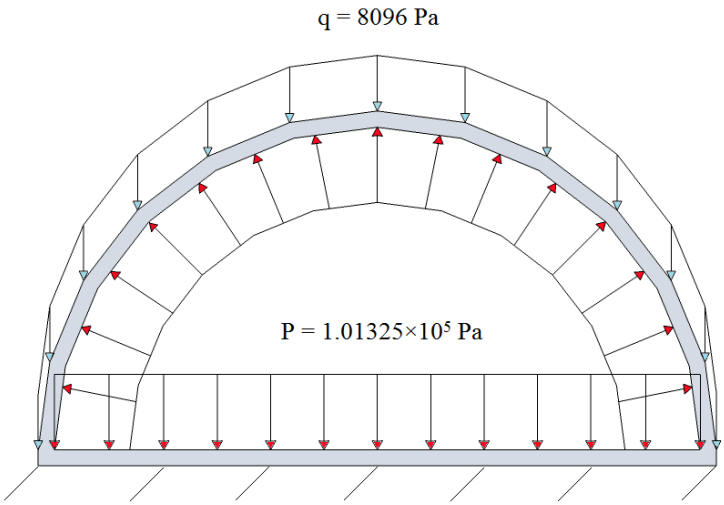

Figure 4.6: Loading conditions, where P and q are the internal air pressurization and regolith weight per unit area, respectively.

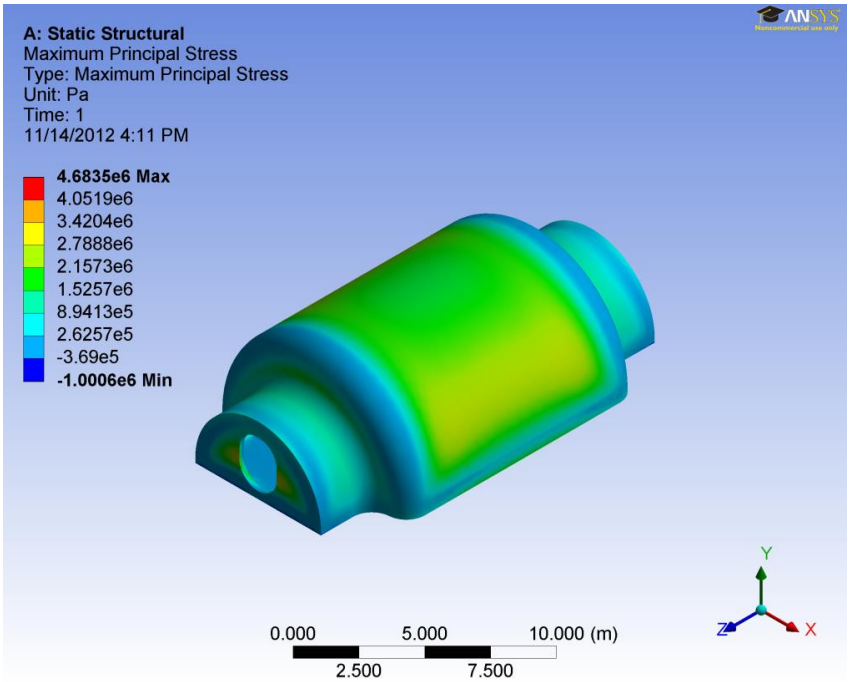

Figure 4.7: Maximum principal stresses.

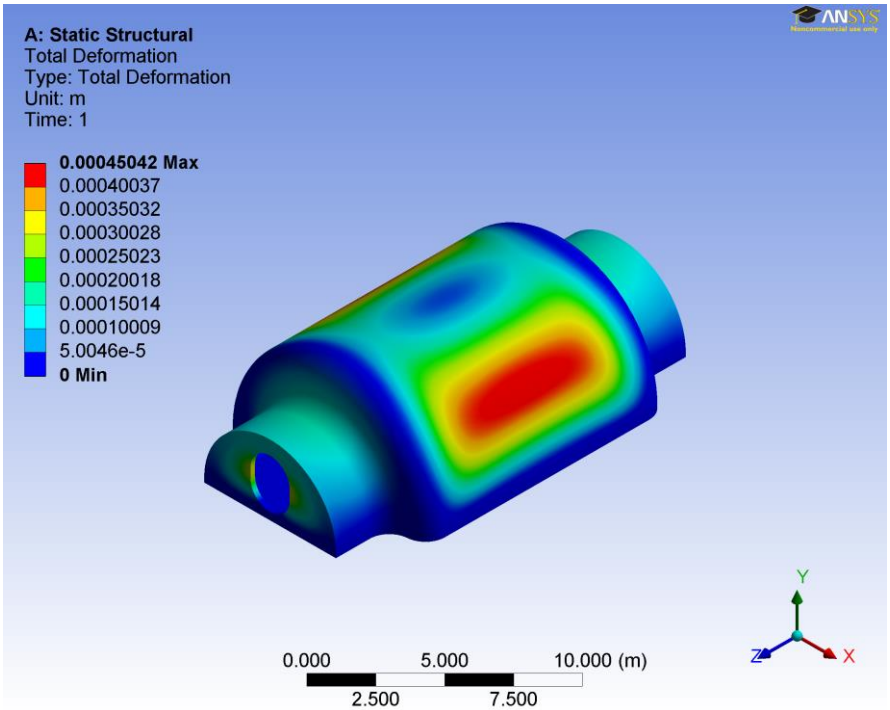

Figure 4.8: Total deformation.

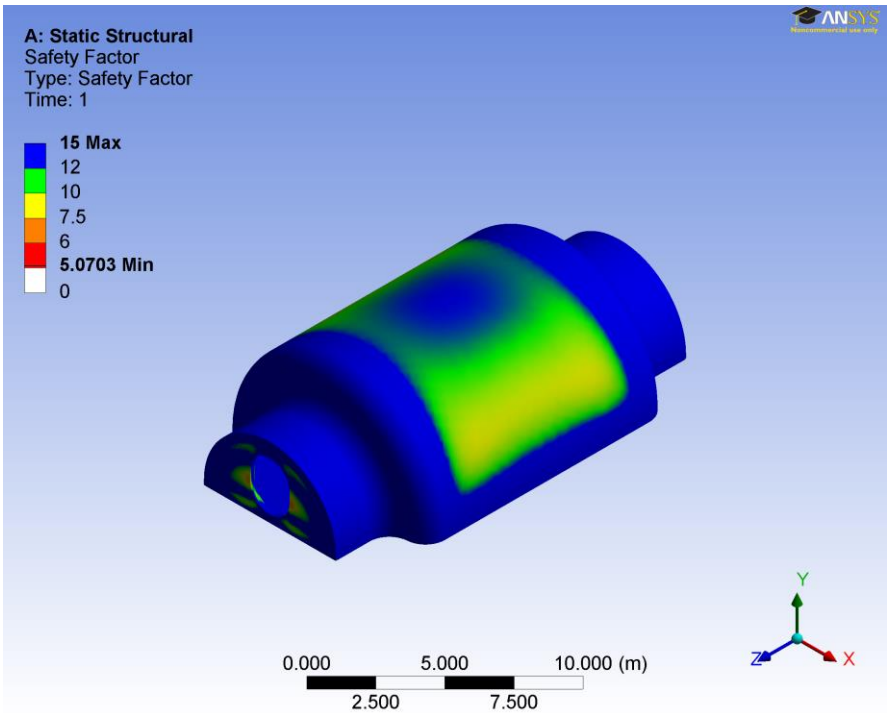

Figure 4.9: Factor of safety.

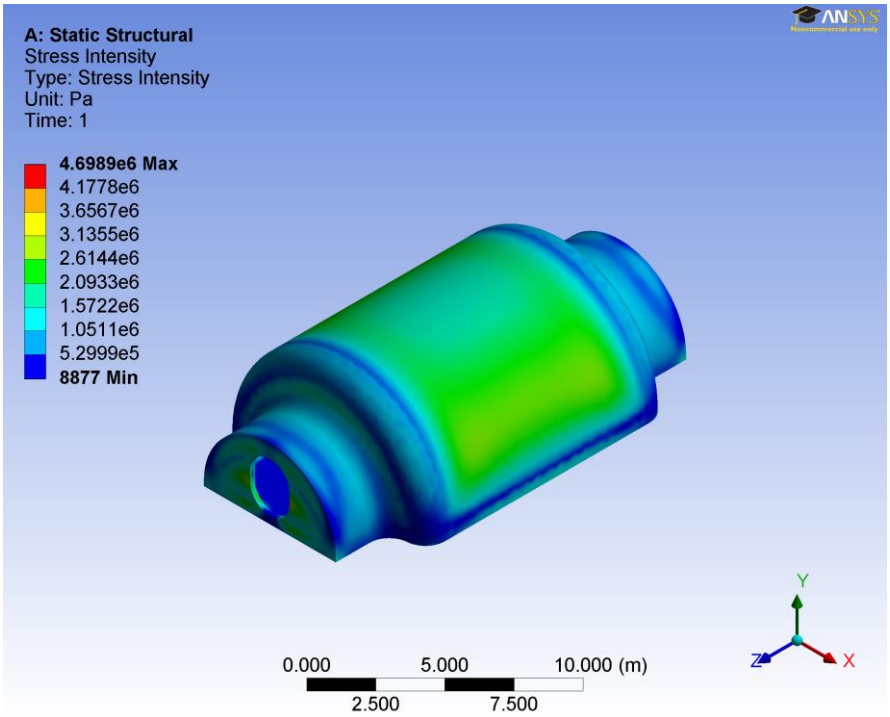

Figure 4.10: Stress intensity.

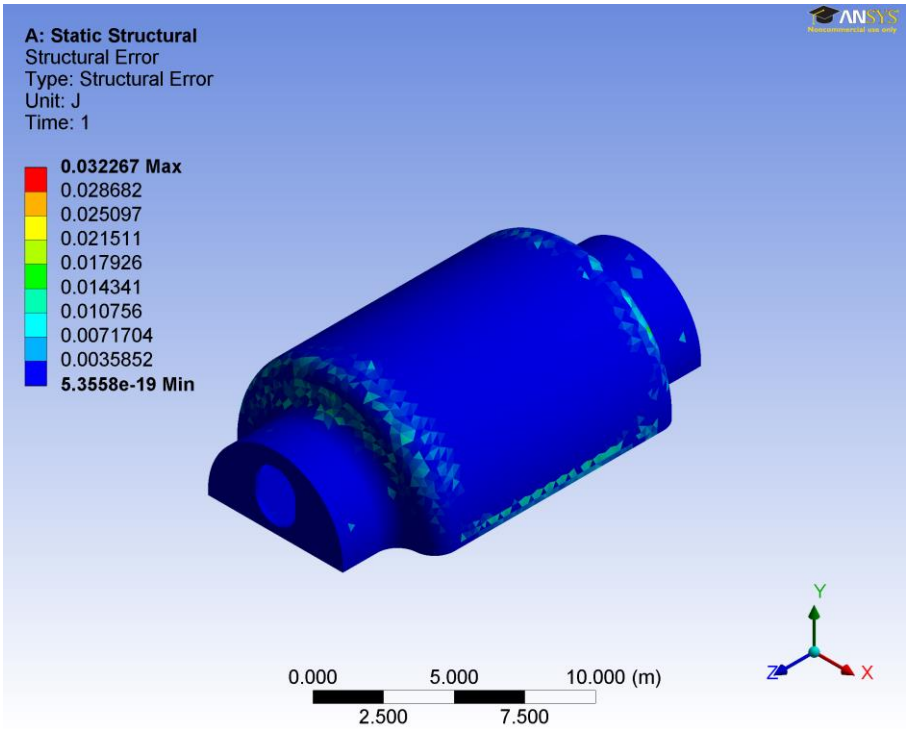

Figure 4.11: Structural error.

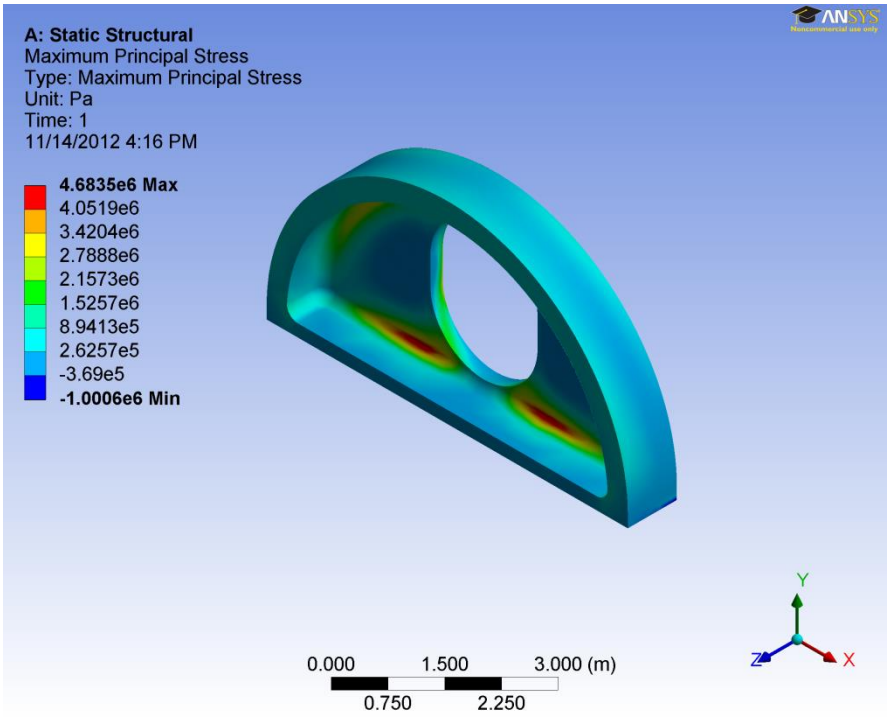

Figure 4.12: Section containing the max principal stress.

Chapter 5. Thermal Control at the Lunar Base

In this chapter we model the thermal lunar environment, explore the thermal properties of regolith and measure the effects of the uncertainties of those properties. We derive an analytical model that can be used to estimate the radiational heat loads of the environment on the structure, so that we can use ANSYS® Academic Research Workbench, Release 13.0 “steady-state thermal” solver for our analysis. Then, numerical simulations are carried out for a selected site at lunar South Pole and used to estimate the capacity requirement of the heat rejecting system based on the thermal loads of the Space Station.

Thermal control at a lunar structure is a challenging problem. The temperature of the lunar surface swings in a large range during the long lunar day and night and differently from location to location. Having essentially no atmosphere on the Moon, the heat exchange between the base and lunar environment are in the form of radiation and conduction. The outer surface of the base exchanges radiative heat with lunar surface, space, and the sun, while the foundation exchanges conductive heat with the Moon. Convective heat transfer takes place inside the base between the air and the walls and also in the air conditioning unit.

Protecting the structure from the radioactive environment and from meteoroid impacts requires a thick regolith shield, but a thicker shield acts as a thermal insulator. It prevents the rejection of heat generated inside by astronauts and instruments. Therefore, heat rejection radiators (HRR), e.g., of the space station type, will be needed to maintain the base temperature in a habitable range.

In order to design the HRR, one needs to know the heat gain/loss of the base and the heat loads, as well as the environment in which the radiators will be placed. Therefore, a thermal analysis of the proposed base is carried out for the lunar South Pole (latitude 88º). The design of the HHR is beyond the scope of this work. The interested reader can refer to Dallas et al. (1971) and Simonsen et al. (1992).

5.1 Temperature on the Lunar Surface

The lunar day lasts approximately 28 Earth days with 14 days of sunlight and 14 days of darkness. At the equatorial latitude temperature ranges from 374˚K during the lunar noon to about 120˚K at lunar night. The temperature variation decreases as the latitudes increase to the Polar Regions, where it varies from about 160˚K to 120˚K (Simonsen et al. 1992). It should be noted that the temperatures mentioned here are the mean temperatures estimated for those latitudes, and they can vary significantly due to the characteristics of the region, e.g., recently, the Diviner Lunar Radiometer Experiment measured subsurface temperatures as low as 38˚K in some polar regions (Paige et al. 2010).

These extreme temperature variations, considering the very low global mean heat flow of the Moon[1], 12 ~ 21 mW/m^2 (3.8215 × 10^{-3} ~ 6.6877 × 10^{-3} Btu/hft^2) (Warren and Rasmussen 1987, Langseth et al. 1976), are essentially due to the solar flux.

Grafton and Nordwall (in Mackay 1963) used some approximate values for the lunar albedo, thermal conductivity, and thickness of the lunar dust layer, and showed that the

[1] The global mean heat flow is the average energy the Moon interior loses to Space.

diurnal temperature on the Moon can be estimated by considering the Moon to be a smooth sphere, and the temperature at equator can be obtained by using the equation

$$T_m(°R) = 673 \sin^{1/6}(\frac{90d}{7}), \quad (5.1)$$

where d is the Earth days past lunar sunrise. Simonsen et al. (1992) extended Equation 5.1 for different latitudes by considering the temperature only as a function of the angle between the sun's rays and the normal outward vector of the lunar surface at a specific location, resulting in

$$T_m(°K) = 373.9(\cos \emptyset)^{0.25}(\sin \theta)^{0.167}, \quad (5.2)$$

where ϕ is the latitude (deg.) of the base position, selected here as 88º for the South Pole. θ is the sun's angle above lunar horizon (deg.).

During the Apollo experiments, a rapid cooling of surface temperature up to 15º phase past sunset[2] was observed (Keihm et al. 1973), after which a temperature drop of only few degrees during the night was measured. We will assume that cooling after the sunset is extremely fast and that the temperature during the night is constant. Therefore, by using the Equation 5.2, the surface temperature for latitude 88˚ is modeled by

$$T_m = \begin{cases} 161.607\ [\sin(11.4786\, d + 9.6495)]^{1/6} & for \quad 0 \le d \le 14 \\ 120 & for\ 14 < d \le 28 \end{cases}, \quad (5.3)$$

where d is the Earth day past lunar sunrise (*also see* Fig. 5.1).

[2] One Earth day and four hours past sunset.

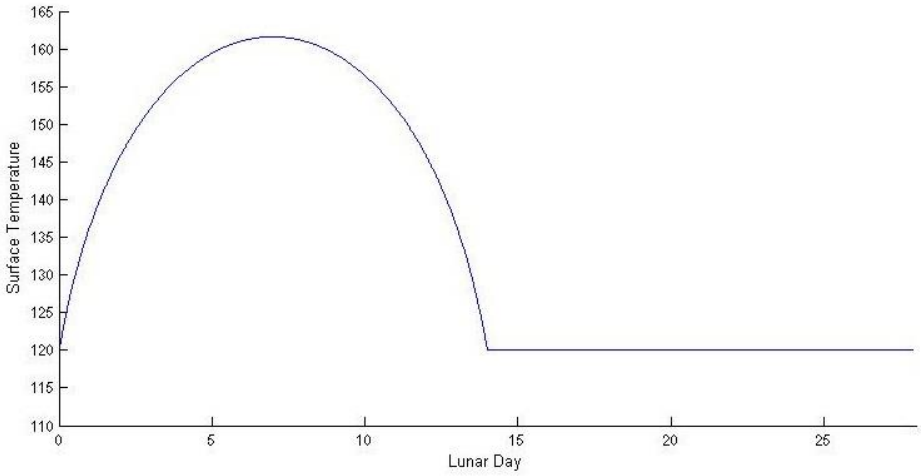

Figure 5.1. Surface temperature (K˚) at 88˚ latitude for one lunation.[3]

5.2 Thermal Properties of Lunar Regolith

Most of our knowledge of the regolith's thermal properties comes from the Apollo era. During the Apollo missions, Heat Flow Experiments were carried out in addition to the experiments on the collected lunar samples.

During the Apollo 15, 16, and 17 missions, heat-flow probes were placed in the holes left after extracting cores from the regolith. Successful measurements were made at the Apollo 15 and 17 landing sites, while Apollo 16 experiments failed due to a broken cable (Heiken et al. 1991). Ever since, many research efforts have been devoted to interpreting these measurements, and to understanding the thermal properties of our Moon, e.g., lunar heat flow and the thermal conductivity of the regolith.

[3]Lunation is defined as the period until the next new moon, or one lunar day and night.

5.2.1 Conductivity

Transfer of thermal energy from the more energetic particles of a substance to the adjacent less energetic ones is called *thermal conduction*. Therefore, *thermal conductivity* is defined as a material property, and represents the rate of heat transfer through a unit thickness of the material per unit area per unit temperature difference. It is a measurement of the ability of a material to conduct heat, as is determined through experiments on material samples.

Keihm et al. (1973) investigated data from the Apollo 15 Hadley Rille landing site, and compared it to surface temperature measurements made during the umbral[4] stage of the August 6, 1971 lunar eclipse. They estimated the theoretical maximum surface temperature to be about 372 ˚K (210 ˚F) at lunar noon and a minimum of about 93 ˚K (-292 ˚F) at lunar morning, with the mean temperature about 207 ˚K (86.8 ˚F). Thermal conductivity of the regolith was estimated to be between 0.9×10^{-5} and 1.6×10^{-5} W/cm ºK (5.2011×10^{-4} and 9.2464×10^{-4} Btu/ft h ºF) for the upper 2 cm (0.79 in), increasing with depth as the density increases, reaching 1.4×10^{-4} W/cm ºK (8.0906×10^{-3} Btu/ft h ºF) at 49 cm (19.3 in). Lunar infrared emissivity[5] of 1.0 and solar absorptivity[6] of 0.93 was used in their calculations.

In another study, Keihm and Langseth (1973) analyzed Apollo 17 data. They found the maximum surface temperature to be about 284˚ K (51.5 ˚F) at lunar noon which cools down to a minimum about 102 ˚K (-276.1 ˚F) at the end of lunar night, with the mean

[4] Umbra is the inner most of a shadow, i.e., the darkest part.
[5] Emissivity indicates the ability of a surface to emit and radiate energy relative to a black body. Emissivity of 1.0 used here implying that the lunar surface is a black body (*see* Section 5.2.3).
[6] If a body is subjected to radiative heat, absorptivity indicates the fraction of the energy the body absorbs in comparison with energy that a black body could have absorbed (*see* Section 5.2.3).

surface temperature about 216 ˚K. They estimated the conductivity at between 0.9×10^{-5} and 1.5×10^{-5} W/cm ºK (5.2011×10^{-4} and 8.6685×10^{-4} Btu/ft h ºF) for the upper thin layer, reaching $1.0 – 1.4 \times 10^{-4}$ W/cm ºK (5.779×10^{-3} and 8.0906×10^{-3} Btu/ft h ºF) at layers deeper than 10 cm (3.94 in).

In both studies the temperatures were found to reach constant values within the first meter of the surface that were higher than the mean surface temperatures. A higher value of equal to 45 ºK at depth of 83 cm at Apollo 15 site and a higher value of equal to 40 ºK at depth of 130 cm at 17 site were measured (Recall the 12 ~ 21 mW/m^2 global mean heat flow of the Moon). Conclusions were made that a strong temperature-dependent conductive layer should be present in the upper few centimeters. In the other words, the lunar surface absorbs more heat during the lunar day than it rejects during the night. This requires the upper few centimeters to have very low density which increases with depth. This causes the upper few centimeters to have a large temperature gradient, which dies down at deeper levels and the temperature reaches a steady-state at some point less than a meter below the surface.

In another effort, Langseth et al. (1976) revisited the Apollo data, and estimated that for all four stations conductivity is in the range of $0.9 – 1.3 \times 10^{-4}$ W/cm ºK ($5.2011 – 7.5127 \times 10^{-3}$ Btu/ft h ºF). They assumed the specific heat to be equal to 0.67 kJ/Kg ºK (0.160063 $Btu/lb_m ºF$) for conductivity calculations. They also estimated densities in range of 1.75 – 1.90 g/cm^3 (109.2 – 118.56 lb/ft^3), and 1.83 – 2.09 g/cm^3 (114.192 – 130.416 lb/ft^3) for Apollo 15 and Apollo 17 landing sites, respectively.

5.2.2 Specific Heat (at Constant Pressure)

The *specific heat*, C_p, is the amount of heat per unit mass required to raise the temperature by one degree Kelvin. Specific heats of the regolith were determined by Hemingway et al. (1973). They examined the samples obtained from Apollo 14, 15, and 16 missions for temperatures ranging from 90 to 350 °K (-297.7 to 170 °F). The results for lunar soil at a density of 1300 kg/m^3 (81.12 lb/ft^3) were obtained and are summarized in Table 5.1 below.

Table 5.1. Specific heat vs. temperature for regolith density of 1300 kg/m^3 (Hemingway et al. 1973).

Temperature	100 °K (-279.7 °F)	150 °K (-189.7 °F)	250 °K (-9.7 °F)	300 °K (80.3 °F)	350 °K (170 °F)
C_p (J/kg °K) (2.389×10^{-4} Btu/lb$_f$ °F)	275.7	433.9	672.4	758.1	848.9
Thermal conductivity (W/m °K) (0.5779 Btu/ft h °F)	0.0007	0.0008	0.0011	0.0014	0.0017

5.2.3 Radiative (Optical) Properties

Radiation may be envisioned as energy being transported either by electromagnetic waves or by photons. The radiative heat transfer from a surface is governed by four material properties: emissivity, absorptivity, reflectivity, and transmissivity (Siegel and Howell 1992).

The *emissivity* of a surface represents the ratio of the radiation emitted by the surface at a given temperature to the radiation emitted by a blackbody at the same temperature. *Absorptivity* is defined as the fraction of the radiation flux incident on a surface that is

absorbed by the surface, while the fraction reflected away is called the *reflectivity*. The fraction transmitted through the body is the *transmissivity* of that body (which is estimated to be equal to zero for the Moon).

5.2.3.1 Lunar Albedo

The albedo is defined as the fraction of light or electromagnetic radiation reflected by a body or particular surface, typically that of a planet (reflectivity). The Moon has an average albedo of 0.09 (very low). The normal albedo value of the lunar near and far sides is summarized in Table 5.2.

Table 5.2. Normal Albedo Values of the Moon (Eckart, 2006).

Region	Minimum	Maximum	Average
Near side			
Mare	0.06	0.09	0.07
Highland	0.11	0.20	0.15
Entire face	0.07	0.10	0.09
Far side	-	-	0.22

5.2.3.2 Emissivity of Regolith

Logan et al. (1972) measured the mid-infrared spectral behavior of Apollo 14 and 15 regolith and compared them to ground-based and balloon-borne measurements. They estimated the infrared emissivity to be in the range of 0.90-0.95, confirming the fact that the Moon does not emit as a black body.

5.3 Modeling Considerations for the Base Structure

In order to calculate the thermal status of the base, we start by assuming that the inside temperature of the base is controlled and constant. Therefore, the concern is to model the heat exchanged between the exterior and lunar environment. In the following, we will utilize our understanding from the Apollo data, and other discussions presented so far, to have a good estimation of the thermal environment to which the base will be exposed. In other words, boundary conditions will be modeled and simplified so that they can be used for numerical calculations.

5.3.1 Foundation of the Structure

As mentioned earlier, heat exchange at the foundation is governed by conduction. From the Apollo heat flow experiments, a constant subsurface temperature is expected. A natural guess is that the regolith in vicinity of the base will be altered due to construction and later on by the astronauts' activities. This will densify the top layer of the surface, resulting in less difference between mean surface temperature and steady subsurface temperature. Also, the polar regions experience milder exposures to the solar flux. Therefore, a conclusion can be made that the temperature at some depth should be considered the same as, or a value fairly close to, the mean surface temperature.

On the other hand, the subsurface temperature in the vicinity of the base would be affected by the heat conducted through the foundation. Therefore, it is safe to assume that at some depth under the base, the temperature is constant, i.e., heat flux at that depth would be the same as lunar global mean heat flow.

5.3.2 Outside Surface of the Structure

Assuming uniform lunar temperatures in the vicinity of the base, the general heat transfer equation governing the thermal exchanges between a thermal shield and its environs at the lunar surface is (Mackay 1963):

$$\frac{q}{A} = (1 - F_{bm})\epsilon_b \sigma T_b^4 + F_{bm}\epsilon_m \sigma (T_b^4 - T_m^4) - S_c \alpha_s \cos\theta_s \ , \qquad (5.4)$$

where q is the heat flux passing through area A, F_{bm} is the configuration factor, ϵ_b and ϵ_m are the non-dimensional emissivity factors, σ is the Stefan-Boltzmann constant, T_b is the temperature of the outside surface of the shield, T_m is the lunar surface temperature, S_c is the solar constant (heat from the sun), α_s is the absorptivity of the outside surface of the shield, and finally θ_s is the angle between incident solar rays and the normal to the outside surface of the shield.

The incident solar radiation reflected from the lunar surface and hitting the structure is neglected due to very low lunar albedo. Also, it is assumed that the heat radiated from the structure that hits the lunar surface is not reflected back to the structure (due to the same reason). The first term on the right hand side of Equation 5.4 is the heat per unit area that radiates from the structure into space. The second term represents the heat per unit area exchanged between the structure and the lunar surface. The third term is the heat per unit area absorbed by the structure from the Sun. Assuming the lunar surface to be rough enough (very close to black body) so that it does not allow the heat radiated from the structure to be reflected back to it, ϵ_b and ϵ_m will be the same. Therefore, Equation 5.4 will be simplified to

$$\frac{q}{A} = \epsilon_b \sigma T_b^4 - F_{bm}\epsilon_b \sigma T_m^4 - S_c \alpha_s \cos\theta_s \ . \quad (5.5)$$

In Equations 5.4 and 5.5, the coefficient F_{bm} only depends on the shape of the structure and its surrounding environment and it represents the fraction of heat radiating from the structure that impact the lunar surface. In other words 1– F_{bm} is the percentage of the heat radiating from the base that escapes into space.

5.3.2.1 Configuration (view) Factor

One of the complexities in the calculation of radiative heat transfer between surfaces is the determination of how the surfaces view each other. Therefore, it is customary to use a quantity called the *configuration factor* to account for the geometry.

Generally, a configuration factor is obtained by considering differential area elements on the surfaces involved and then integrating over the domains of the surfaces. The radiative heat transfer from a diffused differential element to another element is modeled in Figure 5.2. The fraction of energy leaving surface element dA_1 that arrives at element dA_2 is defined as the geometric configuration factor $dF_{1\text{-}2}$, or dF_{12}. It can be shown that F_{12} only depends on position vector, $\boldsymbol{S}$, and the angles between $\boldsymbol{S}$ and the normal surface vectors of the differential area elements dA_1 and dA_2, θ_1 and θ_2, respectively (Siegel and Howell 1992). The relation is

$$dF_{12} = \frac{\cos\theta_1 \cos\theta_2}{\pi |\boldsymbol{S}|^2} dA_2 \quad (5.6)$$

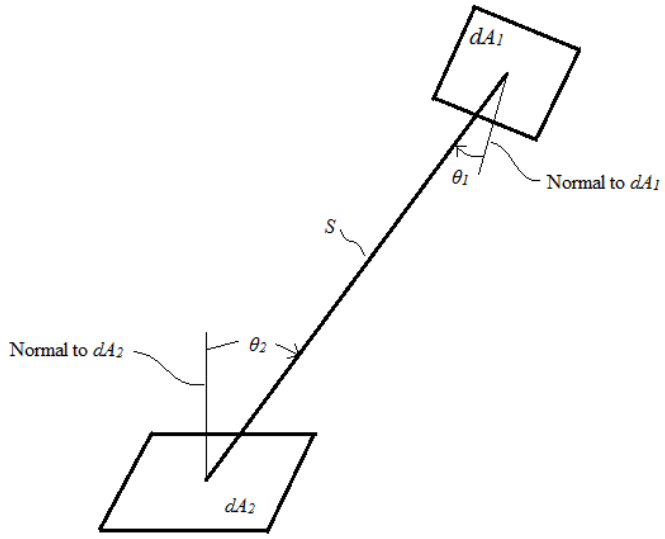

Figure 5.2. Radiative interchange between two diffuse differential area elements (adapted from Siegel and Howell 1992).

The inverse differential configuration factor can be obtained by using the following *reciprocity rule*,

$$dF_{12}dA_1 = dF_{21}dA_2 = \frac{\cos\theta_1 \cos\theta_2}{\pi|\boldsymbol{S}|^2}\, dA_1 dA_2 \,. \tag{5.7}$$

For two finite areas the reciprocity rule will be

$$F_{12}A_1 = F_{21}A_2 \,. \tag{5.8}$$

Therefore, the configuration factor is obtained by considering two differential elements on the two bodies and integrating Equation 5.7 over the domain of the areas involved, and takes the form

$$F_{12} = \frac{1}{A_1}\int\int \frac{\cos\theta_1 \cos\theta_2}{\pi|\boldsymbol{S}|^2} dA_1 dA_2 \,. \tag{5.9}$$

Generally, numerical evaluation of Equation 5.9 requires great effort, and is computationally expensive even for very simple geometries. Thus, there exist shortcuts that take advantage of the definition of configuration factor as the fraction of energy received by the surface, and that utilize the reciprocity relation and conservation of energy to estimate this factor. Therefore, one can use the known configuration factors for simple shapes as good approximations for more complicated configurations. Interested readers can refer to Siegel and Howell (1992) and Sparrow and Cess (1978). Also, many computer programs have been written for numerical calculation of configuration factors, although they can be computationally very expensive.

5.4 Numerical Modeling

In order to estimate the effectiveness of shielding (thermal gain or loss), it is assumed that the inside air temperature is controlled at a constant uniform temperature of 23 °C (296.15 °K, 73.4 °F) with the film[7] coefficient of 10 W/m^2 ^oK (1.7622 Btu/h ft^2 ^oF). Therefore, the boundary conditions to which the regolith shield and sintered regolith foundation is exposed need to be modeled.

5.4.1 Lunar Surface

The slow variation of lunar temperature (see Fig. 5.1) allows the thermal behavior of the base to be very close to steady state. Also, in order to design the thermal control system the extreme conditions are needed to be evaluated. Therefore, we investigated the thermal behavior of the base for two steady state conditions, lunar night and lunar noon. The

[7] Film coefficient is also called convection coefficient. It is called film coefficient since ANSYS uses this terminology.

surface temperatures for these cases are 120 °K and 161.61 °K (-243.7 °F and -168.8 °F), respectively. Recall that these temperatures were estimated for the base position selected to be at 88º latitude at South Polar Regions.

As was mentioned earlier, the temperature at some depth can be considered to have a constant value. Therefore, the heat flux at depth of 3 m (9.84 ft) is considered to be uniform and equal to the lunar heat flow and is selected as 16 mW/m^2 (5.0954×10^{-3} $Btu/h\ ft^2$) based on our discussion in Sec. 5.3.1.

Also for numerical simulation, a finite section of the lunar surface is needed. Therefore, we assume that the lunar surface at 13.5 m (44.3 ft) away from the magnesium base (10.5 m away from the shield) is in thermal equilibrium with surfaces in its vicinity, i.e., no heat flux through the cut-section (Fig. 5.3). The distances in the Figure 5.3 is selected with a little difference, just to give us a sense if these are selected large enough by comparing the thermal flux at 10.5 meters away from the shield. The surface is modeled as isotropic with a thermal conductivity of 0.009 W/m ºK (5.2011×10^{-3} Btu/ft h ºF) (*see* Sec. 5.2.1), and radiative properties of 0.93 are assumed for both absorptivity and emissivity (*see* Sec. 5.2.3).

5.4.2 Foundation

The base is on a foundation of thickness 0.5 *m* of sintered regolith. Although some experiments have been carried out on the sintering of regolith (*see* Sec. 3.4.1), no value is reported for its thermal conductivity. Therefore, two values for the conductivity of sintered regolith are considered, 0.009 and 1.5 W/m °K (5.2011×10^{-3} and 0.8669 Btu/ft^2 h °F). The first one is the same value as that for the lunar surface, and second one is a value

in the range of conductivity coefficients for cast basalt ceramic, where an assumption is made that the thermal conductivity of the sintered regolith should be close to that of the cast basalt ceramic, which ranges from 1.1 to 1.6 W/m °K (0.6357 and 0.9246 Btu/ft^2 h °F) (ITW Densit, Data Sheet).

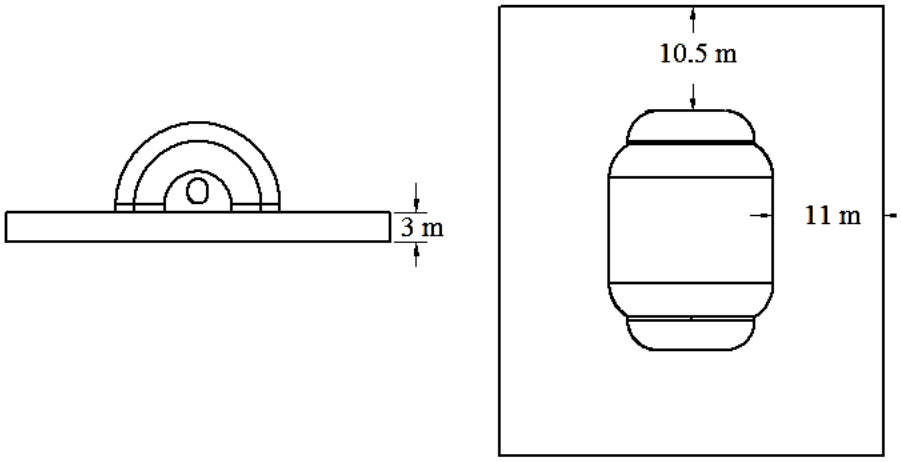

Figure 5.3. Cut-section of lunar surface used for numerical simulations. In left figure the distances of the base to the edges are 11 m.

5.4.3 Sandbags of Regolith Shielding

The thermal properties and density of the sandbags used to contain the regolith shielding will be determined based on the material of the bags and the method of filling them. Here, we assumed that they have the same conductivity as the lunar soil. Moreover, we consider perfect contact (no gaps) between the bags and the magnesium structure. Also, the emissivity and absorptivity of the shield is considered to be the same as that of the

lunar surface, 0.93, since, with time the shield would be covered by dust due to dust migration. Therefore, it is probable that its radiative properties, regardless of the material used for the bags, will be very close to those of the lunar surface.

5.4.4 Radiative Boundary Conditions

Configuration factor, as mentioned earlier, is a crucial consideration in modeling the radiative surfaces. Therefore, we start by estimating this property, and later will use it to define the radiative boundaries in such a way that can be used in the ANSYS steady-state thermal solver.

5.4.4.1 Configuration factor

In order to follow the same assumption we made regarding the surface temperature, we consider that the base rests on an infinitely large smooth surface, i.e., there is no crater or hill close to the base. Avoiding the cumbersome integration of Equation 5.9, we start by considering two cases for which the configuration factors are known. The factor between a vertical surface and an infinitely large horizontal plane, shown in Fig. 5.4a, and the factor between a cylinder and a plate parallel to the axis of the cylinder, shown in Fig. 4b, are considered next.

Mackay (1963) showed that for the case of Figure 5.4a, the configuration factor is 0.5. For the case of Figure 5.4b the configuration factor can be obtained by using the graph represented in Figure 5.5 (Sparrow and Cess 1978).

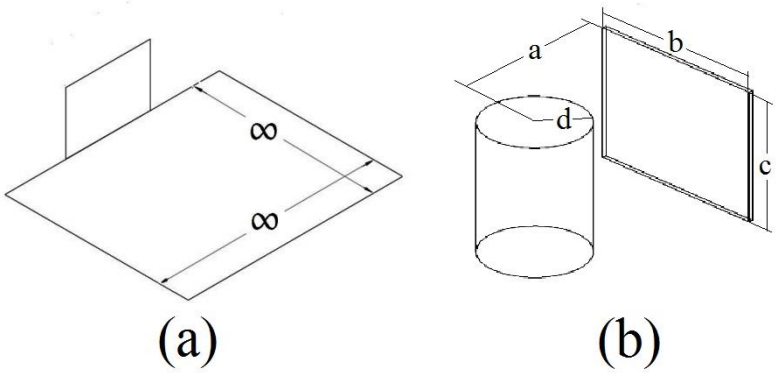

Figure 5.4. (a) A vertical surface and an infinitely large horizontal plane. (b) A cylinder and a plate parallel to the symmetrical axes of the cylinder (adapted from Sparrow and Cess 1978).

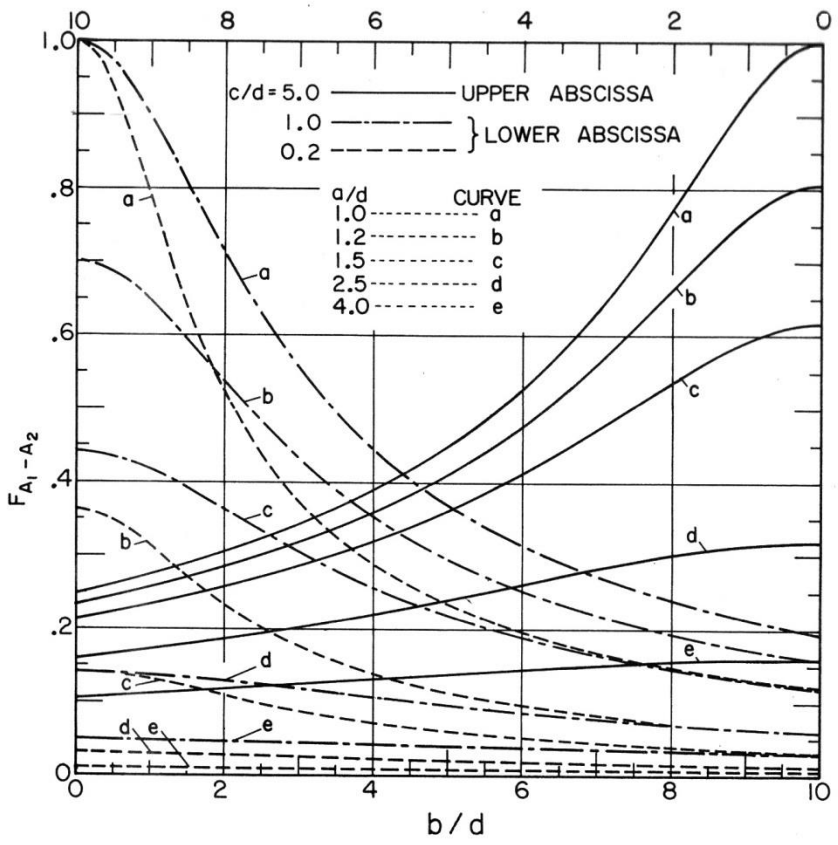

Figure 5.5. Configuration factors for system of Figure 5.4.b (Sparrow and Cess 1978, with permission of CRC Press).

We assume that the lunar structure consists of one large semi-cylinder that is connected at both ends to smaller semi-cylinders. In order to have an estimation of the view factor, imagine each of these semi-cylinders are embedded in a box with faces tangential with respect to the cylinders (see Fig. 5.6). Using Figure 5.4b with the plate's width equal to the diameter of the cylinder, and of equal length, setting $a=r$, we obtain the configuration factor of the plate to cylinder and by using reciprocity law the inverse factor. Then, we can use the Figure 5.4a, to estimate the radiative energy heating the ground. We assume the following:

- A small portion of the radiative heat leaving any surface of the larger cylinder is received by the smaller ones, and can be neglected.
- Radiative energy leaving the smaller cylinders cannot pass through the vertical surface of imaginary box facing the larger semi-cylinder.
- 50% of the energy passing through the vertical surfaces facing the lunar surface escape to empty space (Fig. 5.4a).

Considering these assumptions, and the definition of configuration factor as the fraction of energy leaving the base and received by lunar surface, the factor for the larger semi-cylinder to lunar surface is approximated to be about 0.365, and about 0.356 for the smaller sections. Therefore in numerical calculations we select 0.36 for all semi-cylinders. This factor for vertical surfaces is 0.5 (Figure 5.4a).

The factors obtained are for the cases where the surface temperature in the vicinity of the base is uniform. To estimate this factor for the surfaces facing the shadow during noon, some of the radiative heat is received by the shadow area, some by the area exposed to

the sunlight, and the rest would escape to space. So, we need another known configuration to account for this case. We used the configuration factor of rectangles having a common edge and forming an arbitrary angle, where one rectangle is semi-infinite long (Howell 2012). The configuration is shown in Figure 7, and the factors associated with $\Phi = 90^{o}$ are presented in Table 5.3.

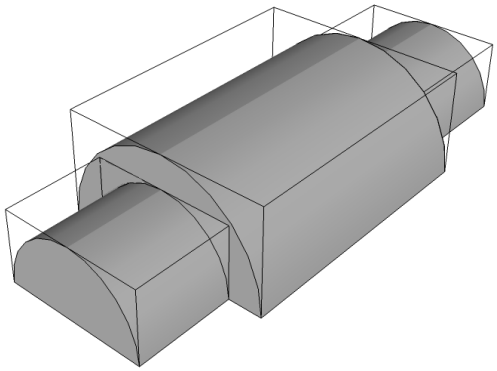

Figure 5.6. Simplified configuration of the base and imaginary boxes containing the base.

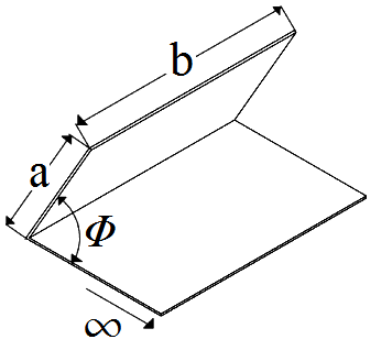

Figure 5.7. Rectangles having a common edge and forming an arbitrary angle, where one rectangle is semi-infinitely long (adapted from Howell 2012).

Table 5.3: Configuration factors associated with $\Phi = 90^{\circ}$ of Figure 5.6 [(a)] (adapted from Howell 2012).

a×b/Φ	0.02	0.05	0.10	0.20	0.40	0.60
Φ = 90º	0.482773	0.464222	0.439467	0.400918	0.345351	0.305299
a×b/Φ	1.00	2.00	4.00	6.00	10.00	20.00
Φ = 90º	0.250000	0.176107	0.115047	0.087378	0.060533	0.035778

[a] For the configuration factors associated with different Φ please refer to the reference. These values are not presented here since we did not need them for our calculations.

Using these values for the surfaces facing the shadow, F_{bm} for the shadowed area is 0.2448, and for the lighted area is 0.1152. F_{bm} for the vertical surfaces facing the shadow is found to be 0.34 for the shadowed area and 0.16 for the lighted area.

5.4.4.2 Ambient Temperature (T_a)

Heat exchange through radiation between the base and the lunar environment can be modeled using Equation 5.5, and can be written in the form,

$$\frac{q}{A} = \epsilon_b \sigma (T_b^4 - F_{bm} T_m^4 - \frac{\alpha_s}{\epsilon_b \sigma} S_c \cos\theta_s) \,. \tag{5.10}$$

Also, for surface radiation problems, Stefan-Boltzmann law states that

$$\frac{q}{A} = \epsilon_b \sigma (T_b^4 - T_a^4) \,. \tag{5.11}$$

Therefore, the ambient temperature is

$$T_a = (F_{bm} T_m^4 + \frac{\alpha_s}{\epsilon_b \sigma} S_c \cos\theta_s)^{1/4} \,. \tag{5.12}$$

The ambient temperature can be obtained by Equation 5.12 for a surface and be input into ANSYS steady-state thermal solver. As is obvious from Equation 5.12, during the lunar

day the ambient temperature is affected by the relative position of the sun to the surface by the value of θ_S. Therefore, the orientation of the base on the lunar surface is of importance. As we are interested in the extreme case, the lunar base orientation should be east to west, i.e., one entrance facing the east while the other one looking at west. This configuration allows the base to receive maximum heat from the sun, at lunar noon.

For simplicity, we replaced the term $S_c \cos \theta_S$ by the equivalent mean solar flux on the surfaces exposed to the sun. This was done by finding the trajectory of the surface in the plane perpendicular to the solar flux at noon (about 190 m^2), and by considering the solar flux to be 1370 W/m^2 (Eckart 2006) with the absorptivity of 0.93, the total solar heat was calculated and divided by the actual surface area facing the sun (about 337.2 m^2).

Regarding the lunar noon, for the surfaces of the shield facing the shadowed area, it is assumed that the temperature of the shadow area is uniform and equal to 120 °K. As was discussed earlier, a rapid cooling was observed during the Apollo experiments (Sec. 5.1). Therefore, we assumed that most of the shadowed area is at the nighttime temperature, using the earlier assumption that the Moon's surface is smooth.

Therefore, based on the discussion and values above, the ambient temperatures are calculated and are shown in Figure 5.8. Other boundary conditions are summarized in this figure as well.

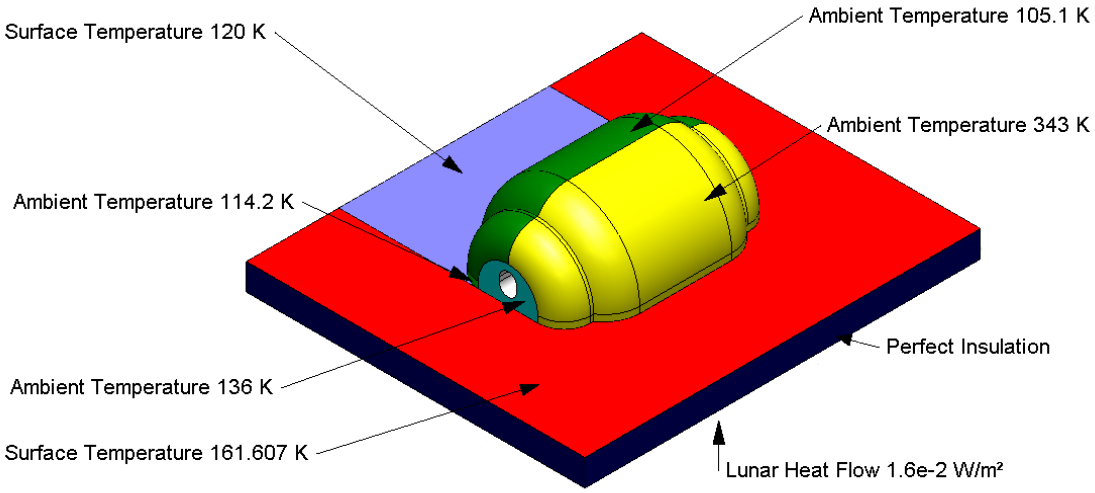

(a)

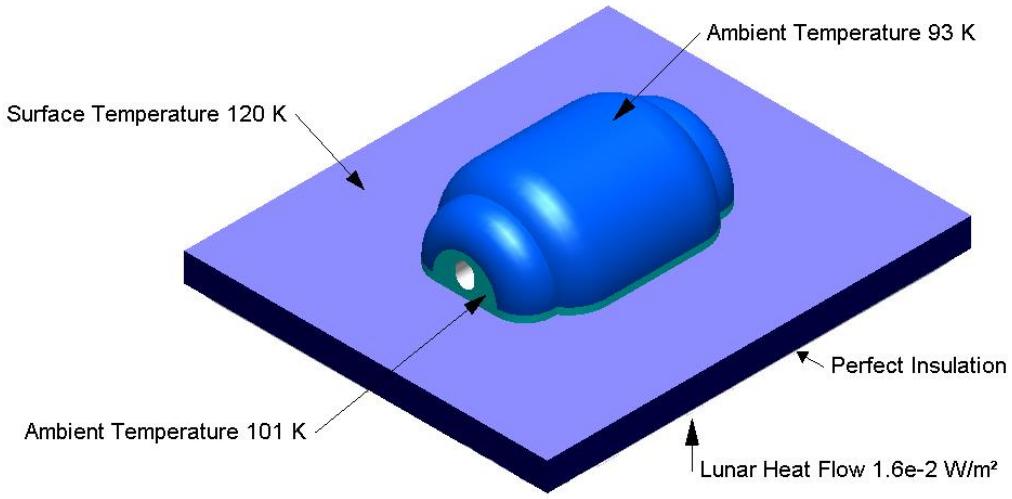

(b)

Figure 5.8. Boundary conditions for (a) lunar noon, (b) lunar night.

5.5 Numerical Results

ANSYS® Academic Research Workbench, Release 13.0 software is used for numerical simulations. Regarding the heat gain/loss of the base, all the cases studied exhibit heat loss.

Considering the case with foundation conductivity of 0.009 W/m ºK (Case 1), the rate of heat loss is estimated to be 142 W at the lunar noon and 331 W at night. For the case with foundation conductivity of 1.5 W/m ºK (Case 2), heat loss is found to be about 145 W at noon and 336 W at night. The temperature distributions are shown in Fig. 5.9 and Fig. 5.10, for case 1 and 2, respectively, while the heat fluxes for cases 1 and 2 are presented in Figures 5.11 and 5.12.

Considering Figures 5.11 and 5.12, there are regions where the heat flux is larger, and can be seen in those figures by yellow and red arrows. These are due to inadequacies in the generated mesh. It can be better observed by calculating the thermal error. As an example, the thermal error for the case 1, for lunar noon, is presented in Figure 5.13, and discussed next.

The continuity assumption results in a continuous temperature field from element to element, but a discontinuous thermal flux field. In order to obtain more acceptable fluxes, thermal flux is calculated using the averaged nodal thermal fluxes for each element, from which the thermal flux is subtracted for each node. This value is then used to calculate the energy error for each element (ANSYS 14.0 Help[a]). These calculations are presented in more detail in Appendix 1, Sec. A1.1. Therefore, the “Thermal Error” can be used to

indicate the mesh adequacy. Obviously, a finer mesh will result in a smaller thermal error.

The errors observed in our calculations occurred at locations where there are discontinuities, as expected. We were unable to refine the mesh to obtain less error due to software and hardware limitations. It is clear from Figure 5.13 and the figures presented in Appendix 2, the error happened in very few minor elements and their contributions to the final results can be neglected. Moreover, considering the accuracy of the data for lunar environment and material properties, we are confident that the results presented are in an acceptable range.

5.6 Discussion and Conclusions

Now that we have estimated the heat loss at a lunar base, a rough calculation of other heat loads that need to be rejected are worth noting. The heat loads (per unit volume) for different modules, e.g., habitat, laboratory, etc., are selected to be the same as for the space station (Simonsen et al. 1992), and are summarized in Table 5.4.

Using the values presented in Table 5.4, and the values obtained for the lunar base at noon and night, we can obtain the minimum and maximum heat that needs to be rejected by thermal control systems, e.g. HRR. These values are summarized in Table 5.5.

Table 5.4. Selected heat loads in habitable areas.

Module	**(W/m^3) 23 ˚C**
Habitation	70.91
Laboratory	70.91
Node	104.79
Airlock	377.05

Table 5.5. Minimum and maximum heat load that needs to be rejected by HRR.

Module	Minimum (kW)	Maximum (kW)
Habitation/Laboratory, Case 1	50.114	50.303
Habitation/Laboratory, Case 2	50.109	50.300

Considering these values and the discussion presented in this chapter, the following are some notes and conclusions worth mentioning:

1. Although the conductivity coefficient for sintered regolith is not known, the heat loss of the structure did not vary significantly for different values for this property.
2. The heat load that needs to be rejected, for both case 1 and case 2, showed small variations for the lunar noon and lunar night time, that is, the base can be assumed to be perfectly insulated for the HRR design process.
3. We have discussed the regolith's conductivity coefficient estimated from Apollo Heat Flow Experiments in Section 5.2.1, which differs to a great extent from the values obtained by experiments on lunar soil samples presented in Table 5.1. The Apollo conclusions were made (Table 5.1) for the upper few centimeters of regolith, after which in deeper layers the conductivity reaches the values in the range of $0.9 – 1.3 \times 10^{-4}$ W/cm ºK. Still there exist debates on how accurate were the Apollo measurements. Possible sources of inaccuracy include:
   a) Uncertainties in the surface emissivity value selected in conductivity calculations (Keihm et al., 1973).

b) Lunar soil in vicinity of the instruments was disturbed due to drilling and astronaut activity. Keihm et al. (1973) considered this factor to be negligible because of the agreements between astronomical observation and results. While later Langseth et al. (1976) suggest that the transient effects due to these activities were present during the measurements and proposed a 5-7 year period to reach the steady-state regime.

c) Daytime measurement error due to cable orientations (Keihm and Langseth, 1973).

While these uncertainties will affect the heat loss of the base, they will not change the results dramatically. The base can still be considered to be perfectly insulated (by comparing the heat loss and heat load).

4. The calculations here were carried out for the average solar flux, and in the final design of an actual structure solar storms need to be taken into account.
5. We did not consider the effects that nearby structures can have on the base heat loss. Also, the lunar surface was assumed to be smooth. In a final design these effects need to be considered as they can have a large impact on the configuration factor.
6. We assumed there to be no gaps between the structure and the sandbags, even though they will be present. Therefore, a lesser heat loss should be expected.

All in all, our understanding of the lunar environment is sufficient for modeling the thermal environment to which the base will be exposed. Also, by considering an appropriate factor of safety when designing the HRR, the uncertainties can be overcome.

More importantly, the 3 meter regolith thickness seems to be sufficient to stabilize the thermal variation of the lunar day and night.

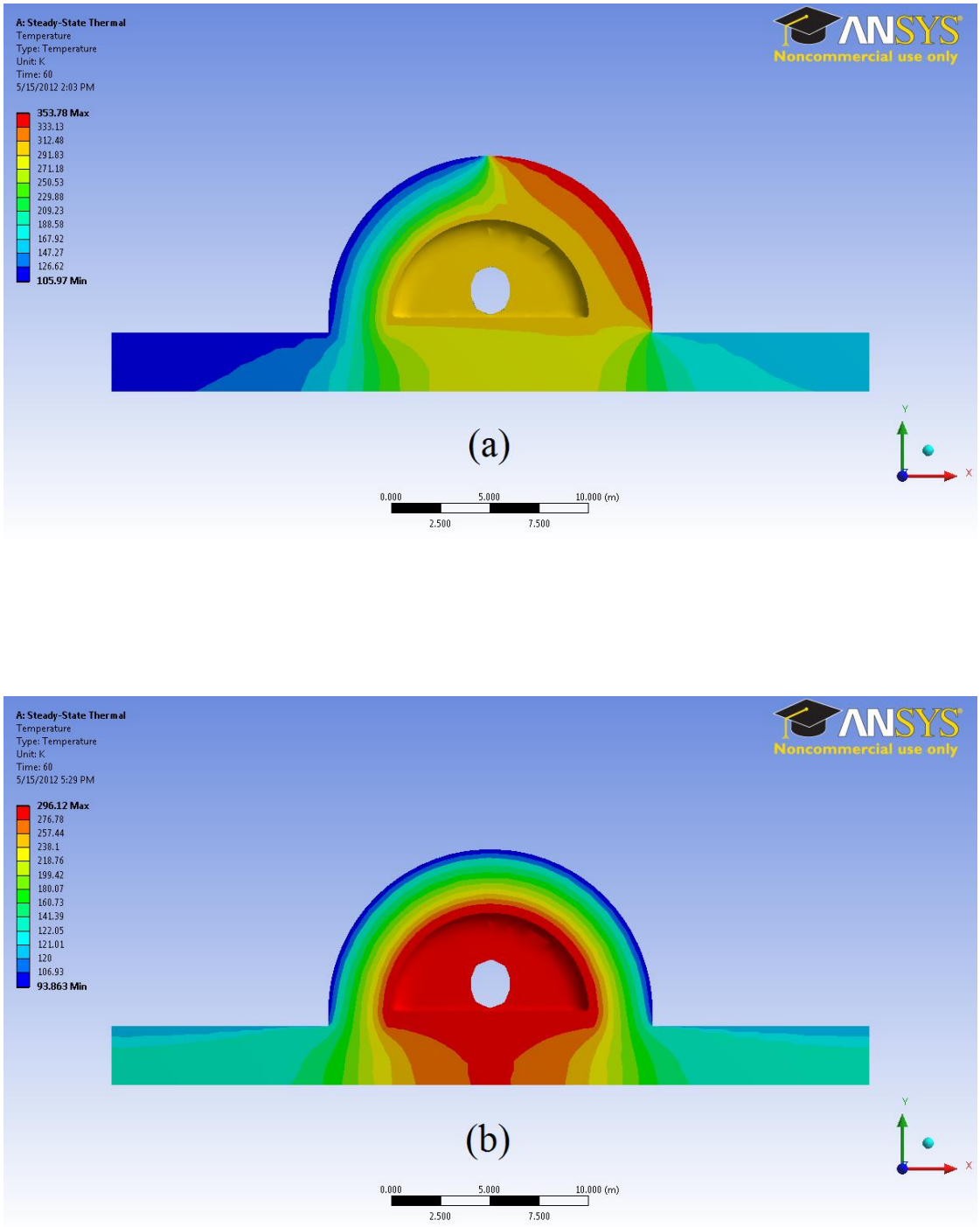

Figure 5.9. Case 1, temperature distribution at (a) lunar noon and (b) lunar night.

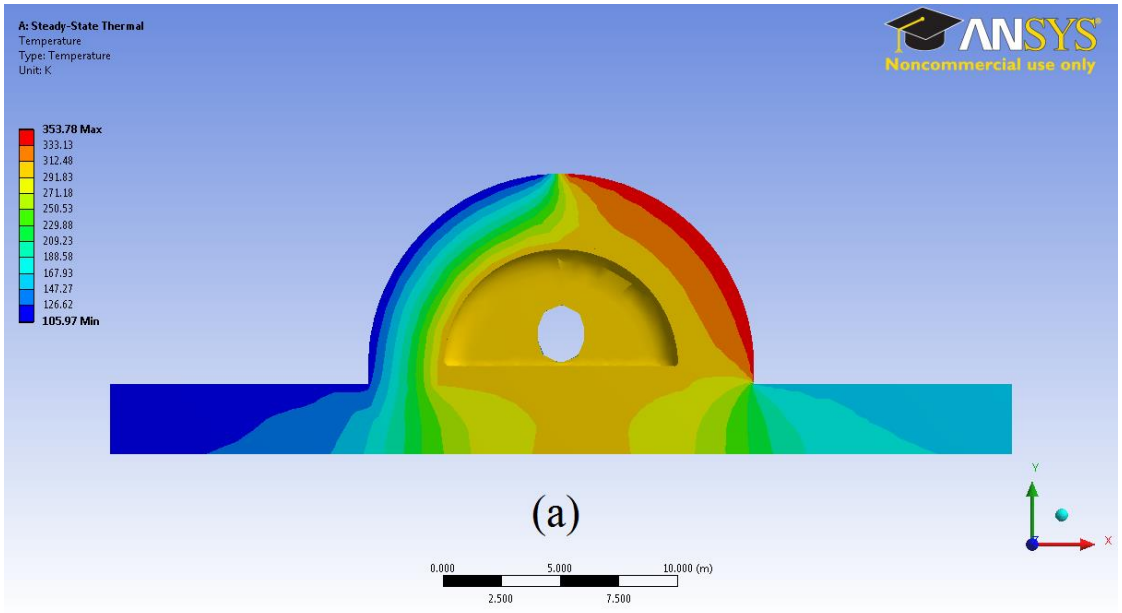

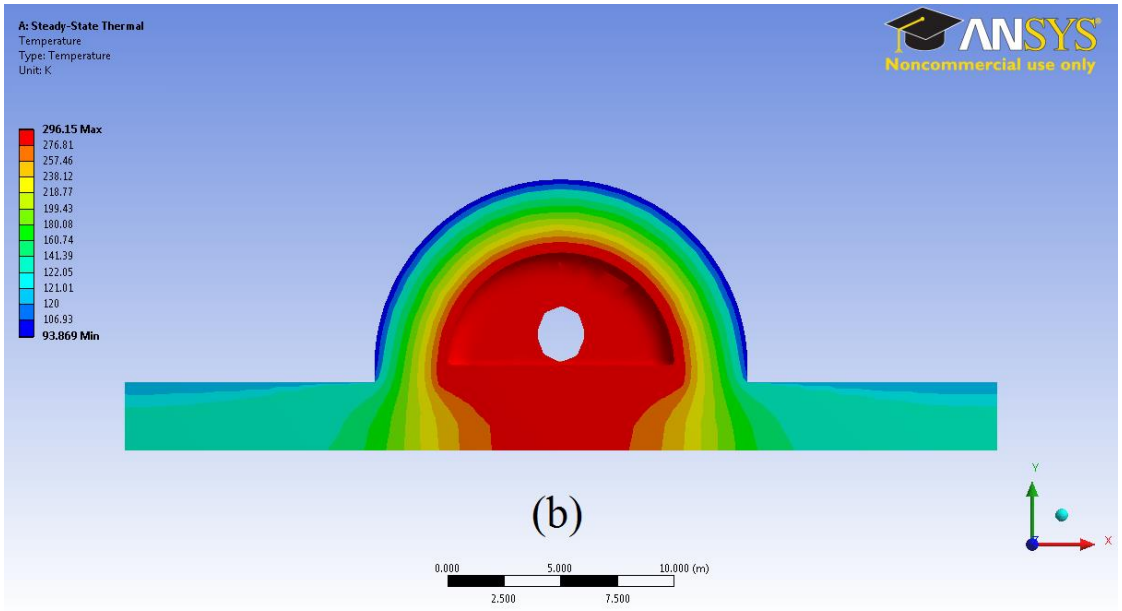

Figure 5.10. Case 2, temperature distribution at (a) lunar noon and (b) lunar night.

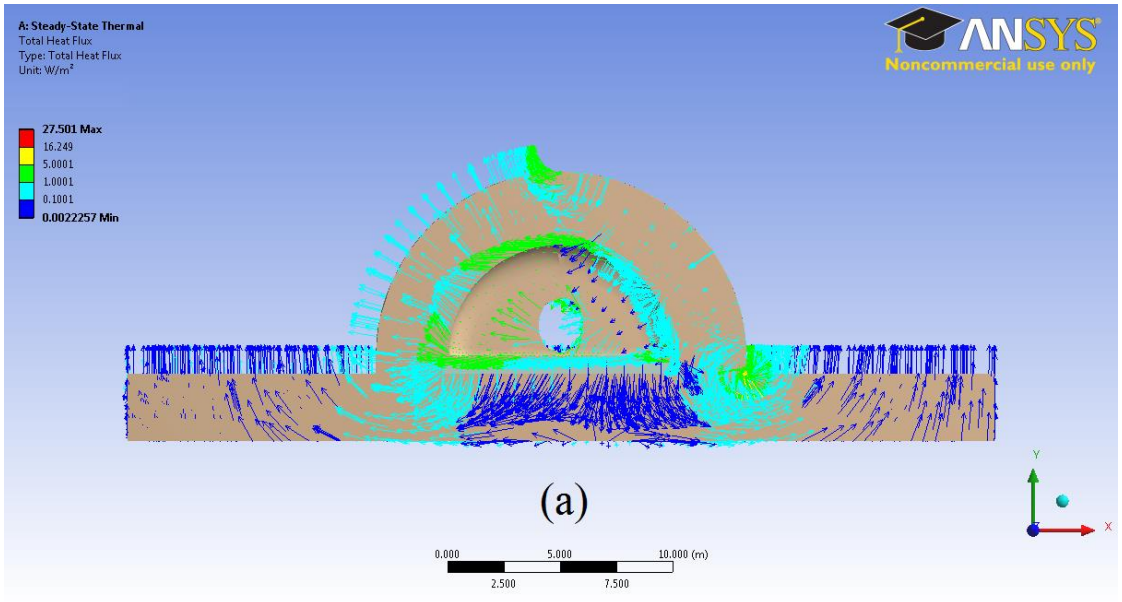

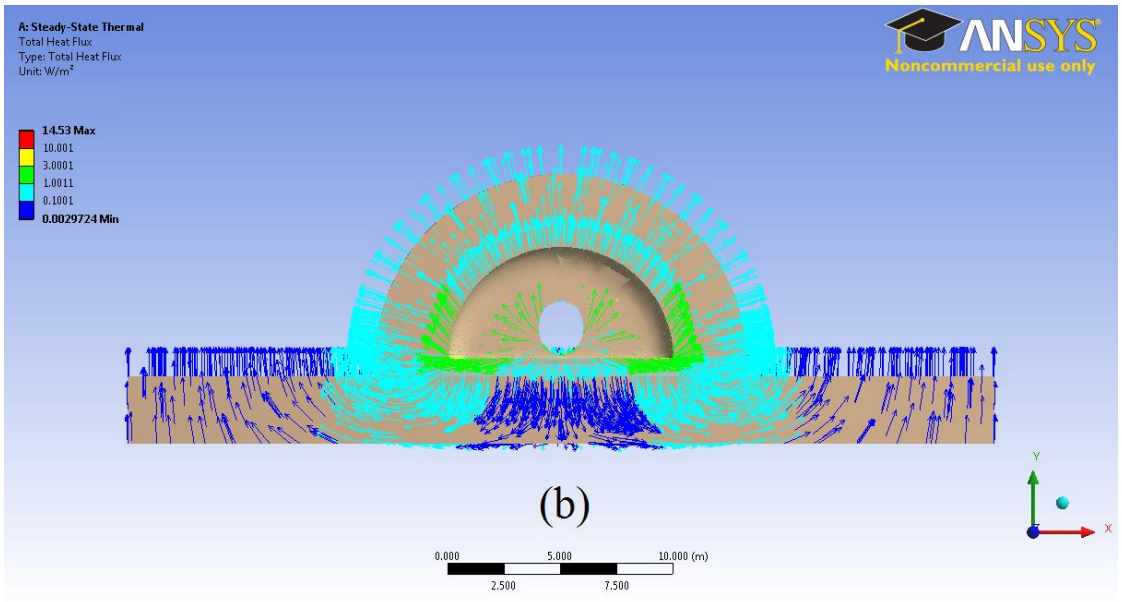

Figure 5.11. Case 1, heat flux at (a) lunar noon and (b) lunar night.

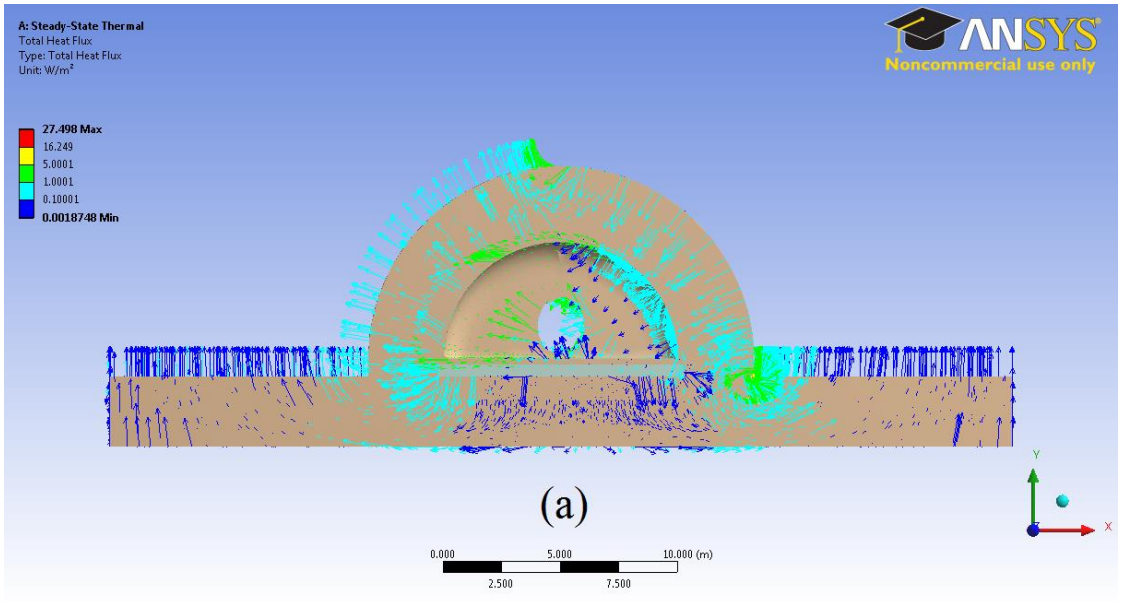

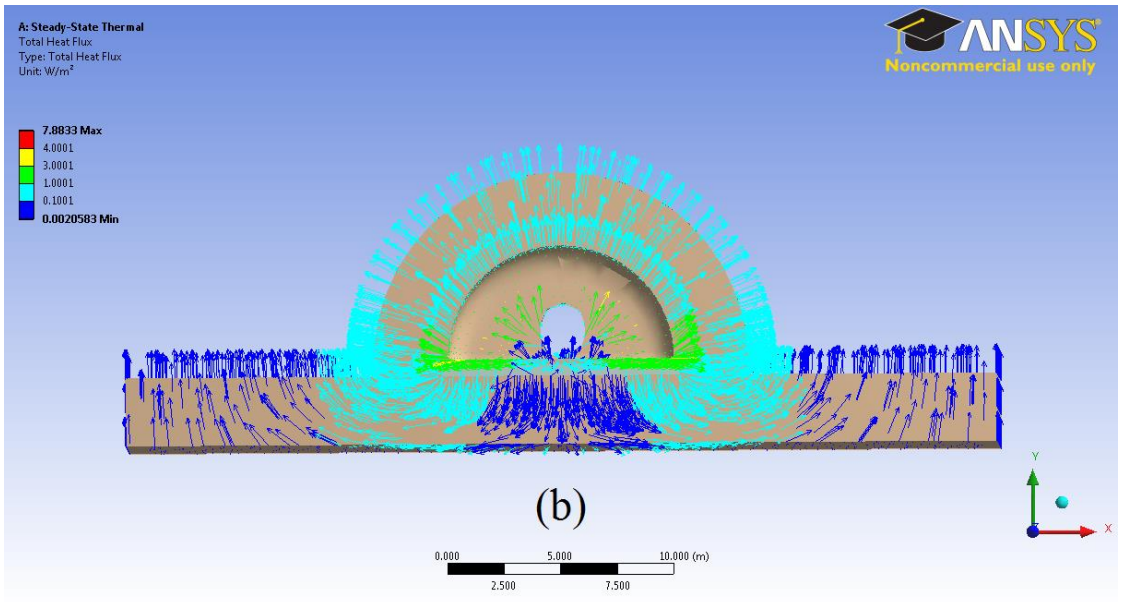

Figure 5.12. Case 2, heat flux at (a) lunar noon and (b) lunar night.

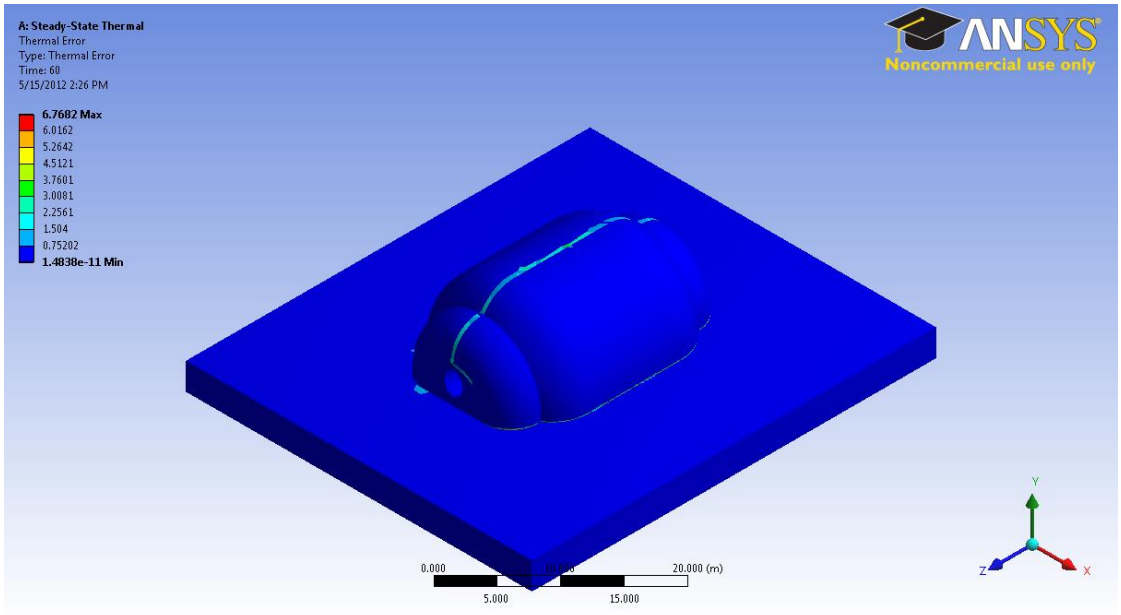

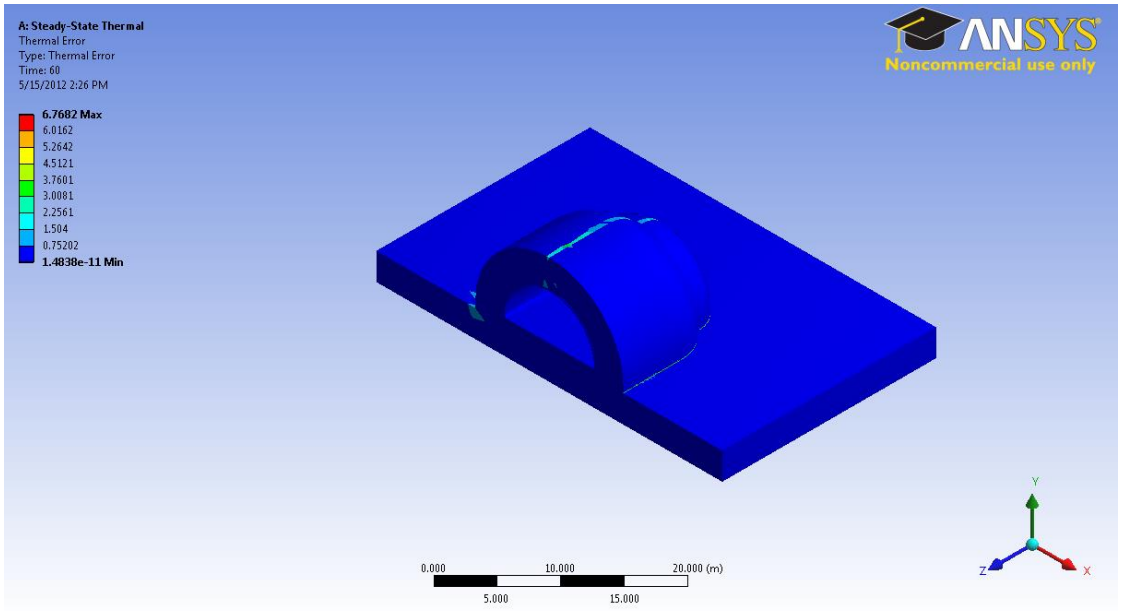

Figure 5.13. Thermal error for case 1 at lunar noon, full configuration and cross-section view.

Chapter 6. Seismic Analysis

Despite the available literature on lunar seismicity, seismic risk has not been studied for a lunar surface structure. We begin by exploring the literature on moonquakes. Then, we develop a seismic model based on best available data and apply it to our typical structure. Two different solvers of ANSYS® Academic Research Workbench, release 14.0 software, random vibration and mode-superposition transient dynamic, are used to obtain the seismic structural response and the results are compared. The chapter ends with a discussion on the vulnerability of lunar structural designs that ignore seismicity.

Before we begin reviewing the literature, we first need to define the ground supports of our typical structure. Having modified the structure, some definitions are presented for readers who are not familiar with the jargon used in seismology and seismic engineering. Afterwards, we summarize the theories based on which the solutions are obtained (Section 6.3).

6.1 Lunar Structure

In Chapters Two and Three, we proposed our conceptual lunar base as a magnesium structure, covered with regolith sandbagged shielding on a sintered regolith foundation. Also, we saw that cast regolith possesses an ultimate strength that is an order of magnitude higher than lunar concrete. We assume the foundation to be built out of lunar concrete since the properties of sintered regolith could not be found. This is conservative, because higher mechanical properties are expected from sintered regolith compared to those of lunar concrete.

Although the technologies for sintering regolith have not matured yet, they are promising. When these technologies advance, the sintered regolith could have properties, if not comparable to cast regolith, better than lunar concrete.

We have added six supporting columns to the magnesium structure, as depicted in Fig. 6.1, of the lunar structure of Chapter Five. The engineering drawing of the structure can be found in Appendix 3.

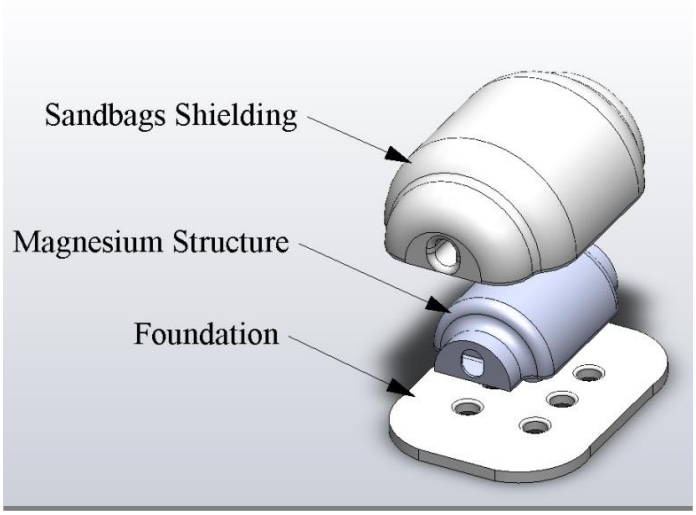

Figure 6.1. Lunar structure.

6.2 Some Definitions

The following are definitions of the jargon being used extensively in seismology.

6.2.1 Body Wave

Seismic waves are divided into two classical types, *P* or compressional waves (also called primary waves), and *S* or shear waves (also called secondary waves). *P* waves are the first arriving waves, having travelled a direct path from the focus of seismic disturbance to the structure (or seismometer), which cause the medium to move back and forth in the direction of propagation. Afterwards, a pulse *pP* that traveled from the focus, reflected off the surface, and arrived at the structure. Second to *P* waves are *S* waves, which cause the medium to move perpendicular to the direction of propagation. Analogous to *P* waves, *sS* waves are the reflected shear waves.

P and *S* waves, including their subcategories, are known as body waves since they travel through the Earth's, or the Moon's, interior. *P* and *S* waves are divided into more categories than discussed here. An interested reader can refer to Stein and Wysession (2003) for more information.

6.2.2 Surface Waves

After the arrival of the body waves, for terrestrial cases, seismograms are dominated by larger longer-period waves. These waves are called surface waves, as these are trapped near the surface of the Earth. In other words, their energy is concentrated near the Earth's surface. These are subcategorized into two types, Love waves and Rayleigh waves. Love waves result from *SH* waves (shear waves polarized in the horizontal plane) trapped near the surface, while Rayleigh waves are a combination of *P* and *SV* (shear waves polarized in the vertical plane) waves that can exist at the top of a homogeneous half-space (Stein and Wysession 2003).

6.2.3 Seismic Coda

In the continental crust, which has many small layers and reflectors, scattering is especially important. These structures cause some of the energy to be scattered and arrive at a receiver later than the initial pulse. The scattered energy arrives from various directions and shows little or no preferred particle motion. Therefore, this scattered energy causes an arrival to have a *coda*, a trail of incoherent energy that decays over seconds or minutes (Stein and Wysession 2003).

6.2.4 Intraplate Earthquakes

Intraplate earthquakes occur within plate interiors when they are not perfectly rigid. In some cases these earthquakes are associated with intraplate volcanism, for example, Hawaii. These are studied, generally, to provide data about where and how the plate tectonic model does not fully describe tectonic processes (Stein and Wysession 2003).

6.3 Modal Analysis (Mode Superposition Method)

As mentioned earlier, random vibration and mode-superposition transient dynamic solvers of ANSYS® software are used for our analyses, both based on the modal superposition method. Therefore, a short summary of modal analysis and theories used are presented to provide the reader a general understanding of these methods (ANSYS Theory Reference 2011, Benaroya and Nagurka 2010, Dill 2012).

Modal analysis (Mode Superposition Method) is a procedure by which the equations of motion (EOM) are transformed from a physical coordinate system to a principal coordinate system where the EOM are decoupled. Each of the decoupled equations

represents a single oscillator. Then, the total response of the system is the linear superposition of the obtained solutions of the decoupled equations. This procedure is valid for undamped systems as well as certain damped systems known as *proportionally damped* systems.[8]

For an N degree-of-freedom (DOF) system, the general equation of motion (EOM) is expressed as

$$[M]\{\ddot{D}\} + [C]\{\dot{D}\} + [K]\{D\} = \{F\}\,, \tag{6.1}$$

where $[M]$ is mass matrix, $[C]$ is the damping matrix, $[K]$ is the stiffness matrix, $\{D\}$ is the nodal displacement vector, and $\{F\}$ is the nodal external force vector.

6.3.1 Free Vibration

Consider an undamped structure displaced a certain amount and then released to oscillate. Since no external forces are exerted, the oscillation is called a *free vibration*, and the EOM becomes

$$[M]\{\ddot{D}\} + [K]\{D\} = \{0\}. \tag{6.2}$$

The modes of vibration and the natural frequencies of vibration are found by solving Equation 6.2 and by assuming a solution of the form $\{D(t)\}=\{D_n \exp(i\omega_n t)\}$, where t is

[8] For an N degree-of-freedom system with general damping, the same procedure as explained in this section results in coupled equations of motion in physical space. These equations can be decoupled in a $2N$ dimension state space, where the complex eigenvalues and vectors can be obtained directly (Bottega 2006). Although simulations that utilize this approach require large computational power, there exist recent efforts to minimize the needed computation power for specific cases by using different approximation methods (Stringer et al. 2010). However, these efforts seem to result in large errors when the damping matrix is not symmetric. Regarding the current study, while ANSYS software can obtain the complex modes of vibration, it does not include the imaginary parts in modal superposition calculations (ANSYS Theory Reference 2011).

time and n is the mode number. The resulting equation is the fundamental eigenvalue problem,

$$([K] - \omega_n^2[M])\{D\}_n = 0, \tag{6.3}$$

where ω_n are the natural circular frequencies (eigenvalues) and $\{D\}_n$ are the modes of vibration (eigenvectors).

Each eigenvector can be normalized with respect to [M],

$$\{\Phi\}_n^T[M]\{\Phi\}_n = 1. \tag{6.4}$$

And, therefore,

$$\{\Phi\}_n^T[K]\{\Phi\}_n = \omega_n^2, \tag{6.5}$$

where $\{\Phi\}$ denotes the normalized mode.

Assuming that the N solutions of Eq. 6.3 have been obtained, the modal vectors satisfy the orthogonality conditions:

$$\{\Phi\}_n^T[K]\{\Phi\}_m = 0, \tag{6.6}$$

$$\{\Phi\}_n^T[M]\{\Phi\}_m = 0, \tag{6.7}$$

for $n \neq m$. The solution $\{D(t)\}$ of Eq. 6.2 can be expressed as a linear combination (superposition) of the mode shapes,

$$\{D(t)\} = \sum_n \{\Phi\}_n q_n(t)$$

$$= [P]\{q_n(t)\}, \qquad (6.8)$$

where $[P]$ is a square matrix whose columns are the mode shape vectors, and $q_n(t)$ are known modal displacements that are found in the modal analysis solution. Therefore, the equations are decoupled and can be solved using the initial conditions.

6.3.2 Forced Vibration (Transient Analysis)

The EOM for an undamped forced system is

$$[M]\{\ddot{D}\} + [K]\{D\} = \{F(t)\}. \qquad (6.9)$$

Substituting Equation 6.8 and its second derivative into Equation 6.9 and using the normalization Equations 6.6 and 6.7 leads to

$$[I]\{\ddot{q}_n(t)\} + [\Omega]\{q_n(t)\} = [P]^T\{F(t)\}, \qquad (6.10)$$

where $[I]$ is the identity matrix and $[\Omega]$ is a diagonal matrix whose elements are the natural frequencies such that $\Omega_{ii} = \omega_i^2$. The decoupled Equations 6.18 can be solved using the Duhamel integral and by considering the initial conditions.

In ANSYS Workbench "transient structural" solver, the ground excitation option is nonexistent. Therefore, when using this method, we will apply the ground acceleration to the entire structure.

6.3.3 Forced Vibration (Random Vibration)

Here a summary of the method used by ANSYS random vibration solver is presented (ANSYS Theory Reference 2011). The equations are modified for an undamped system. The EOM for a forced undamped system can be partitioned into the free and the restrained (support) degrees-of-freedom (DOFs) as

$$\begin{bmatrix}[M_{ff}] & [M_{fr}]\\ [M_{rf}] & [M_{rr}]\end{bmatrix}\begin{Bmatrix}\{\ddot{D}_f\}\\ \{\ddot{D}_r\}\end{Bmatrix}+\begin{bmatrix}[K_{ff}] & [K_{fr}]\\ [K_{rf}] & [K_{rr}]\end{bmatrix}\begin{Bmatrix}\{D_f\}\\ \{D_r\}\end{Bmatrix}=\begin{Bmatrix}\{F\}\\ \{0\}\end{Bmatrix}, \tag{6.11}$$

where $\{D_f\}$ are the free DOFs and $\{D_f\}$ are the restrained DOFs that are excited by random loading (note that the restrained DOFs that are not excited are not included). $\{F\}$ is the nodal force excitation activated by a nonzero force.

The free displacements are decomposed into pseudo-static, $\{D_s\}$, and dynamic, $\{D_d\}$, parts,

$$\{D_f\}=\{D_s\}+\{D_d\}. \tag{6.12}$$

The pseudo-static displacements are obtained from Equation 6.11 by excluding the acceleration of the equation and by replacing $\{D_f\}$ by $\{D_s\}$, therefore,

$$\{D_s\}=-[K_{ff}]^{-1}[K_{fr}]\{D_r\}=[A]\{D_r\}, \tag{6.13}$$

where $[A] = -[K_{ff}]^{-1}[K_{fr}]$. Physically, the elements along the i^{th} column of $[A]$ are the pseudo-static displacements due to a unit displacement of the support DOFs excited by the i^{th} base PSD. Substituting Equations 6.12 and 6.13 into 6.11 results in

$$[M_{ff}]\{\ddot{D}_d\} + [K_{ff}]\{D_d\} \cong \{F\} - \left([M_{ff}][A] + [M_{fr}]\right)\{\ddot{D}_r\}, \tag{6.14}$$

where the second term on the right-hand side are the equivalent forces due to support excitation. Modal superposition can be used to decouple the simultaneous ordinary EOMs in Equation 6.14 as follows. Assuming

$$\{D_d(t)\} = [\Phi\ ]\{q(t)\}, \tag{6.15}$$

the decoupled Equation 6.14 becomes

$$[I]\{\ddot{q}_n(t)\} + [\Omega]\{q_n(t)\} = \{G_n\}, \tag{6.16}$$

where G_n are defined by

$$G_n = \{\Gamma_n\}\{\ddot{D}_r\} + \gamma_n, \tag{6.17}$$

and where $\{\Gamma_n\}$ are the modal participation factors corresponding to support excitation and γ_n are those for nodal excitation, given by

$$\{\Gamma_n\} = -\left([M_{ff}][A] + [M_{fr}]\right)^T\{\Phi_n\}, \tag{6.18}$$

$$\gamma_n = \{\Phi_n\}^T\{F\}. \tag{6.19}$$

From the theories of random vibration and linear systems it is known that the input spectral density, $S_{FF}(\omega)$, and the system frequency response of a single DOF system, $S_{DD}(\omega)$, can be related using

$$S_{DD}(\omega) = H(\omega)H^*(\omega)S_{FF}(\omega), \tag{6.20}$$

(Benaroya and Han 2005) where * denotes complex conjugate and $H(\omega)$ is the transfer function. When the input is force or acceleration, the transfer function is

$$H(\omega) = 1/(\omega_n^2 - \omega^2), \tag{6.21}$$

where ω_n is the natural frequency.

Using mode superposition techniques, Equation 6.20 for the i^{th} DOF becomes

$$S_{d_i}(\omega) = \sum_{j=1}^{n}\sum_{k=1}^{n} \Phi_{ij}\Phi_{ik}\left(\sum_{l=1}^{r_1}\sum_{m=1}^{r_1} \gamma_{lj}\gamma_{mk}H_j^*(\omega)H_k(\omega)S_{lm}(\omega)\right.$$

$$\left.\sum_{l=1}^{r_2}\sum_{m=1}^{r_2} \Gamma_{lj}\Gamma_{mk}H_j^*(\omega)H_k(\omega)\mathrm{S}_{lm}(\omega)\right), \tag{6.22}$$

$$S_{s_i}(\omega) = \sum_{l=1}^{r_2}\sum_{m=1}^{r_2} A_{il}\gamma_{im}\left(\frac{1}{\omega^4}S_{lm}(\omega)\right), \tag{6.23}$$

and,

$$S_{sd_i}(\omega)$$

$$= \sum_{j=1}^{n}\sum_{l=1}^{r_2}\sum_{m=1}^{r_2} \Phi_{ij}A_{il}\left(-\frac{1}{\omega^2}\Gamma_{mj}H_j(\omega)S_{lm}(\omega)\right), \tag{6.24}$$

for the dynamic, pseudo-static, and covariance parts, respectively. n is the number of mode shapes chosen. r_1 is the number of nodes away from support which are excited by an external load. r_2 is the number of the nodes excited by an external load.

The external load can be the power spectrum of ground displacement, velocity, or acceleration. Subsequently, the variances can be calculated, and stresses can be obtained

using similar approaches. For a more detailed analysis the reader may refer to ANSYS Theory Reference (2011).

6.4 Introduction to Lunar Seismicity

As a part of the Apollo missions, the Apollo Passive Seismic Experiments (APSE) were carried out. These experiments revealed that the Moon is by no means a seismically dead planet. During the operation period of the APSE data were collected and processed by many researchers. It has been estimated that the largest moonquakes observed could have had a body-wave magnitude greater than 5.5 Richter. However, due to dissimilarities between the internal structures of the Moon and the Earth, the effect of the moonquake is expected to be quite different from what would be expected for an earthquake of equal magnitude. These differences do not necessarily eliminate the danger posed by lunar seismic activities. Therefore, a response analysis of the proposed lunar structure under seismic excitation is necessary.

6.5 Apollo Passive Seismic Experiments

The APSE, a network of four seismometers, was installed on the surface of the Moon as a part of the Apollo Lunar Surface Experiments Package (ALSP). Data were collected and transmitted back to the Earth from 1969 to 1977 (Nakamura et al. 1982). The term “passive” was used because the principal objective of the experiment was to detect naturally occurring seismic events on the surface of the Moon (Latham et al. 1969).

The passive seismic experiment package sensor unit contained three orthogonally-aligned long-period seismometers to measure surface motion in the vertical and two horizontal

directions, and a single-axis short-period seismometer sensitive to vertical motion at higher frequencies. The long-period seismometers were designed with resonant frequencies of 1/15 Hz, and the short-period seismometer with a resonant frequency of 1 Hz (Latham et al. 1970). The PSEP and its component of the low-frequency seismometers are shown schematically in Fig. 6.2 and Fig. 6.3, respectively.

6.6 Lunar Seismicity

During the eight years of network operations, more than 12,000 seismic events were detected. Four distinct types of natural seismic sources have been identified: deep moonquakes, thermal moonquakes, meteoroid impacts, and shallow moonquakes (Nakamura et al. 1982).

6.6.1 Deep Moonquakes

These are the most abundant type of moonquakes, with 973 confirmed events (Vaniman et al. 1991). Most of their foci occured within a clearly defined region between the depths of 800 km to 1000 km. Their occurrence is strongly correlated with the tidal forces on the Moon due to the Earth and the Sun (Nakamura et al. 1982). These are low frequency, low magnitude events and are unlikely to pose a potential danger to a lunar structure. A body wave magnitude of 1.3 to 3.0 Richter is estimated for a large deep moonquake (Goins et al. 1981).

6.6.2 Thermal Moonquakes

These are very unlikely to pose any threat to a lunar structure, as they are very small seismic events caused by temperature variations at or near the lunar surface. Although

their exact cause is unknown, it is believed that they originate in young craters and large rocks (Nakamura et al. 1982).

6.6.3 Meteoroid Impacts

A total of 1734 meteoroid impacts have been distinguished from the APSE data (Vaniman et al. 1991) – while the actual number is much greater – the long period seismographs were capable of detecting mainly the signals from objects of mass 0.1 kg and higher. The largest meteoroid mass has been estimated at about 2000 kg based on an assumed impact velocity of 22.5 km/s (Dorman et al. 1978).

6.6.4 Shallow Moonquakes

Shallow moonquakes, also called high-frequency teleseismic (HFT) events, are the most energetic and also the rarest seismic sources that have been observed on the Moon. A total number of 32 events have been distinguished (Vaniman et al. 1991). The name HFT is used for these events due to their unusually high frequency content and great distance at which they were observed (Nakamura et al. 1979). Body wave magnitude estimates are in the range of about 5 Richter (Goins et al. 1981, Oberst and Nakamura 1992) to 5.5 Richter (Oberst 1987) for the largest shallow moonquake. The epicenters of all the detected HFT events were located outside the Apollo seismic array, and the number of recorded events was small, thus limiting our understanding of these events (see Fig. 6.4). The actual depths of the HTF events are undetermined, but are estimated at less than 200 km (Nakamura et al. 1979). The cause of these events is yet unknown, although theories have been proposed:

(a) the result of a lasting tectonic influence of impact basins long after their formation, comparable to shallow intraplate earthquakes that occur on Earth (Nakamura et al. 1979),

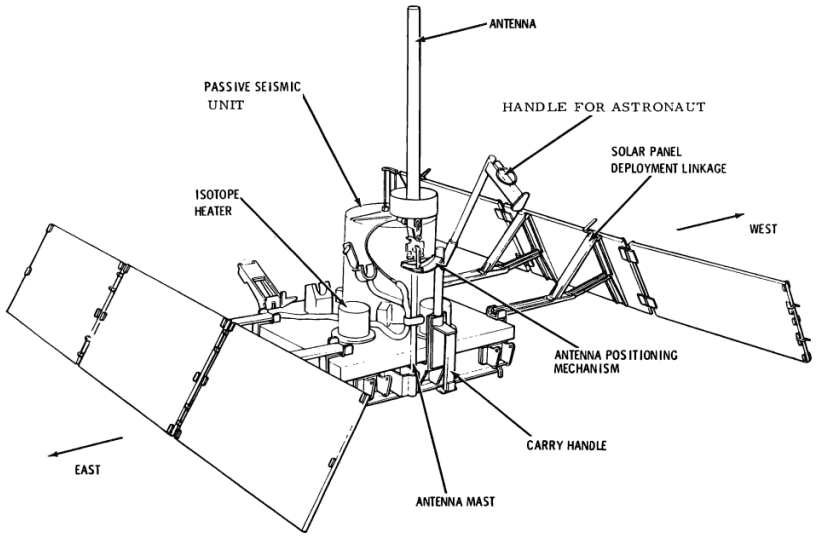

Figure 6.2. Diagram of the fully erected PSEP (Latham et al. 1970, courtesy of NASA and Lunar and Planetary Institute).

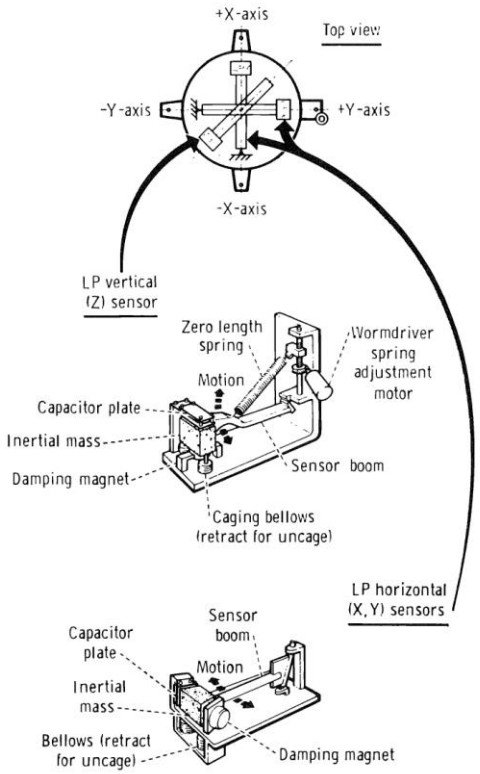

Figure 6.3: Schematic diagrams of the elements of the low-frequency seismometers (Latham et al. 1970, courtesy of NASA and Lunar and Planetary Institute).

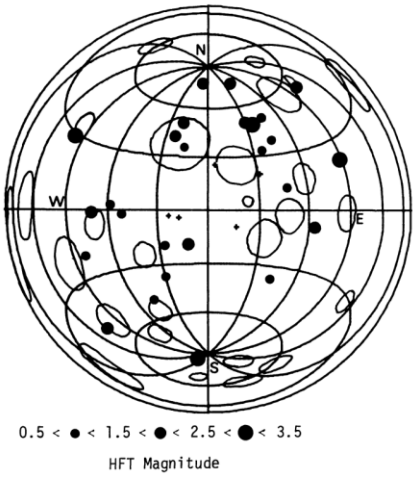

Figure 6.4. Distributions of shallow moonquake epicenters and impact basins. N represents the north pole and S the south pole. The "+" signs are the PSEP locations (Nakamura et al. 1979, courtesy of NASA and Lunar and Planetary Institute).

(b) associated with young thrust fault scarps in the lunar highland (Oberst and Nakamura 1992). A different suggestion is that these events are caused by a high-energy object from a fixed source outside the Solar System (Frohlich and Nakamura 2006).

6.7 Seismic Risks for Lunar Structures

The last two of the categories above, meteoroid impacts and shallow moonquakes, pose the greatest threats to a potential lunar base. The two-ton meteoroid mentioned above contains a linear momentum of 4.5e7 Ns, and could destroy any manmade structure. Moreover, meteoroids of any size can cause life-threatening injuries to the astronauts. These rare events are beyond the current study, which is focused on the seismic risks associated with shallow moonquakes.

As mentioned earlier, shallow moonquakes with estimated magnitudes as large as 5.5 Richter were recorded by ASEP. While the terrestrial equivalent can be fatal, causing moderate damage to buildings, their effects on the lunar base is not the same since the lunar interior structure is very different than that of the Earth. The seismic coda, defined as the seismic energy delayed by scattering, has been observed both on the Moon and the Earth. On the Moon the seismic coda is very large compared to that of Earth (Dainty and Toksoz 1981), which reduces the potential damage to a lunar structure since the seismic energy is scattered over tens of minutes (Dainty and Toksoz 1981, Goins et al. 1981, Oberst and Nakamura 1992).

Even though we have much more knowledge about the Earth, we still face many challenges in predicting earthquakes and their effect. Moonquake, due to minimal data and limited knowledge of the Moon's interior, are studied with a realization that any results are, at best, very approximate.

6.8 Shallow Moonquakes Seismograms

The lunar seismograms associated with shallow moonquakes are of very long duration, even over an hour. These large seismic codas were first observed as coherent trains of surface waves, having been compared to the terrestrial seismic events (Dainty et al. 1974). However, surface wave particle motion and dispersion in the seismic coda were not identified, thus questioning the assumption of surface waves scattering (Goins et al. 1981). Figures 6.5 and 6.6 show typical seismographs recorded for shallow moonquakes.

Although different types of seismic waves could not be identified throughout the seismic coda, the following common features were observed:

- The amplitude builds up to a maximum during the first 10 min (known as the rise time), depending on the epicentral distance and focal depth, then decays very gradually with time. Body waves are present in the first minute of the seismogram, but these are very small. (Dainty and Toksoz 1981, Nakamura and Koyama 1982).
- The frequency of the signals is predominantly in the 2 Hz to 4 Hz range (Nakamura et al. 1979).
- For frequencies higher than 5 Hz most of the energy is lost because of attenuation in the scattering layer (Oberst 1987).

The much larger amplitude (compared to direct phases[9]) and much longer coda, when compared to terrestrial ones, suggests more intense scattering as well as much lower attenuation on the Moon than on the Earth. Various theories were put forward to explain this phenomenon, and of these the diffusion scattering model seems to be the best fit for the frequency range of 0.5 to 10 Hz (Dainty and Toksoz 1981). It worth noting that efforts to identify lunar seismic phases and use them to study the Moon's internal structure have been generally unsuccessful (Stein and Wysession 2003), but yet diffusion scattering is the best available model.

6.9 Diffusion Formalism

An elastic pulse propagates without change in shape in an ideal, infinite, homogeneous, non-dispersive, and elastic medium. However, in heterogeneous media, a single seismic pulse is rapidly converted into a long train of pulses. The gross feature of a seismogram, as mentioned earlier, is the result of body and surface waves, which travel with different speeds. Therefore, the number of possible ray paths becomes quite large and the overall process takes a diffusive form. The seismic energy, E, per unit volume within a unit frequency band can be approximated by the diffusion equation (Wesley 1965),

[9] Direct phases are the seismic waves that have not been scattered.

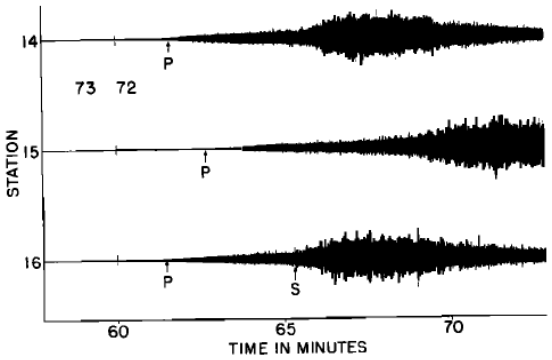

Figure 6.5. Typical seismogram recorded by the short-period vertical instruments at stations 14, 15, and 16 from the March 12, 1973 shallow moonquake (Goins et al. 1981, with permission from John Wiley and Sons).

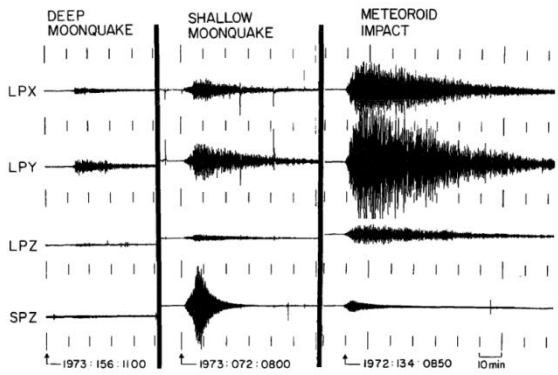

Figure 6.6: Representative lunar seismograms in compressed time scale (Nakamura et al. 1982, with permission from John Wiley and Sons).

$$\partial E/\partial t = D\nabla^2 E\,, \tag{6.25}$$

where D is the diffusivity, and t is the time the seismic wave traveled. The diffusion equation does not consider the anelastic[10] conversion of the seismic energy to heat.

[10] *Anelasticity*, also called *intrinsic attenuation*, is a process where the kinetic energy of elastic wave motion is converted to heat. This is due to the permanent deformation of the medium (Stein and Wysession 2003).

Therefore, considering the anelastic loss and conservation of energy leads to a modified diffusion Equation 6.26 for a three-dimensional, strong, isotropic scattering medium (Aki and Chouet 1975, Dainty and Tokoz 1981),

$$\partial E/\partial t = D\nabla^2 E - (\omega/Q)E, \tag{6.26}$$

$$D = VL/3, \tag{6.27}$$

where Q is the non-dimensional intrinsic quality factor due to anelastic conversion of seismic energy to heat, and does not include the loss by scattering. V is the velocity of seismic waves in the medium and is considered to be the shear wave velocity since most scattered energy is expected to be via shear waves. L is known as the mean free path and is the average distance seismic energy travels before it is scattered.

Aki and Chouet (1975) and Dainty and Tokoz (1981) presented a solution to Equation 6.26 by using the Green's function for a point source,

$$E(R,t,\omega) = \frac{E_0(\omega)}{(4\pi Dt)^{3/2}} exp\left(\frac{-R^2}{4Dt} - \frac{\omega t}{Q}\right), \tag{6.28}$$

where $E_0(\omega)$ is the total seismic energy generated by the seismic events within a unit frequency band around ω at $t = 0$ and $R = 0$, where R is the distance from the focus.

For large t and very small distance, Equation 6.28 becomes a function of time only. Also, the seismic energy per unit volume is twice the kinetic energy for propagating waves or stationary vibration. Therefore, the coda power spectrum of the ground displacement, $S_{xx}(\omega,t)$, can be obtained as (Aki and Chouet 1975),

$$\rho_f \omega^2 S_{xx}(\omega, t) = E(0, t, \omega) \,, \tag{6.29}$$

where ρ_f is the average soil density at the focus.

Next, we assume that the location of our lunar surface structure is known, as is the moonquake focus. Therefore, the distance R is no longer a variable. Using the same approach as above, the coda power spectrum at the base will be

$$\rho \omega^2 S_{xx}(\omega, t) = E(R, t, \omega) \,, \tag{6.30}$$

where ρ is the average density of regolith in vicinity of the base. By substituting Equation 6.30 into 6.28, the coda power at the base is obtained as

$$S_{xx}(\omega, t) = \frac{E_0(\omega)}{\rho \omega^2 (4\pi D t)^{3/2}} exp\left(\frac{-R^2}{4Dt} - \frac{\omega t}{Q}\right), \qquad \text{for } t > t_i \,, \tag{6.31}$$

where t_i is the time after the start of the seismic event when the first seismic waves reach the base.

We know that acceleration is the second derivative of displacement with respect to time and that $S_{\ddot{x}\ddot{x}}(\omega,t) = \omega^4 S_{xx}(\omega,t)$. Therefore, the power spectrum of ground acceleration is

$$S_{\ddot{x}\ddot{x}}(\omega, t) = \frac{\omega^2 E_0(\omega)}{\rho (4\pi D t)^{3/2}} exp\left(\frac{-R^2}{4Dt} - \frac{\omega t}{Q}\right), \qquad \text{for } t > t_i \,. \tag{6.32}$$

6.10 Parameters and Material Properties

In order to investigate the seismic structural response of our typical lunar structure, numerical values must be assigned to Equation 6.8 and material properties must be specified.

6.10.1 Power Spectral Density of Ground Acceleration

Many researchers have devoted their efforts to model moonquakes using the modified diffusion equation, yet there exist many uncertainties associated with each of the parameters in Equation 6.32.

Regarding the diffusivity, *D*, different values have been proposed and used in the literature. Nakamura (1976) applied a two-dimensional scattering model to the seismic signals generated by movement of the lunar rovers and obtained diffusivities from 0.018 km^2/s to 0.033 km^2/s for ranges of about 1 km. Toksoz et al. (1974) studied the near impacts received at the Alsep 12 site and obtained a horizontal diffusivity of 2 km^2/s for ranges less than 150 km. Also, they expected that the diffusivity would be a strong function of frequency, and the effective diffusivity would be different for vertical and horizontal planes. Dainty et al. (1974) explained this by the fact that all types of waves propagate horizontally, whereas only compressional and shear waves propagate vertically. Also, they discussed that the diffusivity cannot be the same for different types of seismic waves, as they propagate at different speeds (see Equation 6.27). However, lunar seismograms demonstrate the same energy envelopes for the horizontal and vertical components of displacement, i.e., different waves cannot diffuse independently.

Nakamura and Koyama (1982) investigated the frequency dependency of anelastic attenuation for both *P* and *S* waves in the upper mantle of the Moon for the frequency range of roughly 3 Hz to 8 Hz. They estimated that the intrinsic quality factor, *Q*, is almost constant across the frequency range and is equal to 4000 for the *P* waves in the upper mantle of the Moon, while *Q* for *S* waves increases from at least 4000 at 3 Hz to at least 7000 at 8 Hz. They could not overcome the uncertainties in the absolute value of *Q* due to the unknown velocity structure[11] of the Moon.

For our analysis we choose the focus distance to the base to be R = 25 km and the density ρ = 1740 kg/m^3 (Williams and Jadwick 1980). While body wave magnitudes of 5.5 Richter have been estimated for the largest lunar events, for our analysis we consider a very conservative event of magnitude 7 Richter. We calculate the energy release at the source, m_b, in the same way as Oberst and Nakamura (1992) ($m_b = (\log E + 1.2) / 2.4$), and find it to be $10^{15.6}$ J. The frequency range is selected to be 0.5 Hz to 10 Hz, since the diffuse scattering model is reported to be well-suited for this range (Dainty and Toksoz 1981).

For different values of *D* and *Q* in the literature, a normally distributed $E_0(\omega)$ seems to satisfy the general characteristics of the lunar seismic coda mentioned in Section 6.5. Therefore, the amplitude of the source is assumed to be Gaussian-distributed over the above frequency range with mean located at 3 Hz and a standard deviation of 1 Hz. Considering the selected magnitude of the event as 7 Richter, the source becomes:

[11] Velocity structure of the Earth can be viewed as a geological map that depicts how different types of seismic waves travel in the interior of the Earth. Here the same concept is meant for the Moon.

$$E_0(\omega) = \frac{10^{15.6}}{0.99379(2\pi)^{3/2}}\ exp\left(\frac{-1}{2}\left(\frac{\omega - 6\pi}{2\pi}\right)^2\right), \tag{6.33}$$

The number 0.99379 in the denominator is obtained by normalizing over the frequency range of 0.5 Hz to 10 Hz. Therefore, 100.0000 percent of magnitude remains in the frequency range.

Then, D = 0.22 km^2/s and Q = 8000 are chosen for Equation 6.32 in such a way so as to obtain the most intense power spectrum for the selected distance R. The resulting PSD is shown in Figure 6.7.

6.10.2 A Realization of the Seismic Signal

In order to carry out the transient response, the ground acceleration power spectrum, $S_{\ddot{x}\ddot{x}}(\omega)$ needs to be converted into an equivalent time history. The power spectrum can be represented as a sum of many sinusoidal functions with different angular frequencies and random phase angle (Benaroya and Han 2005), resulting in the time history

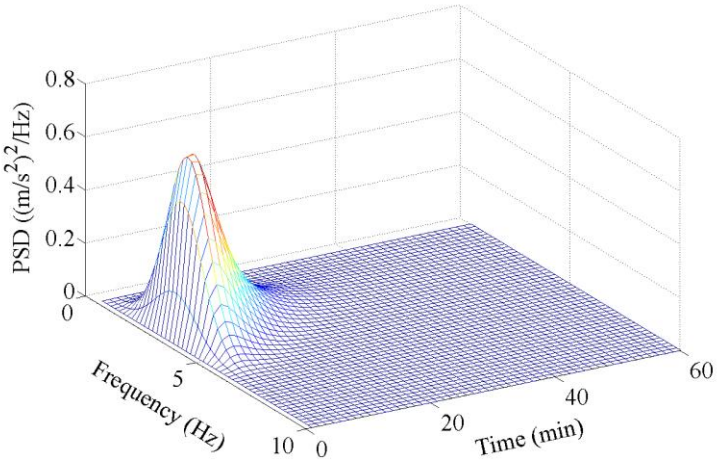

Figure 6.7. Power spectral density of ground acceleration.

$$a(t) = \sum_{i=1}^{N} \cos(\omega_i t - \varphi_i)\sqrt{2S_{\ddot{x}\ddot{x}}(\omega_i)\Delta\omega_i} \ , \tag{6.34}$$

where φ_i is a uniformly distributed random number between 0 and 2π, ω_i are discrete sampling frequencies, $\Delta\omega_i = \omega_i - \omega_{i-1}$, and N is the number of partitions.

The power spectrum presented by Equation 6.8 is a non-stationary (time-dependent) spectrum, while the spectrum in Equation 6.34 is a stationary one. The "uncertainty principle" proposed by Priestley (1967) states that "in the empirical determination of time-varying spectra, we cannot obtain simultaneously an arbitrary high degree of resolution in both the time domain and the frequency domain." That is also true for the inverse problem in hand. Having this in mind, the spectrum presented by Equation 6.8 and depicted in Figure 6.7 can be assumed to be a weakly stationary process.

Therefore, we assume that the time domain is divided to intervals of one minute duration, where the power spectrum is estimated by stationary spectra equal to the wave elevations at the mid-points of each time interval. Therefore, a realization of the ground acceleration signal is obtained by considering these stationary spectra for their assigned time intervals and $\Delta\omega_i = 2\pi/250$. A representative signal is generated using Matlab software and is depicted in Figure 6.8.

In evaluating this result (Fig. 6.8) the wave elevations at frequencies higher than 5 Hz are neglected in order to reduce the computational power. As it is well-known by the Nyquist-Shannon sampling theorem, if a function contains no frequencies higher than f_0 Hz, a series of sampling point with highest time step of $1/2\ f_0$ seconds is needed to avoid

aliasing. Therefore, neglecting frequencies higher than 5 Hz allows simulations of longer duration with a good accuracy, because the neglected part of the spectrum contains only four percent of the total energy of the complete spectrum Figure 6.7.

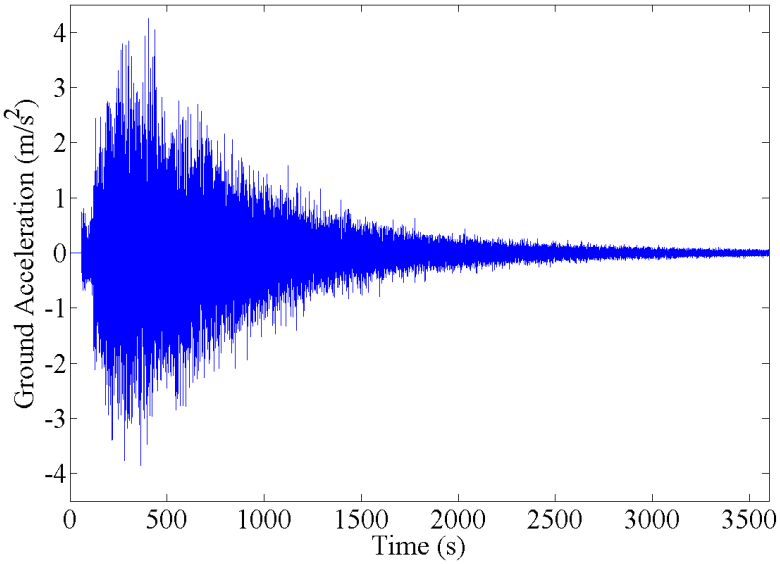

Figure 6.8. A realization of seismic ground acceleration.

6.10.3 Material Models and Properties

Having obtained a representative PSD and seismic signal, we wish to carry out a modal analysis. While magnesium and concrete can be considered as isotropic media, sandbag dynamics are very complicated. Although using nonlinear models such as the Mohr-Coulomb model seem to give a good prediction of the sandbag dynamics (Ansari et al. 2011), they cannot be used in a modal analysis which is based on linear superposition.

Considering nonlinear models for transient dynamic simulations require very large computational power. Therefore, to simplify our computational analysis, an assumption is made that the sandbags are designed in a way that they retain their general configuration during moonquakes and therefore an elastic model can be considered. In modal analysis, generally the first few modes contribute the most to the final results. Therefore, the assumption made here implies that the small local plastic deformations would only affect modes higher than those considered.

For our analysis, the magnesium (Mg) physical properties selected are the same as those of pure sand cast magnesium (Avedesian and Baker 1999), the foundation is taken to be made of lunar regolith (Happel 1993), and the properties of the sandbags are taken to be those of the typical sandbag of Ansari et al. (2011). These are summarized in Table 6.1, where the tensile yield strength of the foundation is assumed to be the same as for regular cements.

Table 6.1. Physical Properties Selected.

	Mg	Foundation	Sandbags
Density (ρ), kg/m3	1738	2500	1650
Young's Modulus (E), GPa	40 (Static) 44 (Dynamic)	21.4	0.06
Poisson's Ratio (υ)	0.35	0.21	0.3
Tensile Yield Strength, MPa	21	5	-
Compressive Yield Strength, MPa	21	7.07	-

6.11 Numerical Analysis and Results

In both random vibration and transient analyses, ANSYS® Academic Research Workbench, Release 14.0 software is used for the numerical simulations.

6.11.1 Random Vibration Analysis

A total of 225,088 nodes and 179610 elements (consisting of 2100 SOLID186, 138960 SOLID187, 13808 CONTA174, 13808 TARGE170, 10934 SURF154 elements) are generated. A static analysis and a prestressed[12] undamped modal analysis are performed.

In our static analysis, the boundary and loading conditions are selected as a fixed support applied to the bottom surface of the foundation, internal air pressure of 1 atm acting on all the interior surfaces, and 1.63 m/s^2 gravitational acceleration. All the contact surfaces are assumed to be bonded. The stresses and strains are calculated and included in the modal analysis.

Modal analysis is performed using the sparse (direct) solver. This solver (including the Block Lanczos method for modal and buckling analyses) is based on a direct elimination of equations, as opposed to the iterative solver (ANSYS 14.0 Help[c]). In order to be conservative damping is not included, even though concretes have damping ratios of about 2% (Amik and Monteiro 2005) and terrestrial granular soils can exhibit damping ratios of 1-34% under seismic loading (Ishibashi and Zhang 1993).

[12] Prestress analysis modal analysis is where the static analysis is performed first, and then the resulting stresses and strains are included in evaluating the structural modes.

The first 20 modes are obtained and the first 12 modes are selected and included in a random vibration analysis such that the ratio of the cumulative effective mass to total mass (M) reaches a minimum of 90%[13] for all *x*, *y* and *z* directions. However, fewer modes would suffice since the fundamental frequency associated with a movement in the *x*-direction, which is the direction with the lowest stiffness, is the selected direction for seismic loads in our analysis. The natural frequencies associated with the first 12 modes and the ratios of the cumulative effective mass to total mass for the *x*, *y* and *z* directions (*Mx*, *My*, and *Mz*, respectively) are given in Table 6.2. The details on how the cumulative effective mass ratio is calculated can be found in Appendix 1, Section A1.3.

Random vibration analysis (in ANSYS) is used to obtain the response to seismic excitation. Lunar excitations are of very long codas (see Figure 6.7) and in a time window of several minutes it can be assumed to be a stationary process. Therefore, we make another conservative assumption and choose the spectrum at the time with highest value (at 5.9 min) as the stationary PSD. This PSD of ground acceleration, as shown in Figure 6.9, is applied to the fixed support of the static analysis, that is, only the nodes at the fixed support are excited by the ground acceleration.

The resulting static stress is shown in Figure 6.10. Also, Figures 6.11, 6.12 and 6.13 depict the normal stresses in *x*, *y* and *z* directions, respectively, where a scale factor of 3 Sigma (99.737% of the time) has been used to obtain these normal stresses. Note that the stress directions cannot be combined in the usual way, as these are statistical in nature. A meaningful equivalent stress is obtained using a special algorithm proposed by Segalman

[13] According to ACI 371R-08 for each model, the selected number of modes must have the cumulative mass ratio of at least 90% in the direction of seismic loading for water tanks (Moslemi et al. 2011). Note the similarity between water tanks and the thin-walled structure consider here.

and Fulcher (ANSYS 14.0 Help[b]). A short summary of this method is presented in Appendix 1, Sec. A1.4.

Table 6.2. The first 12 modes, natural frequencies, and cumulative mass ratios.

Mode	Frequency (Hz)	Mx	My	Mz
1	7.12318	0.921916	0.3259E-07	0.1037E-05
2	7.48658	0.921916	0.4435E-07	0.2880E-04
3	7.57750	0.921917	0.4443E-07	0.765552
4	8.12391	0.962620	0.6908E-06	0.765552
5	8.43596	0.962621	0.9521E-01	0.765552
6	9.01120	0.962621	0.9521E-01	0.765552
7	9.79641	0.962621	0.743113	0.765552
8	10.1445	0.962621	0.743113	0.973952
9	10.2687	0.962621	0.743113	0.973952
10	10.3165	0.962621	0.743113	0.999763
11	10.5421	0.979402	0.743114	0.999763
12	10.6966	0.979402	0.905534	0.999764

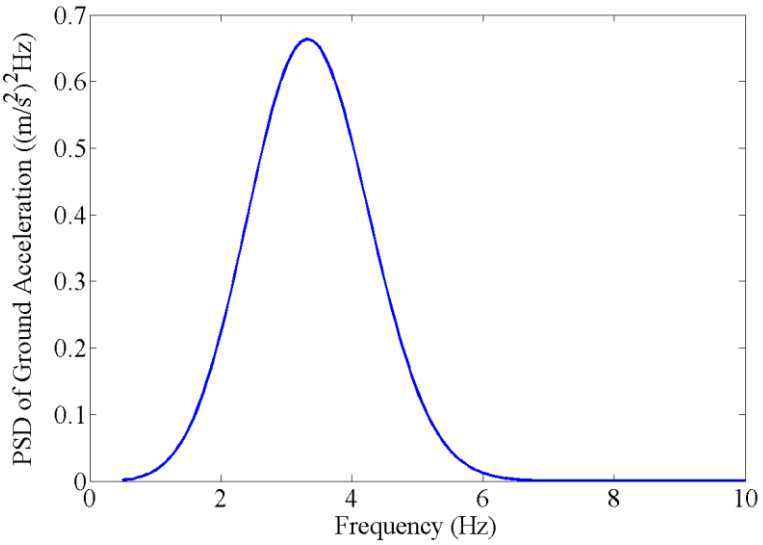

Figure 6.9. PSD of ground acceleration at 5.9 minutes.

Choosing the Segalman and Fulcher algorithm, the maximum stress in the magnesium structure is of magnitude 3.9313 MPa, as shown in Figure 6.14. Note that the stress distribution is obtained by using a probability distribution that is not Gaussian and its mean value is not zero. The stress values are just conservative estimates of the upper bound of the equivalent stresses, where the distribution of principal stress is set to zero (ANSYS Theory Reference). However, in order to estimate the total stress, we obtain a rough estimation of the maximum stress by linear superposition of the maximum of static and dynamic stresses, assuming these could occur at the same location. Therefore, the estimated maximum stress is 7.92 MPa, where the maximum principal static stress (Figure 6.10) and maximum equivalent (dynamic) stress (Figure 6.15) are added.

In calculating the maximum stress above, we have used the maximum principal stress of our static analysis, while von Mises equivalent stress is commonly used to predict yielding in ductile materials.[14] The reason is that maximum principal stress result is a slightly larger result. Instead, using von Mises stress from static analysis results in a maximum value equal to 7.41 MPa.

Since the correlation between static and dynamic stresses is unknown, node by node superposion of the static and dynamic stresses cannot be justified. However, if the stresses and their corresponding nodes are extracted from the solution of our static analysis (Figure 6.10) and added to the stresses from the random vibration analysis (Figure 6.15) for the same nodes, the maximum total stress is 5.81 MPa.

[14] In order to estimate the yield of ductile materials, maximum equivalent stress failure theory is commonly used. This theory is also called, von Mises-Hencky theory, octahedral shear stress theory, or maximum distortion (or shear) energy theory. In this method, the energy of distortion is compared with the distortion energy for yield in uniaxial tension. Therefore, in order to obtain the factor of safety, one can obtain the von Mises stress and compare it to the tensile yield strength. The von Mises stress, σ_e, is obtained as $\sigma_e = (½ [(\sigma_1 - \sigma_2)^2 + (\sigma_2 - \sigma_3)^2 + (\sigma_3 - \sigma_1)^2])^{1/2}$, where σ_1, σ_2, and σ_3 are the principal stresses.

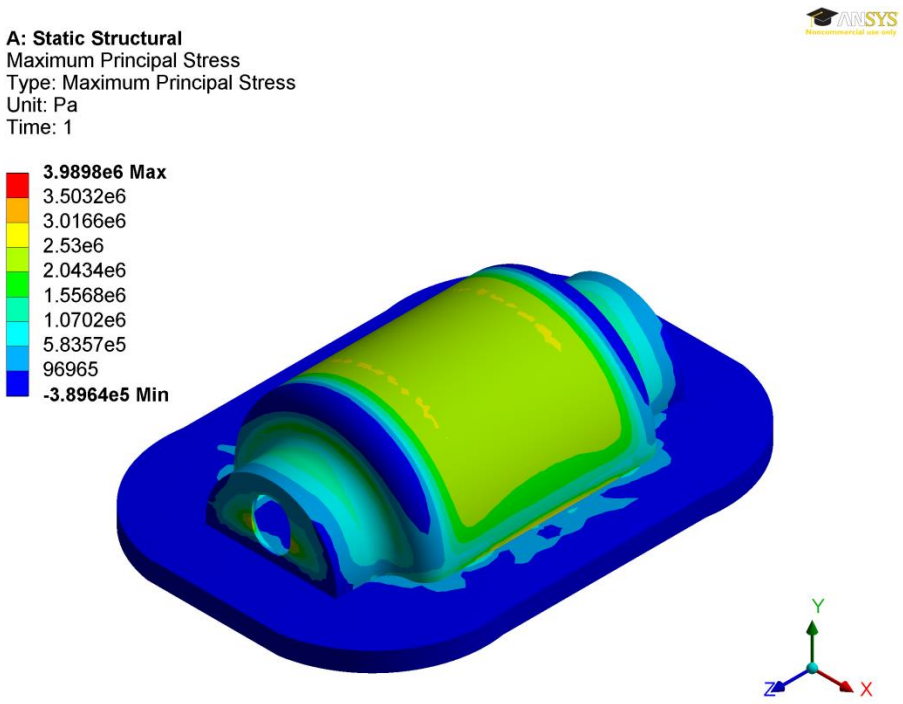

Figure 6.10. Maximum principal stress for static analysis (maximum stress = 3.9898e6 Pa).

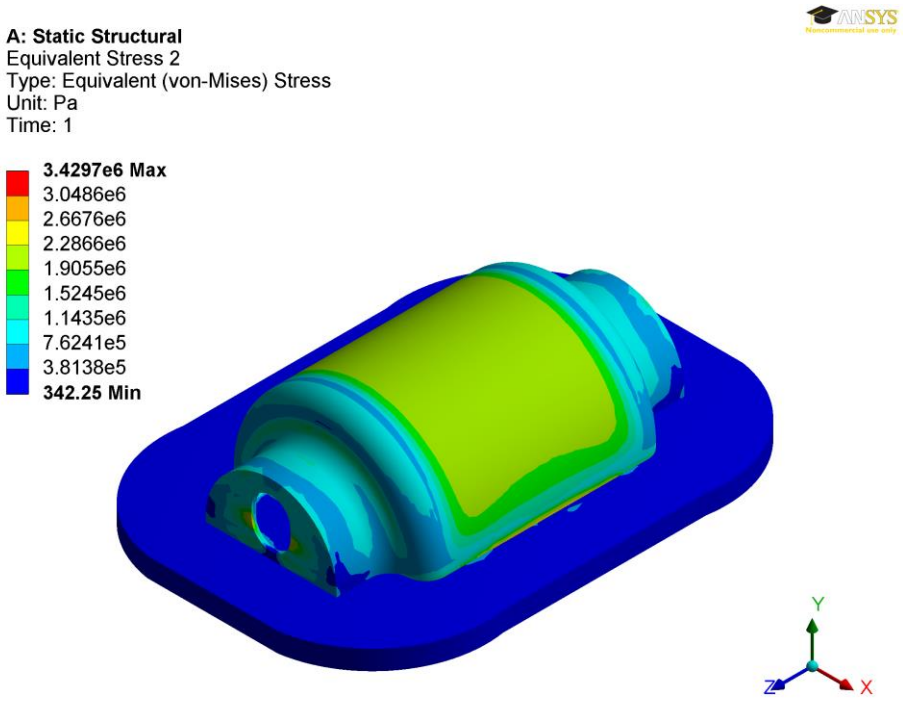

Figure 6.11. Equivalent (von-Mises) stress for the static analysis, maximum = 3.4297e6 Pa.

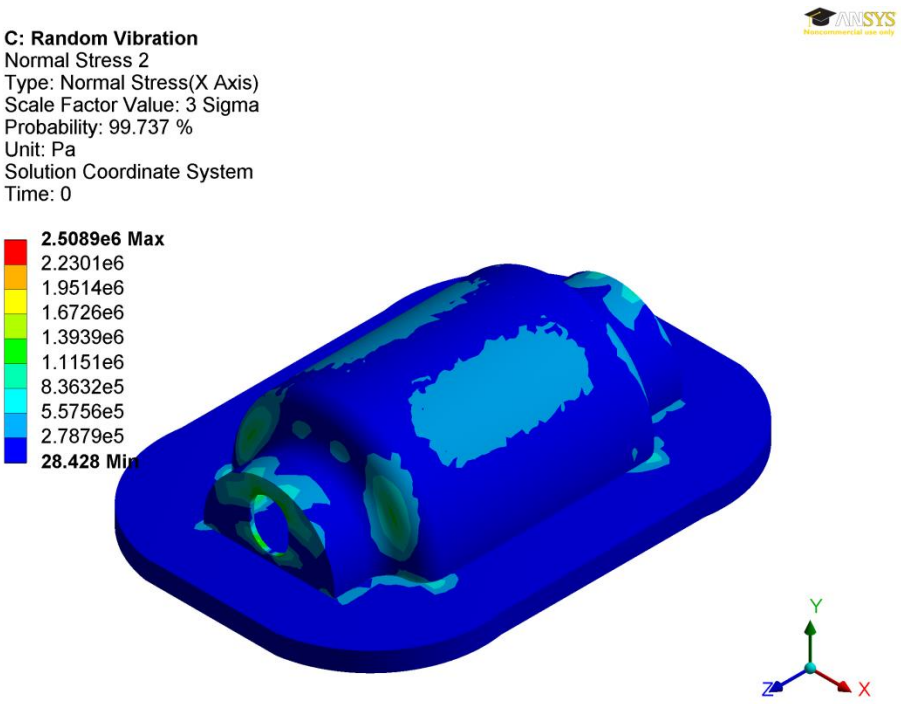

Figure 6.12.Maximum normal stress (X Axis), maximum = 2.5089e6 Pa.

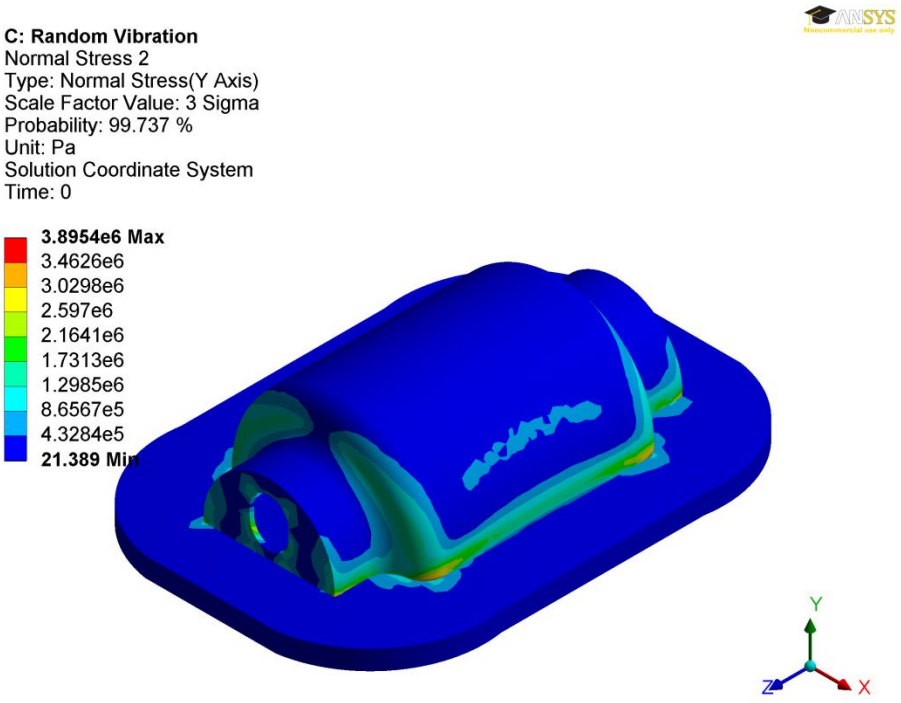

Figure 6.13. Maximum normal stress (Y Axis), maximum = 3.8954e6 Pa.

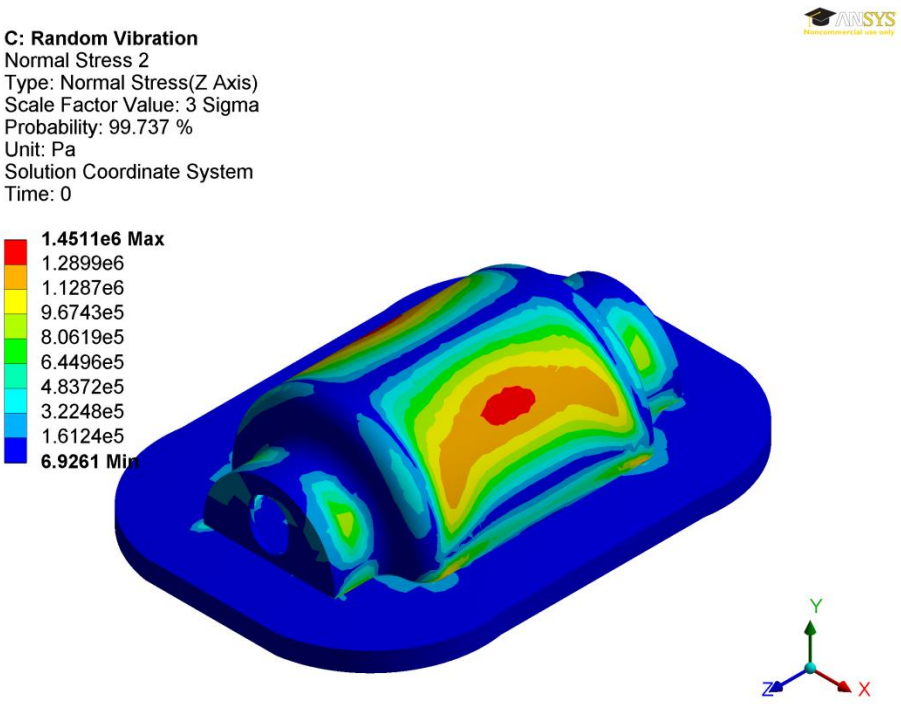

Figure 6.14. Normal stress (Z Axis), maximum = 1.4511e6 Pa.

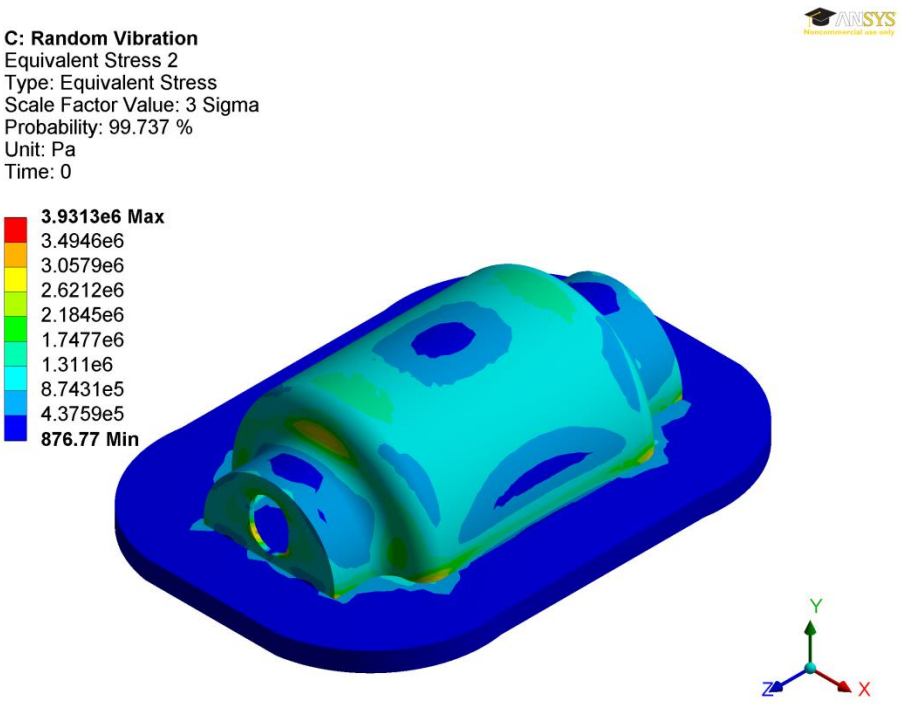

Figure 6.15. Equivalent stress, maximum = 3.9313e6 Pa.

6.11.2 Transient Analysis

A total number of 140153 nodes and 116023 elements (consisting of 2892 SOLID186, 68597 SOLID187, 16275 CONTA174, 16275 TARGE170, and 11984 SURF154) are generated, and an undamped modal analysis is performed using the sparse (direct) solver. Natural frequencies for the first 12 modes and their corresponding cumulative mass ratios are given in Table 6.3. The prestress modal analysis is not allowed for this analysis. Therefore, the obtained natural frequencies are slightly different than those of the previous analysis (*see* Tables 6.2 and 6.3). Also, the difference is partially due to the fact that we selected 12 modes to be extracted, as opposed to the 20 modes extracted in the previous analysis. Recall that in the previous analysis, 20 modes were extracted and the first 12 modes were included in the random vibration analysis. In the transient analysis, the software does not allow the user to choose a different number of modes than the ones extracted in modal analysis. Therefore, we chose 12 modes to be extracted in modal analysis.

Table 6.3. The first 12 modes, natural frequencies, and cumulative mass ratios.

Mode	Frequency (Hz)	Mx	My	Mz
1	7.21089	0.94635	0.164678E-08	0.127920E-06
2	7.54061	0.94635	0.826832E-08	0.588595E-05
3	7.67209	0.94635	0.826832E-08	0.768843
4	8.18808	0.98333	0.124824E-06	0.768843
5	8.53126	0.98333	0.107168	0.768843
6	9.06663	0.98333	0.107168	0.768843
7	9.93901	0.98333	0.823614	0.768843
8	10.20238	0.98333	0.823614	0.968253
9	10.30783	0.98333	0.823614	0.968253
10	10.37801	0.98333	0.823615	1.00000
11	10.60309	1.00000	0.823615	1.00000
12	10.76313	1.00000	1.00000	1.00000

The transient simulation has been carried out for 2 minutes duration, from 294 s to 414 s, of the seismic signal of Figure 6.8, which includes the ground acceleration peak at 354 s. Figure 6.16 depicts the selected interval of the seismic signal. The seismic acceleration is then applied to the entire structure (the ground excitation cannot be used in this solver). This resulted in a different loading condition of that in our random vibration analysis (*see* 6.11.3). The static loads are the lunar gravitational force (acting on the whole structure) and the air pressure of 1 atm (acting on all the interior surfaces).

Time steps (load steps) are selected as 0.1 second and three sub-steps are chosen for each time step. Time steps are times at which the load is specified. The sub-step number specifies the number of intervals in each time step that is used for the numerical integration.

The maximum principal stresses obtained are depicted in Figure 6.17, and the equivalent von Mises stresses are shown in Figure 6.18. In both figures the results are compared to the same results from random vibration analysis.

Figure 6.19 depicts the maximum structural error for each sub-step. However, these errors did not occur at the same locations as the maximum stresses. As an example, the stresses at time 28.8 s (pick of Figure 6.17) are shown in Figures 6.17 and the errors associated with these stresses are depicted in Figure 6.18. As it is obvious from these figures, the error associated with maximum stress at this time step is about 8×10^{-13} J. This is the case for other times as well, and therefore, the accuracy of the results are acceptable. As mentioned earlier, the errors are due to inadequacies in the generated mesh. The continuity assumption results in a continuous displacement field from element

to element, but a discontinuous stress (ANSYS 14.0 Help[a]). Therefore, a finer mesh can reduce these errors. However, we could not use a finer mesh due to software license limitation on the number of allowed nodes.

The maximum stresses in most of the time steps occurred in the vicinity of the interior doorways. As an illustration, Figure 6.20 depicts the stress distribution at 28.8 s, when the maximum principal stress occurred (peak of Figure 6.17). Also, the corresponding structural error is shown in Figure 6.21.

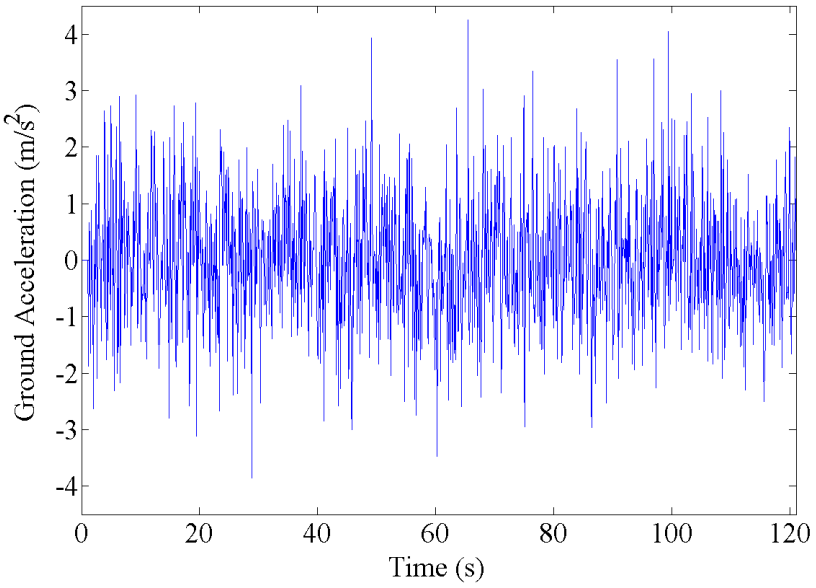

Figure 6.16. Ground acceleration signal used in transient analysis.

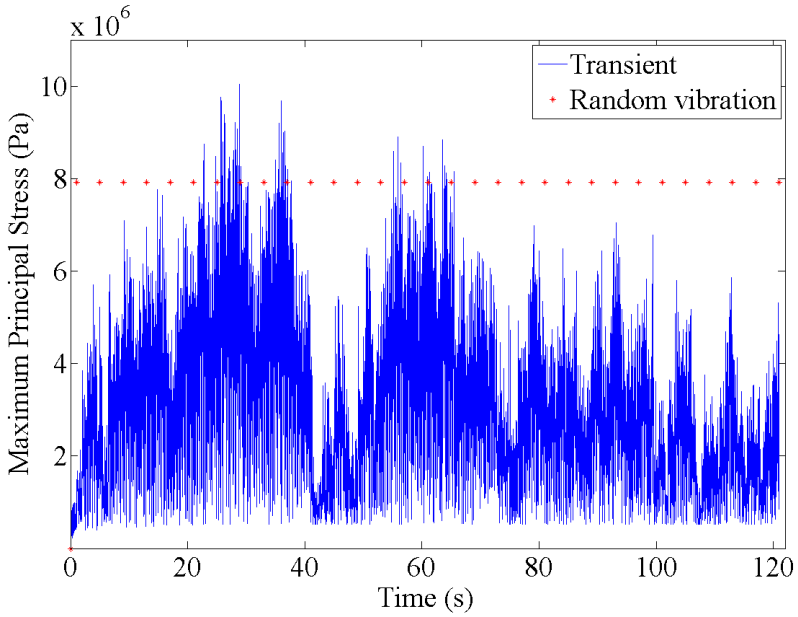

Figure 6.17. Maximum principal stresses obtained from transient modal analysis (solid lines) and random vibration (*).

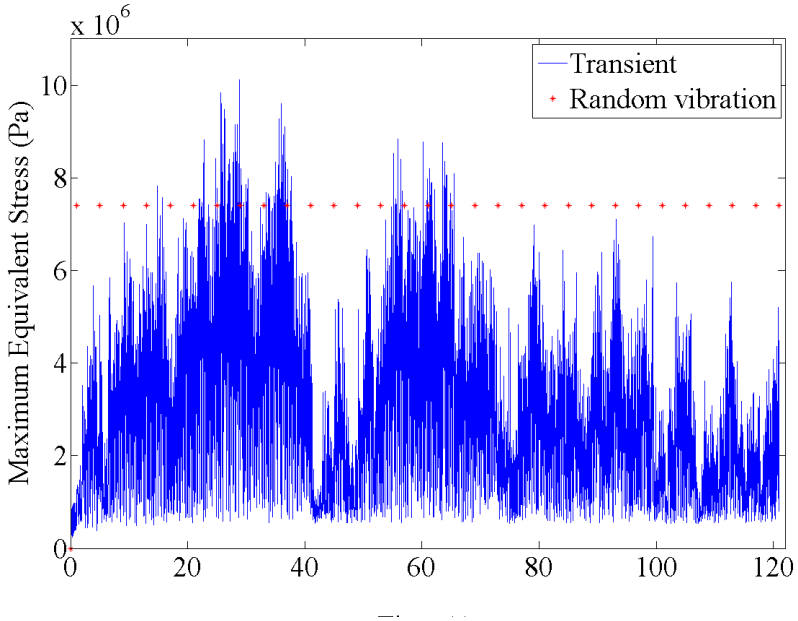

Figure 6.18. Maximum equivalent (von Mises) stresses obtained from transient modal analysis (solid lines) and random vibration (*).

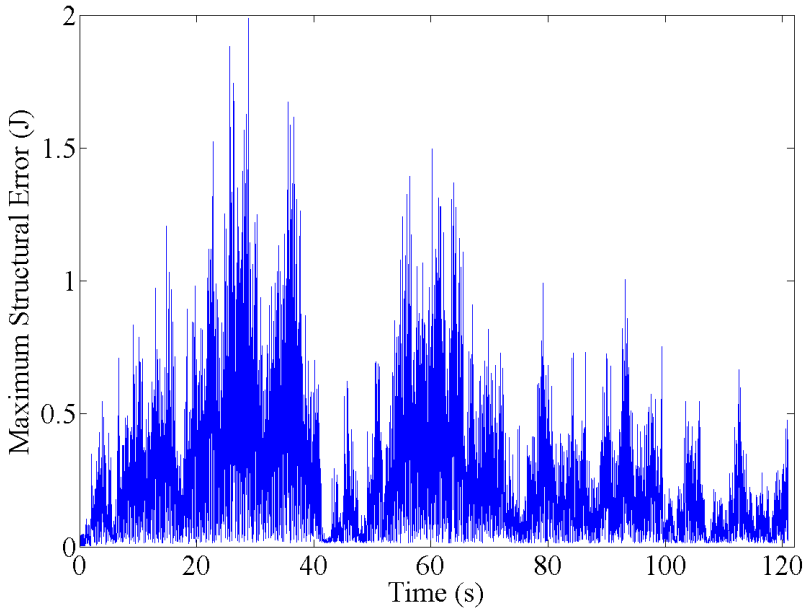

Figure 6.19. Maximum structural error in transient analysis.

6.11.3 Discussion

The results from the random vibration analysis and transient modal superposition are in reasonable agreement, considering the differences in the setups of the problem.

In random vibration analysis, as mentioned in Sections 6.3.3 and 6.11.1, the ground excitation is applied to the nodes at the fixed support (the bottom layer of the foundation), while the ground acceleration is applied to the whole body in our transient analysis. Of course, the total mass of the structure is considered in the calculations of both methods. However, in transient analysis the acceleration imposed on nodes located elsewhere than the fix support results in higher momentums and, therefore, higher stresses.

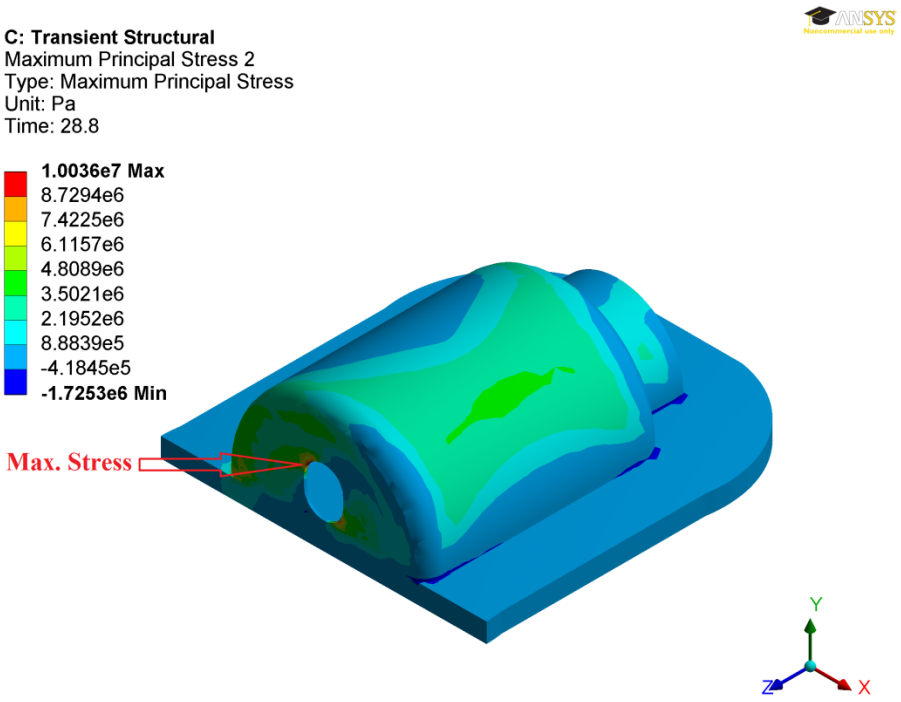

Figure 6.20. The maximum stress at the vicinity of the interior doorways at time 28.8 s.

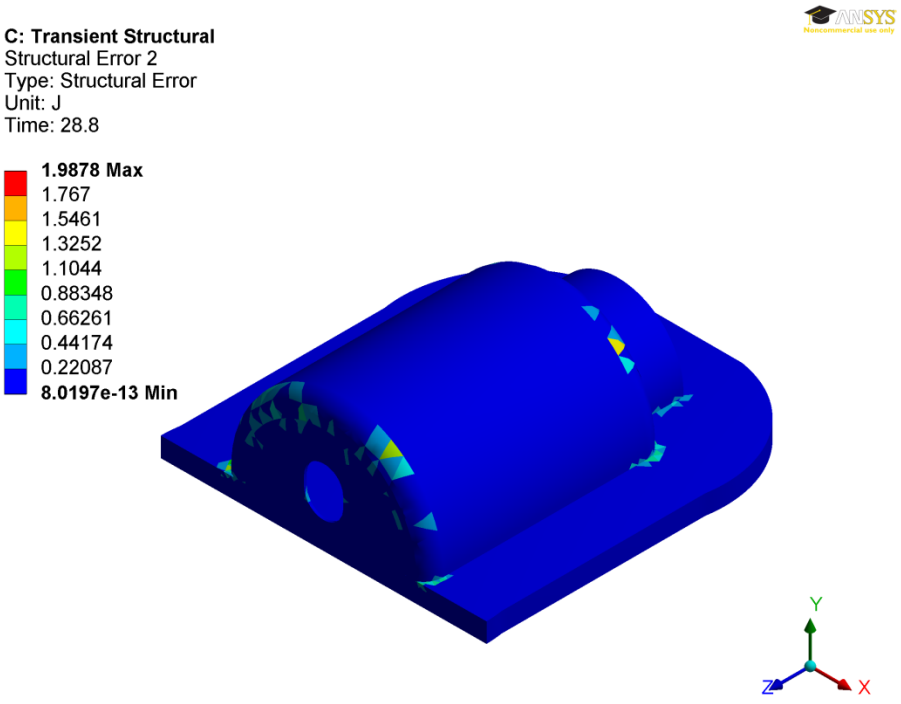

Figure 6.21. Structural error at time 28.8 s.

Selecting the maximum stress from the transient analysis (10.03 MPa) and comparing it to the yield strength of magnesium (21 MPa), we can roughly estimate that a factor of safety of the order of 3 would had sufficed. Note that the initial factor of safety in our analysis was 5.

As mentioned earlier (Chapter Four), our structural design was not optimized. The maximum stresses occurred in the vicinity of the doorways where the stress concentration is expected. In an optimized design, a more uniform stress distribution is anticipated that could result in smaller maximum stresses.

6.11.4 Computational Considerations

We did not consider a finer mesh, longer durations of the seismic excitation, or an adaptive meshing for the transient analysis due to software and hard drive storage constraints. Simulations usually took between 12 – 20 hours depending on the number of nodes and the duration of the seismic signal. We have used a Dell Precision T7600 Workstation, with an Intel® Xeon® CPU E5-2630 0, 2.30 GHz, 7.20 GT/s Intel® QPI processor and 36.0 GB of memory (RAM).

The software allowed between 1 core to 4 cores to be used for different solvers. The current transient simulation occupied about 1 TB of memory for two minutes of seismic loads. We could not perform longer simulation due to the unavailability free space on the hard drive of our workstation. Moreover, the software allows a maximum of 10000 time steps, out of which our simulation is using 3630. However, a longer simulation seems unnecessary since the results from transient and random vibration studies are very similar.

6.12 Conclusions

A seismic model based on the best available data is presented and is applied to our typical lunar surface structure. The structural response to a lunar seismic event of Richter magnitude 7 revealed that risk associated with designs that neglect seismic effects is very low since these structures are designed using relatively high factors of safety. This low risk seems reasonable especially considering the fact that lunar surface is covered with a layer of regolith and granular soil is proven to have excellent damping quality. Moreover, it is very unlikely that a moonquake of such magnitude would occur at a 25 km distance or less.

It is worth noting that Oberst and Nakamura (1992) have estimated that a lunar structure at a randomly chosen site could experience a shallow moonquake of greater than 4.5 within a range of 100 km about once in 400 years.

Our vision of first generation lunar habitats is a thin-walled structure that is covered with a thick layer of regolith shielding. These structures are expected to have fundamental frequencies higher than seismic loading frequencies, reducing the damage due to seismic events. Also, it is envisioned that these structures will be highly damped. The same statement might not stand for tall or flexible structures. Moreover, for the same type of structures with considerably thicker regolith shielding than selected here, the seismic response can be higher, since an increase in mass results in larger exerted forces to the structure by the regolith. In a modal sense, an increase of mass reduces the fundamental frequency of the total system. Also, the fundamental frequencies would be closer to excitation frequencies, magnifying the response.

Having assumed that the foundation remains intact during seismic events, the stability of the structure is not studied. It may be worthwhile to perform a foundation analysis.

Moreover, we expect second generation lunar habitats to be sub-surface structures. These types of structures will require a more detailed analysis since the effect of regolith-structure coupling become more important. Thin walled structures will unlikely be used in sub-surface structures. The seismic effects, also, should be considered in the design of vibration-sensitive instruments.

Due to minimal data and limited knowledge of the Moon's interior, the results presented are, at best, very approximate. We are hopeful that by the time the technologies are ready to construct such lunar structures, seismic experiments like the seismic package of SELENE-2 (Japanese 1st Moon lander) would shed more light on lunar seismicity. A three stations global seismic network on the moon is one of the objectives of this mission (Tanaka et al. 2008).

It is believed that shallow moonquakes are similar to intraplate earthquakes on Earth. These earthquakes reoccur after such long intervals that their occurrences are unexpected (Oberst and Nakamura 1992). If this is the case for the Moon, analyses similar to what has been presented here might be the only way to estimate the seismic response of lunar structures.

Impact structural analysis is beyond the scope of the current study, and requires separate consideration. In comparison with the lunar seismicity, meteoroid impacts can pose higher threats to a lunar structure.

Chapter 7. Conclusions and Future Work

Our literature review on lunar surface structures (Chapter One) and on the roadmaps for space exploration (Chapter Two) revealed that in-situ resource utilization is viewed by most as the best approach for successful manned exploration and settlement of the Moon and beyond. In line with these roadmaps, we proposed an advanced concept where the use of rapid prototyping technologies by mini-robots can form the basis for habitable lunar structures. Explained was our vision that mini-robots are sent to the Moon where they extract the needed lunar resources and use rapid prototyping technologies to construct lunar structures. Afterwards, these structures could become functional by small modifications with the astronauts upon their arrival.

Every aspect of this concept and goal has serious technical challenges. We mentioned that currently the capabilities needed to autonomously erect structures on the Moon is nonexistent. It is nonexistent on Earth.

Having considered the requirements of our advance concept, we proposed magnesium as a feasible structural material in Chapter Three. Then, we studied magnesium and its alloys considering the availability of alloying elements on the Moon. Our static analysis (Chapter Four) of our typical lunar structure proved that magnesium is a suitable structural material. However, at the time this study was conducted, the authors noted the lack of the literature on:

- lunar magnesium extraction; magnesium was the surplus in proposed lunar material extraction methods, and
- rapid manufacturing of magnesium and its alloys.

A lunar precursor mission would add to our knowledge of these topics.

We mentioned that few numerical studies have been carried out to model the lunar hostile environment. The extreme temperatures and temperature fluctuations, radioactivity, seismic activity, and constant meteoroid bombardments each impose threats that need special consideration in designing a lunar structure.

In Chapter Five, we considered thermal control at a lunar structure. We saw that average lunar surface temperatures at the equator swing from about 120 ^{o}K at night to about 374 ^{o}K at noon. Also, we observed milder temperature fluctuations at the lunar Polar Regions. Therefore, we selected a site at 88^{o} latitude in the lunar South Pole Region and modeled the lunar thermal environment there. The requirements for a heat rejection radiator were estimated by selecting the heat loads (per unit volume) to be the same as those for the space station. Also studied was the effects of uncertainties in regolith thermal properties and those of sintered regolith. What we have not studied was the effect of these thermal loads during the construction phase. A study can be conducted considering following scenarios:

- when the structure is being manufactured and is not shielded
- when the structure is shielded during the manufacturing phase.

It is known that magnesium alloys not containing rare Earth metals lose their mechanical properties when exposed to fluctuating temperatures. However, experiments suggesting this are conducted in temperatures very much higher than what is found on the lunar surface. Nevertheless, no study could be found on the effect of very low temperature on

the properties of magnesium, or in fact many other metals. As mentioned earlier, temperatures as low as 37 ºK were measured on lunar surface.

Despite the existence of literature on moonquakes, a seismic structural analysis of a lunar base has not been previously conducted. Therefore, in Chapter Six we presented a seismic model based on the best available data and applied it to our typical lunar structure. We chose a seismic event of Richter 7 magnitude for our analysis. Although Oberst and Nakamura (1992) presented an approximation method for estimating the occurrence of seismic events of different magnitudes for a randomly selected area of 10^6 km^2, the figure presented by them has an upper limit of 6 Richter (Figure 7.1). Using the same figure, we roughly estimated that a moonquake of magnitude 7 in the aforementioned area could occur once per few thousands of years.

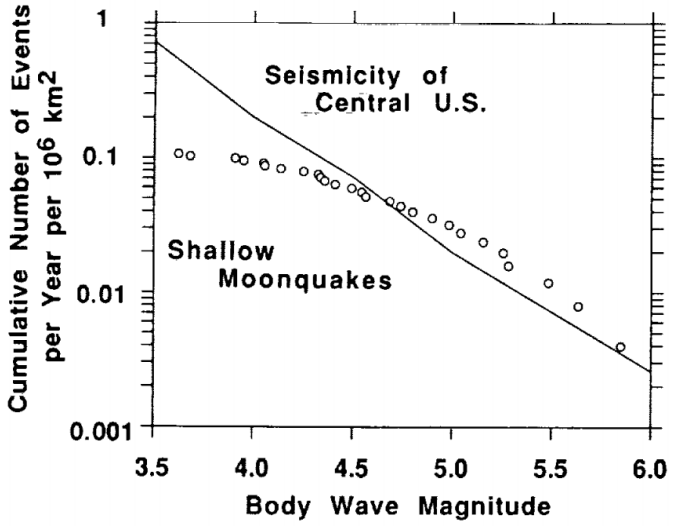

Figure 7.1. Magnitude-frequency relationships of shallow moonquakes (open circles) and intraplate earthquakes (line) (Oberst and Nakamura 1992, courtesy of NASA).

As mentioned, our analysis is, at best, very approximate due to severe lack of data. There are hopes that future experiments, like the Japanese Selene II, will help to increase our understanding of lunar seismicity. However, there is a theory that compares shallow moonquakes with intraplate earthquakes. These earthquakes are surprising events because of the long duration between their occurrences. If this theory holds, analyses similar to the one presented in Chapter Six could be the only way to evaluate the risk associated with these events. Even in this case, further experiments are necessary to understand the unknown velocity structure of the Moon.

Having considered the discussion above, our analysis estimated the seismic risk to be very low for our typical structure. The same might not be true for other types of structure or for similar structures with a substantially thicker shield.

As mentioned earlier, a meteoroid impact large enough to destroy any manmade structure was estimated during the Apollo experiments (*see* 6.6.3). No literature could be found on numerically investigating the risk associated with these rare events. Therefore, a study comprising of the following stages seems necessary:

- A global map of meteoroid impacts must be gathered that can be used to estimate the risk of impacts for different potential sites.
- An impact design code similar to terrestrial seismic codes needs to be developed. What is the biggest impact magnitude that a lunar structure must stand against?
- Lunar structural defense against large impacts – what are the options available to avoid destruction by a large impact? Perhaps a planetary defense system is needed.

- What measures would be taken to mitigate the damage if a large impact could not be avoided?

Another environmental factor that requires a separate consideration is radioactivity and is beyond the focus of our study. However, a relatively larger literature exists on the lunar radiative environment than other environmental factors. A good example is the work done by Wilson et al. (1997).

All in all, many challenges exist along the way to the design and construction of the types of systems proposed here. But there can be no settlement of the Moon and beyond without such systems. We have proved that we can travel to the Moon. Our understanding of the Moon is sufficient to engineer such a return. The main constraint will be the robotic aspects of it. The authors are optimistic that if we start today, the challenges can be resolved within the next two decades.

Appendix 1. ANSYS Definitions and Methods

Appendix 1 is a summary of the methods used by ANSYS® Academic Research Workbench, Release 14.0 software. The aim of this section is to provide the reader a basic understanding of the concepts as defined by ANSYS.

A1.1 Thermal Error

The assumption of a continuous temperature field results in a discontinuous thermal flux field. In order to obtain more acceptable fluxes, thermal flux is calculated using the averaged nodal thermal fluxes for each element, from which the thermal flux is subtracted for each node. This value is then used to calculate the energy error for each element. Therefore, the thermal fluxes error at node *n* of element *i*, Δq_n^i, is obtained by (ANSYS 14.0 Help[a])

$$\{\Delta q_n^i\} = \{q_n^a\} - \{q_n^i\}\,, \tag{A1.1}$$

where q is the thermal flux, and q_n^a is the average thermal flux vector at node *n*, given by

$$\{q_n^a\} = \frac{1}{N}\sum_{i=1}^{N}\{q_n^i\}\,, \tag{A1.2}$$

where *N* is the number of elements connecting to node *n*. The energy error for element *i*, e_i, can be calculated by

$$e_i = \frac{1}{2}\int \{\Delta q\}^T [D]^{-1}\{\Delta q\} dV\,, \tag{A1.3}$$

where *V* is the Volume, [*D*] is the conductive matrix evaluated at a reference temperature, and $\{\Delta q\}$ is the thermal flux error vector as previously defined. The error can be normalized as well.

A1.2 Stress Error

Similar to the "Thermal Error", it is an assumption that the displacement field is continuous and results in a discontinuous stress field from element to element. Therefore, the stress error vector, $\{\Delta\sigma_n^i\}$, can be obtained by (ANSYS 14.0 Help[a])

$$\{\Delta\sigma_n^i\} = \{\sigma_n^a\} - \{\sigma_n^i\}, \tag{A1.4}$$

where σ is the stress, and σ_n^a is the average stress vector at node *n*, given by

$$\{\sigma_n^a\} = \frac{1}{N}\sum_{i=1}^{N}\{\sigma_n^i\}, \tag{A1.5}$$

where *N* is the number of elements connecting to node *n*. The energy error for element *i*, e_i, can be calculated by

$$e_i = \frac{1}{2}\int\{\Delta\sigma\}^T[D]^{-1}\{\Delta\sigma\}dV, \tag{A1.6}$$

where *V* is the Volume, [*D*] is the stress-strain matrix evaluated at a reference temperature, and {Δσ} is the stress error vector as previously defined. The error can be normalized as well.

A1.3 Effective Mass Ratio

Assuming that Equation 6.3 is solved for eigenvalues, ω_i, and eigenvectors, $\{\Phi\}$, the participation factor for the i^{th} mode, γ_i, is defined as (ANSYS Theory Reference, 2011)

$$\gamma_i = \{\Phi\}_i^T\{F\}, \tag{A1.7}$$

where $\{F\}$ is the external force vector. If the modes are normalized with respect to the mass matrix, the effective mass for the i^{th} mode is

$$M_{effective} = \gamma_i^2 \ . \tag{A1.8}$$

Then the cumulative mass ratio, $M_{e,}$ for the i^{th} mode is

$$M_e = \frac{\sum_{j=1}^{i} M_{effective}}{\sum_{j=1}^{N} M_{effective}} \ , \tag{A1.9}$$

where N is the total number of modes and the subscript e is a unit vector specifying the direction for which M is calculated.

A1.4 Equivalent Stress

The equivalent stress mean square response is computed using a special algorithm proposed by Segalman and Fulcher as (In: ANSYS Theory Reference 2011)

$$(\sigma_d^2)_{nd} = \sum_{j=1}^{n}\sum_{k=1}^{n} (\Psi_j)_{nd}^{T} [A] (\Psi_k)_{nd} Q_{jk} \ , \tag{A1.10}$$

where $(\Psi_j)_{nd}$ is the vector component "stress shapes" for mode j at node nd, $[A]$ is a quadratic operator, and Q_{jk}, are the components of the nodal covariance matrices.

A1.5 ANSYS Elements

ANSYS elements presented in this section are applicable for general finite strain deformation. Their formulations (that are not presented here) are based on the principle of virtual work (ANSYS Theory Reference, 2011).

A1.5.1 SOLID187

SOLID187 is a 3D, 10-node, tetrahedral structural element, which has a quadratic displacement behavior and is suitable for modeling of irregular meshes. This element is

well capable for modeling elasticity, plasticity, hyperelasticity, creep, stress stiffening, large deflection, and large strain.

A1.5.2 SOLID186

SOLID187 is a 3D, 20-node, tetrahedral structural element, which has a quadratic displacement behavior and is suitable for modeling of irregular meshes. It has the similar capabilities to SOLID187 element.

A1.5.3 TARGE170

It describes the boundary of a deformable body and is used with solid, shell, or line elements.

A1.5.4 CONTA174

This element is used to represent contact and sliding between 3D target surface and a deformable surface, and has the same geometries as of the solid or shell elements to which it is connected. It can be used for isotropic contact regions as well as orthotropic Coulomb frictional ones.

A1.5.5. SURF154

It is used when various loads and surface effects are presents on a boundary surface.

Appendix 2. Additional Figures

Here are some additional figures from Chapter Five, Thermal Control at the Lunar Base.

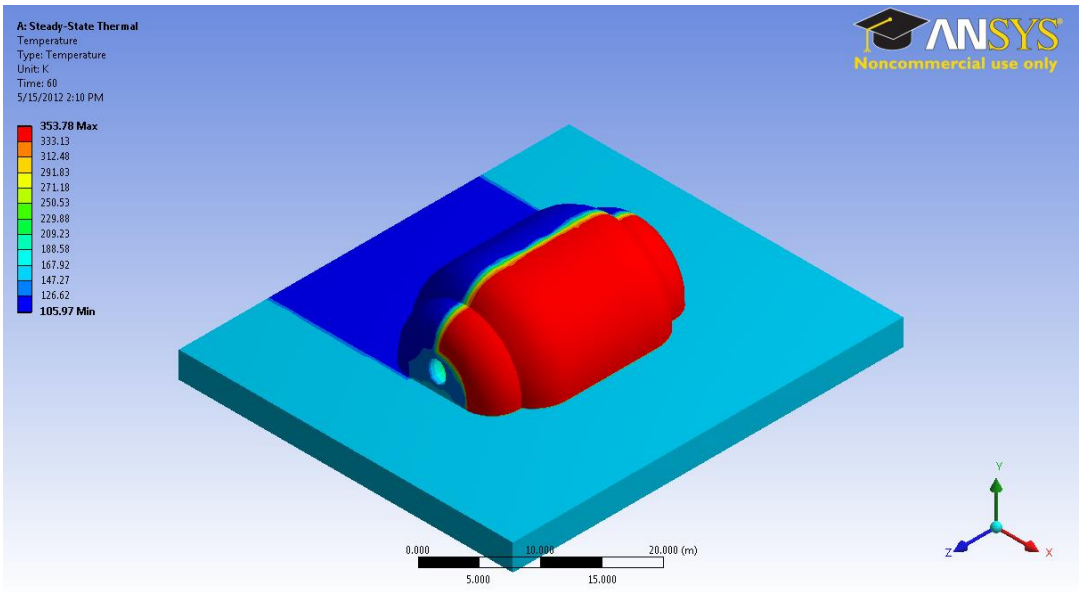

Figure A2. 1. Temperature distribution at lunar noon (max: 353.78 ºK, min: 105.97 ºK).

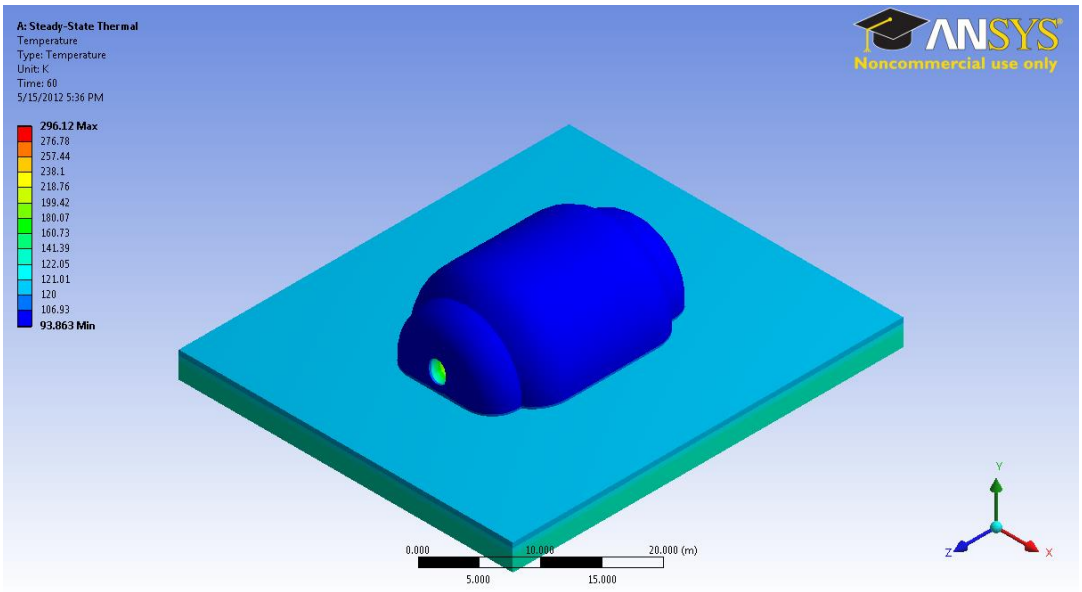

Figure A2. 2. Temperature distribution at lunar night (max: 296.12 ºK, min: 93.863 ºK).

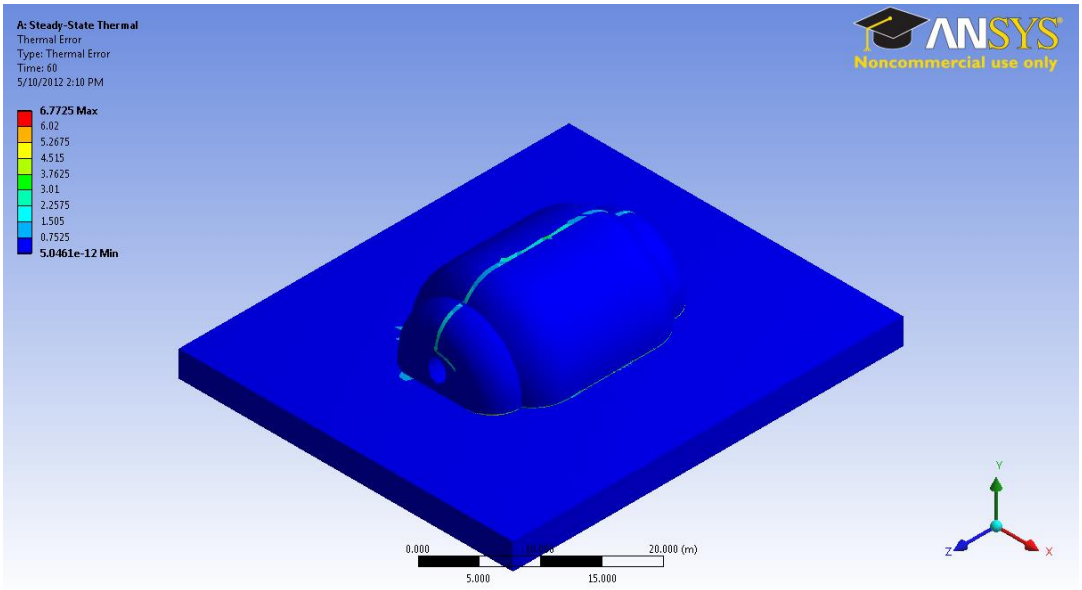

Figure A2. 3. Thermal error for case 2 at noon.

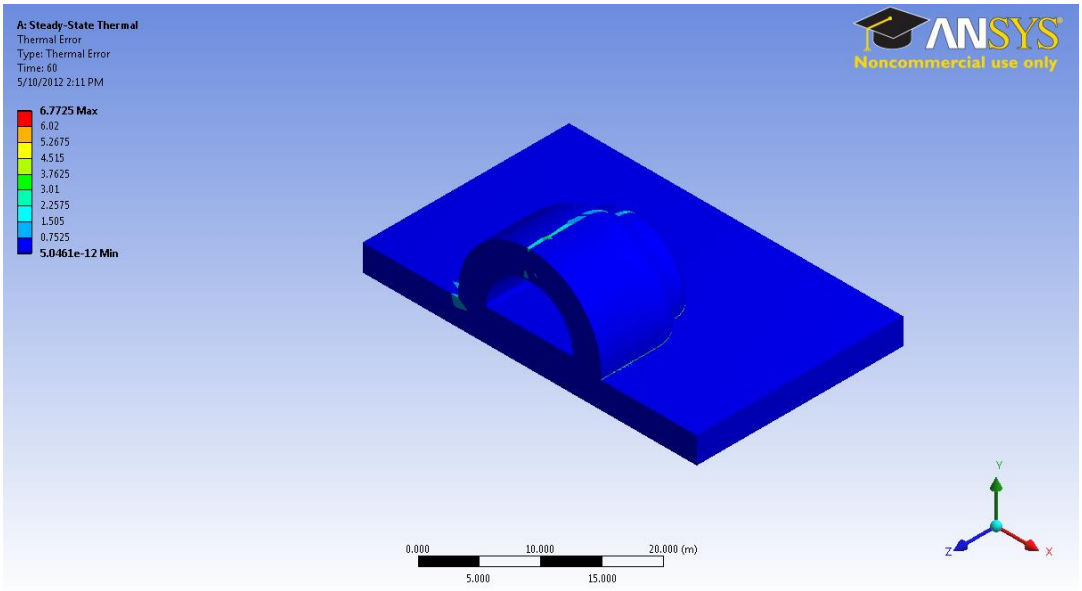

Figure A2. 4. Thermal error for case 2 at noon, cross-section view.

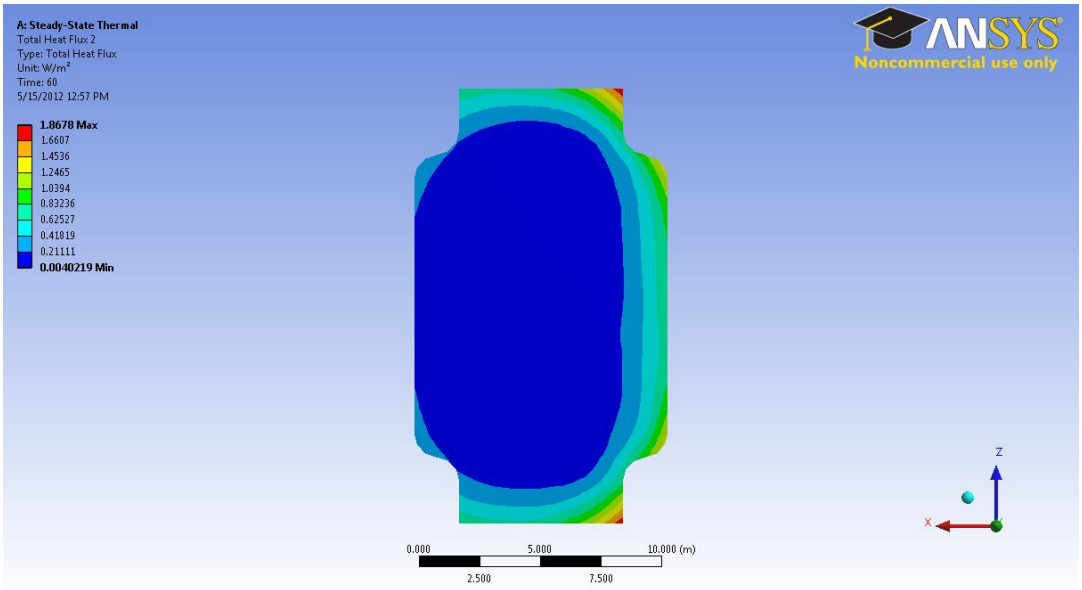

Figure A2. 5. A representative figure of the thermal flux at the foundation (case 2 at lunar noon, view from below). Max= 1.8678 W/m^2 and min= 0.0040219 W/m^2.

Appendix 3. Engineering Drawings

The engineering drawings of our typical lunar structure used for the seismic analysis are presented.

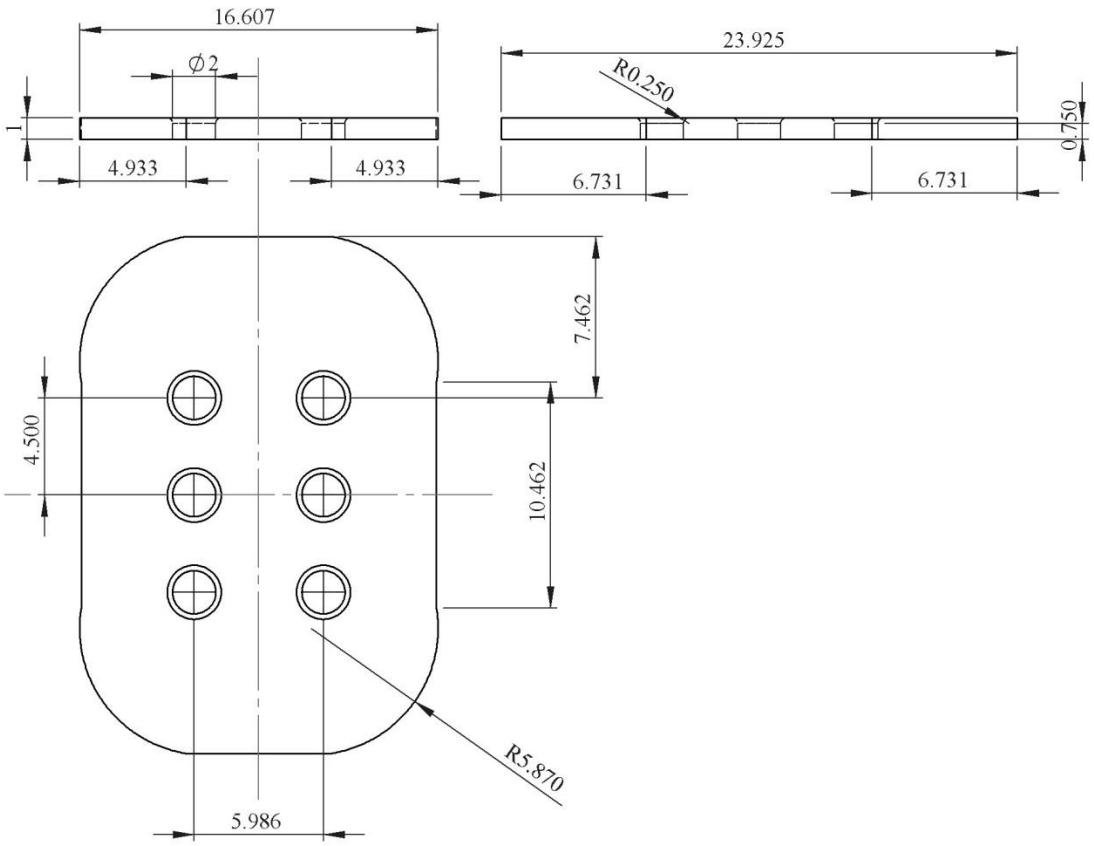

Figure A3. 1. Engineering drawing of the foundation. All dimensions are in meters.

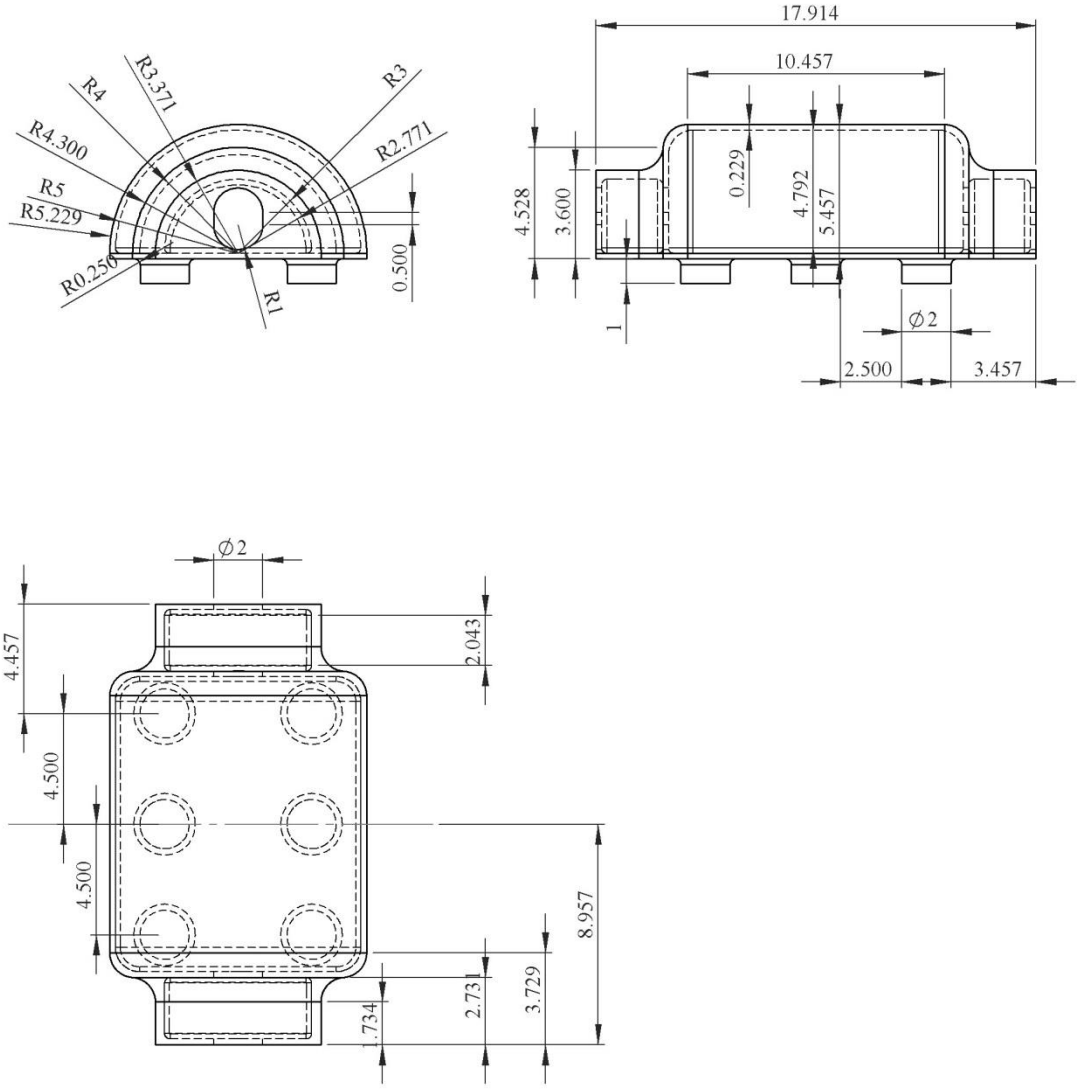

Figure A3. 2. Engineering drawing of the magnesium structure. All the dimensions are in meters.

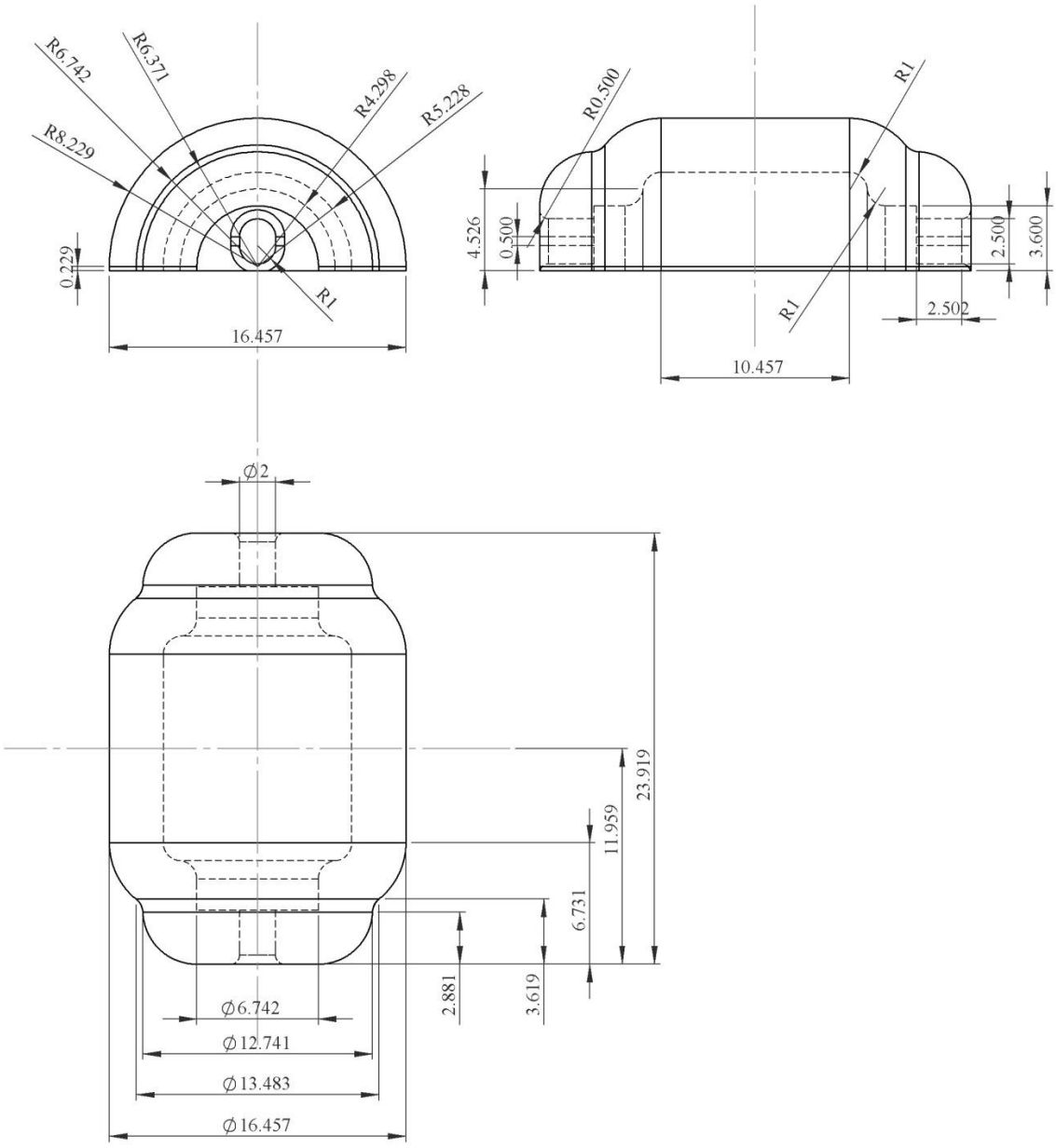

Figure A3. 3. Engineering drawing of the regolith shield. All the dimensions are in meters.

References

Aki, K., and Chouet, B. (1975). "Origin of coda waves: source, attenuation, and scattering effects." *Journal of Geophysical Research*, Vol. 80, No. 23, pp. 3322-3342.

Alderliesten, R., Rans, C., and Benedictus, R. (2008). "The applicability of magnesium based fibre metal laminates in aerospace structures." *Composites Science and Technology*, 68(14), 2983-2993.

Alford, J.M., Mason, G.R., and Feikema, D.A. (2006). "Free Fall Plasma-Arc Reactor for Synthesis of Carbon Nanotubes in Microgravity." *Review of Scientific Instruments* 77.

Amik, H. & Monterio, J.M. (2005). "Modification of concrete damping properties for vibration control in technology facilities." *Proc. SPIE 5933, Building for Nanoscale Research and Beyond,* 59330Q, San Diego, CA, USA 31 July 2005. Bellingham, WA.

Ansari, Y., Merifield, R., Yamamoto, H., and Sheng, D. (2011). "Numerical analysis of soilbags under compression and cyclic shear." *Computers and Geotechnics*, 38: 659-668.

ANSYS 14.0 Help[b], ANSYS® Academic Research Workbench, Release 14.0, Help system, Random Vibration, , Inc.

ANSYS 14.0 Help[c], ANSYS® Academic Research Workbench, Release 14.0, Help system, Block Lanczos Solver Performance Output, ANSYS, Inc.

ANSYS Theory Reference (2011). ANSYS Mechanical APDL Theory Reference. Kohnke, P. (Ed.). ANSYS® Academic Research Workbench, Release 14.0. ANSYS, Inc.

Aulesa, V. (2000). "Architecture of lunar habitats." *Exploration and Utilisation of the Moon. Proceedings of the Fourth International Conference on Exploration and Utilisation of the Moon*: *ICEUM 4*. Edited by Foing, B. H. and Perry, M., pp. 289-292, 10-14 July, 2000, at ESTEC, Noordwijk, The Netherlands. European Space Agency, ESA SP-462, 2000.

Avedesian, M.M., and Baker, H. (1999). *ASM specialty handbook: Magnesium and magnesium alloys*. ASM International.

Balasubramaniam, R., Gokoglu, S., and Hegde, U. (2010). "The reduction of lunar regolith by carbothermal rocessing using methane." *Int. J. Mineral Processing*, Vol. 96, pp. 54–61.

Beer, F. P., Johnston, Jr. E. R., and Dewolf, J.T. (2006). *Mechanics of Materials*, Fourth Edition in SI Units. McGraw Hill.

Benaroya, H., Bernold, L., and Chua, K.M. (2002). "Engineering, design and construction of lunar bases." *Journal of Aerospace Engineering*, Vol. 15, No. 2, pp. 33-45.

Benaroya, H., and Han, S.M. (2005). *Probability models in engineering and science*. CRC Press, Boca Raton, FL.

Benaroya, H., Indyk, S., and Mottaghi, S. (2012). "Advance system concept for autonomous construction and self-repair of lunar surface ISRU structures." In: *Moon: Prospective, Energy, and Material Resources*. Badescu, V. (ed.), pp. 641-660. Springer, Berlin.

Benaroya, H., Mottaghi, S., and Porter, Z. (2013). "Magnesium as an ISRU-derived resource for lunar structures." *Journal of Aerospace Engineering, Special Issue: In Situ Resourse Utilization*, 26(1): 152-159.

Benaroya, H., and Nagurka, M.L. (2010). *Mechanical vibration: analysis, uncertainties, and control* (3rd ed.). CRC Press, Boca Raton, FL.

Binder, A.B. (1990). "LLOX-metal production via NaOH electrolysis." Proc. Space 90: Engineering, Construction, and Operations in Space II, ASCE, New York, 339-346.

Boby, A., Pillai, U.T.S., and Pai, B. C. (2011). "Developments in magnesium alloys for transport applications—An overview." *Indian Foundry J.*, 57(1), 29-37.

Bottega, W.J. (2006). *Engineering vibrations*. CRC Press, Boca Raton, FL.

Cadogan, D., Stein, J., and Grahne, M. (1999). "Inflatable composite habitat structures for lunar and mars exploration." *Acta Astronautica*, Vol. 44, Issues 7–12, pp. 399-406.

Campbell, B.A., and Campbell, D.B. (2006). "Regolith properties in the south polar region of theMoon from 70-cm radar polarimetry." *Icarus*, 180, 1-7.

Cole, G.S. (2003). "Issues that influence magnesium's use in the automotive industry." *Materials Science Forum*, 419-422, 43-50.

Cortes, P., and Cantwell, W.J. (2004). "Fracture properties of fiber-metal laminates based on magnesium alloy." *Journal of Materials Science*, 39(3), 1081-1083.

Curreri, P.A., Ethridge, E.C., Hudson, S.B., Miller, T.Y., Grugel, R.N., Sen, S., and Sadoway, D.R. (2006). "Process demonstration for lunar in situ resource utilization—Molten oxide electrolysis." NASA/TM-2006-214600.

Dainty, A.M., and Toksoz, M.N. (1981). " Seismic codas on the Earth and the Moon: a comparison." *Physics of the Earth and Planetary Interiors,* Vol. 26, pp.250-260.

Dainty. A.M., Toksoz, M.N., Anderson, K.R., and Pines, P.J. (1974). "Seismic scattering and shallow structure of the Moon in oceanus procellarum." *The Moon,* Vol. 9, pp. 11-29.

Dallas, T., Diaguila, A.J., and Saltsman, J.F. (1971). NASA Technical Memorandum, Report No. NASA TM X-1846.

Davies, F.T., He, C., Lacey, R.E., and Ngo, Q. (2003). "Growing Plants for NASA – Challenges in Lunar and Martian Agriculture." *In: Combined Proceedings International Plant Propagators' Society*, vol. 53, pp. 59–64.

Dill, E.H. (2012). *The finite element method for mechanics of solids with ANSYS applications.* CRC Press. Boca Raton, FL.

Dorman, J., Evans, S., Nakamura, Y., Latham, G. (1978). "On the time-varying properties of the lunar seismic meteoroid population." *Lunar and Planetary Science Conference 9th*, pp. 3615-3626.

Duke, M.B. (ed.) (1998). Workshop on Using In-Situ Resources for Construction of Planetary Outposts. *Lunar and Planetary Institute*, 98-01.

Duke, M.B., Gaddis, L.R., Taylor, G.J., and Schmitt, H.H. (2006). "Development of the Moon." *Reviews in Mineralogy & Geochemistry*, 60(1), 597-655.

Duke, M.B., Mendell, W.W., and Roderts, B.B. (1985). "Strategies for a permanent lunar base." In: *Lunar Bases and Space Activities of the 21st Century*. Houston, TX, Lunar and Planetary Institute, edited by Mendell, W.W., pp. 57- 68.

Faierson, E.J., Logan, K.V., Stewart, B.K., and Hunt, M.P. (2010). "Demonstration of concept for fabrication of lunar physical assets utilizing lunar regolith simulant and a geothermite reaction." *Acta Astronautica* 67, 38–45.

Fairchild, K., and Mendell, W.W. (eds.) (1988). Report of the In Situ Resources Utilization Workshop, *NASA Conference Publication 3017*.

Frohlich, C., and Nakamura, Y. (2006). "Possible extra-Solar-System cause for certain lunar seismic events." *Icarus*, Vol. 185, pp. 21-28.

Goins, N.R., Dainty, A.M., Toksoz, M.N., 1981. "Seismic Energy Release of the Moon". *Journal of Geophysical Research*, Vol. 86, NO. B1, pp. 378-388.

Gruber, P., Häuplik, S., Imhof, B., Özdemir, K., Waclavicek, R., and Perino M.A. (2007). "Deployable structures for a human lunar base." *Acta Astronautica*, Vol. 61, Issues 1–6, pp. 484-495.

Gupta, M., and Sharon, N. M. L. (2011). *Magnesium, magnesium alloys, and magnesium composites*. Wiley, New York.

Hagerty, J.J., Lawrence, D.J., and Hawke, B.R. (2011). "Thorium abundances of basalt ponds in South Pole-Aitken basin: Insights into the composition and evolution of the far side lunar mantle." *Journal of Geophysical Research*, 116(E6), pp. 2156-2202.

Happel, J. A. (1993). "Indigenous materials for lunar construction." *Applied Mechanics Reviews*, 46(6), pp. 313–325.

Haskin, L. A., and Warren, P. H. (1991). "Lunar chemistry." In: Lunar sourcebook, G.H. Heiken, D.T. Vaniman, and B.M. French, eds., Cambridge Univ. Press, New York, 367-474.

Hassan, S. F., Ho, K. F., and Gupta, M. (2004). "Increasing elastic modulus, strength and CTE of AZ91 by reinforcing pure magnesium with elemental copper." *Materials Letters*, 58(16), 2143-2146.

Heiken, G.H., Vaniman, D.T., French, B.M., Schmitt, H.H., (1991). *Lunar Sourcebook, A User's Guide to the Moon.* Cambridge University Press.

Heinbockel, J.H., Slaba, T.C., Tripathi, R.K., Blattnig, S.R., Norbury, J.W., Badavi, F.F., Townsend, L.W., Handler, T., Gabriel, T.A., Pinsky, L.S., Reddell, B., and Aumann, A.R. (2011). "Comparison of the transport codes HZETRN, HETC and FLUKA for galactic cosmic rays." *Advances in Space Research*, 47(6), 1089-1105.

Hemingway, B.S., Robie, R.A., and Wilson, W.H. (1973). "Specific heats of lunar soils, basalt, and breccias from the Apollo 14, 15, and 16 landing sites, between 90 and 350 ºK." *Proceedings of the Fourth Lunar science Conference, Supplement 4, Geochemica et Cosmochimica Acta*, 3, pp.2481-2487.

Hibbeler, R.C. (2011). *Mechanics of Materials*, Eight Edition. Prentice Hall.

Hobosyan, M.A., and Martirosyan, K.S. (2012). "Sintering of regolith by activated thermites: a novel approach for lunar in-situ resource utilization." *43rd Lunar and Planetary Science Conference*, March 19–23, 2012 at The Woodlands, Texas. LPI Contribution No. 1659, id.1019.

Holladay, J.D., Brooks, K.P., Wegeng, R., Hu, J., Sanders, J., and Baird, S. (2007). "Microreactor development for Martian in situ propellant production." *Catalysis Today* 120, 35–44.

Horton, C., Gramajo, C., Alemu, A., Williams, L., Ignatiev, A., and Freundlich, A. (2005). "First demonstration of photovoltaic diodes on lunar regolith-based substrate." *Acta Astronautica* 56, 537–545.

Howell, J.R., 2012. A Catalog for Radiation Heat transfer Configuration Factors. University of Texas at Austin. Web. http://www.me.utexas.edu/~Howell/tablecon.html#C1 (as of 3/26/2013).

Hu, J., Brooks, K.P., Holladay, J.D., Howe, D.T., and Simon, T.M. (2007). "Catalyst development for microchannel reactors for Martian in situ propellant production." *Catalysis Today* 125, 103–110.

Ishibashi, I. & Zhang, X. (1993). "Unified dynamic shear moduli and damping ratios of sand and clay." *Soil and Foundations*, 33(1): 182-191. Japanese Society of Soil and Mechanics and Foundation Engineering.

ITW Densit, Data Sheet, *Densit.com* (2012). Web. http://www.densit.com/Files/Filer/pdf_files/Wearprotection/Products/pro-cast-basalt-uk.pdf

Jayalakshmi, S., Kailas, S. V., and Seshan, S. (2002). "Tensile behaviour of squeeze cast AM100 magnesium alloy and its Al2O3 fibre reinforced composites." *Composites Part A: Applied Science and Manufacturing*, 33(8), 1135-1140.

Jin, Q., Eom, J. P., Lim, S. G., Park, W. W., and You, B. S. (2003). "Grain refining mechanism of a carbon addition method in aMgeAl magnesium alloy." *Scripta Materialia,* 49(11), 1129-1132.

Johnson, S.W. and Leonard, R.S. (1985). "Evolution of concepts for lunar bases." In: Mendell W.W. (ed.), *Lunar bases and space activities of 21st century*. Houston, TX, Lunar and Planetary Institute, pp. 47-56.

Kaneko, T., and Suzuki, M. (2003). "Automotive applications of magnesium alloys." *Materials Science Forum*, 419e422, 67-74.

Kaplicky, J. and Nixon, D. 1985. "A surface-assembled superstructure envelope system to support regolith mass- shielding for an initial-operational-capability lunar base." In: *Lunar Bases and Space Activities of the 21st Century*. Houston, TX, Lunar and Planetary Institute, edited by Mendell, W.W., pp. 375-380.

Keihm, S.J., and Langseth, M.G. Jr. (1973). "Surface Brightness Temperatures at the Apollo 17 Heat Flow Site: Thermal conductivity of the upper 15 cm of regolith." *Proceedings of the Fourth Lunar Science Conference (Supplement 4, Geochimica et Cosmochimica Acta),* Vol. 3, pp.2503-2513.

Keihm, S.J., Peters, K., Langseth, M.G., and Chute, J.L. Jr. (1973). "Apollo 15 Measurement of Lunar Surface Brightness Temperatures Thermal Conductivity of the Upper $1\frac{1}{2}$ Meters of Regolith." *Earth and Planetary Science Letters* 19, pp. 337-351.

King, C.B., Butterfield, A.J., Hypes, W.D., Neal, J.E., and Simonsen, L.C. (1990). "Single launch lunar habitat derived from NSTS external tank." NASA Technical Memorandum 4212. Report No. TM-4212.

Kozyrovska, N.O., Lutvynenko, T.L., Korniichuk, O.S., Kovalchuk, M.V., Voznyuk, T.M., Kononuchenko, O., Zaetz, I., Rogutskyy, I.S., Mytrokhyn, O.V., Mashkovska, S.P., Foing, B.H., and Kordyum, V.A. (2006). "Growing pioneer plants for a lunar base." *Advances in Space Research* 37, 93–99.

Land, P. (1985). "Lunar base design." In: *Lunar Bases and Space Activities of the 21st Century*. Houston, TX, Lunar and Planetary Institute, edited by Mendell, W.W., pp. 363-373.

Landis, G.A. (2007). "Materials refining on the Moon." *Acta Astronautica* 60(10-11), 906–915.

Langseth, M. G., Keihm, and S.J., Peters, K. (1976). "Revised lunar heat-flow values." *Proc. Lunar Sci. Conf. 7th*, pp. 3143-3171.

Latham, G., Ewing, M., Press, F., Sutton, G. (1969). "The Apollo Passive Seismic Experiment." *Science,* Vol. 165, pp. 241-250.

Latham, G.V., Ewing, M., Press, F., Sutton, G., Dorman, J., Nakamura, Y., Toksoz, N., Wiggins,R., Derr, J., and Duennebier, F. (1970). "Apollo 11 passive seismic experiment." *Proceedings of Apollo 11 Lunar Science Conference,* Vol. 3, pp. 2309-2320.

Lawrence, D. J., Feldman, W.C., Barraclough, B.L., Binder, A.B., Elphic, R.C., Maurice, S., Miller, M.C., and Prettyman, T.H. (2000). "Thorium abundances on the lunar surface." *Journal of Geophysical Research*, 105(E8), 20307-20331.

Lin, T., Senseney, J., Arp, L., and Lindbergh, C. (1989). "Concrete lunar base investigation." *Journal of Aerospace Engineering*, Vol. 2, No.1, pp. 10–19.

Liu, Y., and Taylor, L. A. (2011). "Characterization of lunar dust and a synopsis of available lunar simulants." *Planetary and Space Science,* 59(14), 1769-1783.

Logan, L.M, Hunt, G.R., Balsamo, S.R., and Salisbury, J.W. (1972). "Midinfrared emission spectra of Apollo 14 and 15 soils and remote compositional mapping of the Moon." *Proceedings of the Third Lunar Science Conference (Supplement 3, Geochimica et Cosmochimica Acta)*, Vol. 3, pp. 3069-3076. The M.I.T. Press.

Luo, A., and Pekguleryuz, M.O. (1994). "Review cast magnesium alloys for elevated temperature applications." *Journal of Materials Science*, 29(20), 5259-5271.

Mackay, D.B. (1963). *Design of Space Powerplants*. Prentice-Hall International Series in Space Technology.

Magnesium Elektron Ltd. (2011a). Datasheet 102.

Magnesium Elektron Ltd. (2011b). Datasheet 440.

Magnesium Elektron Ltd. (2011c). Datasheet 454.

Magnesium Elektron Ltd. (2011d). Datasheet 455.

Magnesium Elektron Ltd. (2011e). Datasheet 475.

McCallum, I.S., Domeneghetti, M.C., Schwartz, J.M., Mullen, E.K., Zema, M., Ca´mara, F., McCammon, C., and Ganguly, J. (2006). "Cooling history of lunar Mg-suite gabbronorite 76255, troctolite 76535 and Stillwater pyroxenite SC-936: The record in exsolution and ordering in pyroxene." *Geochim. Cosmochim. Acta*, 70(24), 6068-6078.

McCammon, C. and Ganguly, J. (2006). "Cooling history of lunar Mg-suite abbronorite 76255, troctolite 76535 and Stillwater pyroxenite SC-936: The record in exsolution and ordering in pyroxene." *Geochimica et Cosmochimica Acta,* 70, pp. 6068–6078.

McKay, D.S., Heiken, G., Basu, A., Blanford, G., Simon, S., Reedy, R., French, B.M., and Papike, J. (1991). "The Lunar Regolith." In: *Lunar Sourcebook*. Heiken, G.H., Vaniman, D.T., and French, B.M., eds., Cambridge Univ. Press, New York, 285-356.

Mendell, W. (ed.) (1985). *Lunar Bases and Space Activities of the 21st Century*. Lunar and Planetary Institute.

Meyers, C., and Toutanji, H. (2007). "Analysis of Lunar-Habitat Structure Using Waterless Concrete and Tension Glass Fibers." *Journal of Aerospace Engineering*, Vol. 20, No.4, pp. 220-226.

Miller, J., Taylor,L., Zeitlin, C., Heilbronn, L., Guetersloh, S., DiGiuseppe, M., Iwata, Y., and Murakami, T. (2009). "Lunar soil as shielding against space radiation." *Radiation Measurements*, 44(2), 163-167.

Moore, C.L. (2010). "Technology development for human exploration of Mars." *Acta Astronautica,* 67, 1170–1175.

Mordike, B. L. (2002). "Creep-resistant magnesium alloys." *Materials Science and Engineering A*, 324, 103-112.

Mordike, B. L., and Ebert, T. (2001). "Magnesium properties, applications, potential." *Materials Science and Engineering A*, 302(1-2), 37-45.

Moslemi, M., Kianoush, M.R., Pogorzelski, W. (2011). "Seismic response of liquid-filled elevated tanks." *Engineering Structures*, Vol. 33, Issue 6, pp. 2074-2084.

Nakamura, Y. (1976). "Seismic energy transmission in the lunar surface zone determined from signals generated by movement of lunar rovers." *Bulletin of the Seismological Society of America*, Vol. 66, No., 2, pp. 593-606.

Nakamura, Y., and Koyama, J. (1982). "Seismic Q of the Lunar Upper Mantle." *Journal of Geophysical Research,* Vol. 87, No. B6, pp. 4855-4861.

Nakamura, Y., Latham, G.V., and Dorman, H.J. (1982). "Apollo Lunar Seismic Experiment – Final Summary." *Proceedings of the Thirteenth Lunar and Planetary Science Conference, Part 1. Journal of Geophysical Research*, Vol. 87, Supplement, pp. A117-A123.

Nakamura, Y., Latham, G.V., Dorman, H.J., Ibrahim, A. K., Koyama, J., and Horvath, P. (1979). "Shallow moonquakes: Depth, distribution and implications as to the present state of the lunar interior". *Proceedings of Lunar and Planetary Science Conference 10th*, pp. 2299-2309.

Neelakanta, P.S. (1995). *Handbook of electromagnetic materials, monolithic and composite versions and their applications*. CRC Press.

Ng, C.C., Savalani, M.M., Lau, M.L., and Man, H.C. (2011). "Microstructure and mechanical properties of selective laser melted magnesium." *Applied Surface Science*, 257(17), 7447-7454.

Nowak, P.S., Sadeh, W.Z., and Morroni, L.A. (1992). "Geometric modeling of inflatable structures for lunar base." *Journal of Aerospace Engineering*, Vol. 5, No. 3, pp. 311-322.

Oberst, J. (1987). "Unusually high stress drops associated with shallow moonquakes." *Journal of Geophysical Research,* Vol. 92(B2), pp. 1397-1405.

Oberst, J., and Nakamura, Y. (1992). "A seismic risk for the lunar base." NASA, Johnson Space Center, *The Second Conference on Lunar Bases and Space Activities of the 21st Century*, Vol. 1, pp 231-233.

O'Handly, D. (2000). "System Architecture Development for a Self-Sustaining Lunar Colony." Orbitec Technologies Corporation Final Report for the NASA Institute for Advanced Concepts, pp. 1-54. Web.http://www.scribd.com/doc/20158534/ORBITEC-System-Architecture-Development-for-a-Self-Sustaining-Lunar-Colony

Ostrovsky, I., and Henn, Y. (2007). "Present state and future of magnesium application in aerospace industry." International Conf. New Challenges in Aeronautics, Moscow.

Paige, D.A., Siegler, M.A., Zhang, J.A., Hayne, P.O., Foote, E.J., Bennett, K.A., Vasavada, A.R., Greenhagen, B.T., Schofield, J.T., McCleese, D.J., Foote, M.C., DeJong, E., Bills, B.G., Hartford, W., Murray,B.C., Allen, C.C., Snook, K., Soderblom, L.A., Calcutt, S., Taylor, F.W., Bowles, N.E., Bandfield, J.L., Elphic, R., Ghent, R., Glotch, T.D., Wyatt, M.B., and Lucey,P.G. (2010). "Diviner Lunar Radiometer Observations of Cold Traps in the Moon's South Polar Region." *Science*, pp. 330-479; DOI: 10.1126/science.1187726.

Papike, J.J., Taylor, L., and Simon, S. (1991). "Lunar minerals." In: *Lunar sourcebook*. Heiken, G., Vaniman, D., and French, B., eds., Cambridge Univ. Press, Cambridge, U.K., 121-181.

Pokhmurska, H., Wielage, B., Lampke, T., Grund, T., Student, M., and Chervinska, N. (2008). "Post-treatment of thermal spray coatings on magnesium." *Surface and Coatings Technology*, 202(18), 4515-4524.

Polmear, I.J. (1994). "Magnesium alloys and applications." *Materials Science and Technology*, 10(1), 1-16.

Qian, M., and Das, A. (2006). "Grain refinement of magnesium alloys by zirconium: Formation of equiaxed grains." *Scripta Materialia*, 54(5), 881-886.

Roberts, M. (1988). "lnflatable habitation for the lunar base." *NASA Conf. Publ*. No. 3166, NASA, Washington, D.C.

Ruess, F., Schänzlin, J., Benaroya, H. (2006). "Structural Design of a Lunar Habitat." *Journal of Aerospace Engineering*, 19(3), 133–157.

Sanders, G.B., and Duke, M. (2005). NAS. In: *Situ Resource Utilization (ISRU) Capability Roadmap Final Report*.

Seboldt, W., Lingner, S., Hoernes, S., Grimmeisen, W., Lekies, R., Herkelmann, R., and Burt, D. (1993). "Lunar oxygen extraction using fluorine." In: *Resources of near earth space*. Lewis, J.S., Matthews, M.S. , and Guerrieri, M.L., eds., University of Arizona Press, Tucson, AZ, 129-148.

Sen, S., Ray, C.S., and Reddy, R.G. (2005). "Processing of lunar soil simulant for space exploration applications." *Materials Science and Engineering A*, 413-414, 592–597.

Senf, J., Broszeit, E., Gugau, M., and Berger, C. (2000). "Corrosion and galvanic corrosion of die casted magnesium alloys." In: *Magnesium technology 2000*. Kaplan, H.I., Hryn, J., and Clow, B., eds., Minerals, Metals & Materials Society.

Senior, C.L. (1993). “Lunar oxygen production by pyrolysis.” In: *Resources of near earth space*. Lewis, J.S., Matthews, M.S. , and Guerrieri, M.L., eds., University of Arizona Press, Tucson, AZ, 179-196.

Shkuratov, Y. G., Kaydash, V.G., Stankevich, D.G., Starukhina, L.V., Pinet, P.C., Chevrel, S.D., and Daydou, Y.H. (2005). “Derivation of elemental abundance maps at intermediate resolution from optical interpolation of lunar prospector gamma-ray spectrometer data.” *Planetary and Space Science*, 53(12), 1287-1301.

Shu, D.W., and Ahmad, I. R. (2011). “Magnesium alloys: An alternative for aluminum in structural applications.” *Advanced Materials Research*, 168-170, 1631-1635.

Siegel, R., and Howell, J.R. (1992). *Thermal Radiation Heat Transfer*, third edition. Hemisphere Publishing Corporation.

Siegfried, W.H., and Santa, J.E. (2000). “Use of Propellant from the Moon in human exploration & development of space.” *Acta Astronautica*, Vol. 47, pp. 365–375.

Simonsen, L.C., Debarro, M.J., and Farmer, J.T. (1992). “Conceptual Design of a Lunar Base Thermal Control System”. *The Second Conference on Lunar Bases and Space Activities of the 21st Century*, Proceedings from a conference held in Houston, TX, April 5-7, 1988. Edited by Mendell, W.W., NASA Conference Publication 3166, p.579.

Sparrow, E.M., and Cess, R.D. (1978). *Radiation Heat Transfer*, augmented edition. Hemisphere Publishing Corporation.

Sridhar, K.R., Finn, J.E., and Kliss, M.H. (2000). “In-situ Resource Utilization Technologies for Mars Life Support Systems.” *Advances in Space Research*, 25(2), 249–255.

Sridharan, R., Ahmed, S.M., Das, T.P., Sreelatha, P., Pradeepkumar, P., Naik, N., and Supriya, G. (2010). “‘Direct’ evidence for water (H2O) in the sunlit lunar ambience from CHACE on MIP of Chandrayaan I.” *Planetary and Space Science*, 58, 947–950.

Stein, S., and Wysession, M. (2003). *An Introduction to Seismology, Earthquakes, and Earth Structure*. Blackwell Publishing Ltd.

StJohn, D.H., Qian, M., Easton, M.A., Cao, P., and Hildebrand, Z. (2005). “Grain refinement ofmagnesiumalloys.” *Metall Mater Trans A*, 36(7), 1669-1679.

Stringer, D.B., Sheth, P.N., and Allaire, P.E. (2010). “Modal reduction of geared rotor systems with general damping and gyroscopic effects.” *Journal of Vibration and Control*, 17(7), pp. 975-987.

Superform Aluminum. (2010). “AZ31B-O automotive material data sheet, Magnesium Elecktron alloys.” http://www.superform-aluminium.com.

Tanaka, S., Shiraishi, H., Kato, M., Okada, T., (2008). “The science objectives of the SELENE-II mission as the post SELENE mission.” *Advances in Space Research*, 42(2), pp. 394-401.

Taylor, G.J., and Martel, M.V. (2003). “Lunar prospecting.” *Advances in Space Research*, Vol. 31, No. 11, pp. 2403–2412.

Taylor, L.A., and Carrier, W.D. (1993). “Oxygen production on the Moon-An overview and evaluation.” In: *Resources of near earth space.* Lewis, J.S., Matthews, M.S., and Guerrieri, M.L., eds., University of Arizona Press, Tucson, AZ, 69-108.

Toksoz, M.N., Dainty, A.M., Solomon, S.C., and Anderson, K.R. (1974). “Structure of the Moon.” *Reviews of Geophysics and Space Physics*, Vol. 12, No. 4, pp. 539-567.

Toutanji, H.A., Evans, S., and Grugel, R.N. (2012). “Performance of lunar sulfur concrete in lunar environments.” *Construction and Building Materials*, Vol. 29, pp. 444 – 448.

Vaniman, D., Reedy, R., Heiken, G., Olhoeft, G., and Mendell, W. (1991). “ The lunar environment.” In: *Lunar Sourcebook*. Heiken, G., Vaniman, D., and French, B., eds., Cambridge Univ. Press, Cambridge, U.K. pp.27- 60.

Vai, A.T., Yurko, J.A., Wang, D.H., and Sadoway, D.R. (2010). “Molten oxide electrolysis for lunar oxygen generation using in-situ resources.” *Jim Evans Honorary Symposium*, TMS Annual Meeting 2010, Seattle, 301-308.

Wang, T., Debelak, K.A., and Roth, J.A. (2008). “Extraction of magnesium and copper using a surfactant and water in supercritical carbon dioxide.” *Journal of Supercritical Fluids*, 47(1), 25–30.

Warren, P.H., and Rasmussen, K.L. (1987). “Megaregolith Insulation, Internal Temperatures, and Bulk Uranium Content of the Moon.” *Journal of Geophysical Research*, Vol. 92, No. B5, pp. 3453-3465.

Watarai, H. (2006). “Trend of research and development for magnesium alloys.” *Science & Technology Trends - Quarterly Review*, 18, 84-97.

Wesley, J.P. (1965). “Diffusion of seismic energy in the near range.” *Journal of Geophysical Research*, Vol. 70, No. 20, pp. 5099-5106.

Williams, R.J., and Hubbard, N. (1981). *Report of Workshop on Methodology for Evaluating Potential Lunar Resource Sites*, NASA Technical Memorandum 58235.

Williams, R.J., and Jadwick, J.J. (1980). *Handbook of lunar materials*. NASA Reference Publication 1057.

Wilson, J.W., Simonsen, L.C., Shinn, J.L., Dubey, R.R., Jordan, W., and Kim, M. (1997). “Radiation analysis for the human lunar return mission.” NASA Technical Paper 3662.

Yang, Z.R., Wang, S.Q., Gao, M.J., Zhao, Y.T., Chen, K.M., and Cui, X.H. (2008). “A new-developed magnesium matrix composite by reactive sintering.” *Composites Part A: Applied Science and Manufacturing*, 39(9), 1427-1432.